

**INCOMMENSURATE HETEROEPITAXY BY VAN DER WAALS AND
WEAK CHEMICAL INTERACTIONS FOR EPITAXIAL THIN FILM
TRANSFER**

INCOMMENSURATE HETEROEPITAXY BY VAN DER WAALS AND
WEAK CHEMICAL INTERACTIONS FOR EPITAXIAL THIN FILM
TRANSFER

By

STEPHEN JOVANOVIC, M.A.Sc.

A Thesis Submitted to the School of Graduate Studies in Partial Fulfilment
of the Requirements for the Degree of Doctor of Philosophy

McMaster University

©Copyright by Stephen Jovanovic, April 2021

Doctor of Philosophy (2020)
(Department of Engineering Physics)

McMaster University
Hamilton, Ontario

TITLE: Incommensurate Heteroepitaxy by van der Waals and Weak Chemical Interactions for Epitaxial Thin Film Transfer

AUTHOR: Stephen Michael Jovanovic, M.A.Sc., (McMaster University)

SUPERVISOR: Dr. John S. Preston

NUMBER OF PAGES: xiii, 163

Abstract

High quality crystalline semiconductor films are a key component in the production of electronic and opto-electronic devices, however, the requirement of latticed-matched single crystal substrates for the epitaxy of a thin film limits the available material systems which can be developed commercially. This strict lattice matching requirement is relaxed for two-dimensional layered materials grown via van der Waals epitaxy. Unfortunately, the same low surface energies of these layered materials also suppress the growth of three-dimensional materials upon them, preventing direct large area single-crystal growth.

The work presented in this thesis will demonstrate and investigate the spontaneous van der Waals epitaxy, driven by weak chemical interaction, of a three-dimensional material on a three-dimensional material system. Despite a 3.7% lattice mismatch, high quality CdTe can be heteroepitaxially deposited on α -Al₂O₃ but with an incommensurate interface which demonstrates weak adhesion between the film/substrate.

This weak adhesion is exploited by developing a strain driven epitaxial thin film transfer and handling method, which causes deposited layers and structures to separate at the substrate interface for transfer to secondary carrier substrates without effecting the film properties and leaving the original substrate for subsequent use. Simple transferred thin film crystalline II-VI heterostructure devices on flexible substrates are

demonstrated, without the need for selective chemical etch layers, ion-implantation or complex post-processes as required by conventional fabrication techniques. Following a growth study of GaAs on three oxide substrates, the phenomena of epitaxial registry with apparent weak interface adhesion is demonstrated for another system, GaAs/ α -Al₂O₃, where a layer transferred heterostructure device on a flexible substrate is also demonstrated.

Acknowledgements

I would like to gratefully acknowledge and thank the following for their help and support, not just during my doctoral studies, but during my entire time at McMaster:

The National Sciences and Engineering Research Council of Canada for providing financial support of this project and myself through its grants and scholarship programs.

My supervisor, Dr. John Preston, who has not only given me this opportunity to work on a project I am passionate about, but for his mentorship, wisdom, and guidance. Thank you for the academic freedom to be creative and try things for the sake of scientific exploration. Thank you for always being there when it counted most.

My committee members, Dr. Adrian Kitai and Dr. Ray LaPierre, for their guidance and input throughout my degree, but also for the support and collaboration on a variety of projects. In addition, I would also like to thank Dr. Nabil Bassim and Dr. Kari Dalnoki-Veress for their support and collaboration during my studies.

My colleagues at McMaster, Michael Cino, Dr. Paul Kuyanov and Hesham El-Sherif for fruitful discussion, advice, experimental collaboration and perhaps most of all for putting up with my terrible sense of humor.

All the technical staff of the university, who are the backbone of all research work and the unsung heroes for graduate student at the university. In particular, I wanted to thank Jim Garrett of the BIMR; Andy Duft and Chris Butcher of the CCEM; Zhilin Peng of the CANS Facility; Doris Stevanovic, Dr. Ross Anthony, and Dr. Shahram Ghanad-Tavakoli of the CEDT; Peter Jonasson and Simon McNamee of the Department of Engineering Physics; and Dr. Jim Britten and Victoria Jarvis of the X-ray Crystallography Facility.

All my in-laws, for all their love, support, encouragement, and motivation: Fatima Majdi, Mansour Haftshijani, Mila Haftshijani, Edris Majdi and Melissa Melanson. I want to provide an additional thank you to my parents-in-law, Dr. Abbas Majdi and Mahin Majdi, for welcoming me graciously into their family and home as one of their own.

My brothers, Andrew and Paul, for their encouragement. I could not be prouder of who you both are and who you continue to grow into as the years go by.

My parents, John and Kathy, and grandparents, Nerina and Paul, for their unconditional love, motivation, support, and guidance through life. I hope I have made you proud in who I have become and continue to do so on my path through life.

And finally, to my beloved wife, Dr. Tahereh Majdi, for her steadfast support of me and who without this work would not be possible in the very

literal sense. She has consistently been an impactful academic and technical collaborator through the discussion of problems and concepts to come up with and implement solutions. She has contributed directly to my work and success in life not only as my emotional bedrock and inspiration when all hope seemed lost, but also by her direct contribution of knowledge towards this and all my projects, including the painstaking task editing of my jumbled thoughts. I cannot imagine this journey without her, she has shaped me into the man I am today. Thank you for all the love, unending motivation and believing in me even when I did not.

I dedicate this work to my family and friends,
those here with me today and those forever in my heart.

Table of Contents

Abstract	iii
Acknowledgements	v
List of Figures and Tables.....	x
List of Abbreviations and Symbols	xii
1 Background	1
1.1 Introduction	1
1.2 Conventional Thin Film Growth.....	4
1.2.1 Homoepitaxy	4
1.2.2 Heteroepitaxy	7
1.2.3 Thin Film Growth Modes	10
1.2.4 Strategies to Combat Heteroepitaxial Misfit	11
1.3 Sapphire as a Substrate.....	15
1.4 Thesis Overview.....	21
2 Incommensurate van der Waals Heteroepitaxy and Weak Chemical Interaction	24
2.1 Relevant Literature and Previous Work	24
2.2 Experimental Methods and Details	27
2.2.1 Pulsed Laser Deposition.....	27
2.2.2 Electron Microscopy	31
2.2.3 X-ray Diffraction and Texture Analysis	35
2.2.4 Substrate Preparation and Growth	39
2.3 Results and Discussion.....	40
2.4 Conclusions.....	57
3 Transfer Methods for Epitaxial Thin Films	59
3.1 Relevant Literature and Previous Work	59
3.2 Experimental Methods and Details	66
3.2.1 Photoluminescence Spectroscopy.....	66
3.2.2 Substrate Preparation and Growth	66
3.3 Results and Discussion.....	68
3.3.1 Film Structural and Optical Quality after Layer Transfer	68
3.3.2 Layer Transfer Methodologies: Challenges and Solutions.....	74

3.4	<i>Conclusions</i>	90
4	GaAs on Oxide Preliminary Growth Study	92
4.1	<i>Relevant Literature and Previous Work</i>	92
4.2	<i>Experimental Methods and Details</i>	94
4.2.1	Molecular Beam Epitaxy	94
4.2.2	Substrate Preparation and Growth	96
4.3	<i>Results and Discussion</i>	98
4.3.1	Structural Analysis of GaAs Films on Oxide Substrates	98
4.3.2	MELO of GaAs from Oxide Substrates	106
4.4	<i>Conclusions</i>	112
5	Epitaxial Thin Film Transfer for Flexible Heterostructure Devices	115
5.1	<i>Relevant Literature and Previous Work</i>	115
5.2	<i>Experimental Methods and Details</i>	118
5.2.1	Current Density-Voltage Measurements	118
5.2.2	CdTe HIT Heterostructure Design and Growth	119
5.2.3	Two Side Processed GaAs Device Design and Growth.....	124
5.3	<i>Results and Discussion</i>	127
5.3.1	CdTe Heterostructure J-V Characteristics.....	127
5.3.2	Layer transferred GaAs Device J-V Characteristics	141
5.4	<i>Conclusions</i>	145
6	Conclusions and Future Work	147
6.1	<i>Contribution Summary</i>	147
6.2	<i>Future Work</i>	150
6.2.1	Process Improvements for Layer Transferred Devices	150
6.2.2	Refinement of GaAs (111)/ α -Al ₂ O ₃ (0001) and Interfacial Study	151
6.2.3	Compliant Chalcogen Interlayers for Other Material Systems	152
7	References	154
8	Appendix	162
8.1	<i>Optical and Electrical Characterisation of ZnO Films</i>	162
8.2	<i>Optical and Electrical Characterisation of ZnTe:N Films</i>	163

List of Figures and Tables

Figure 1: Bandgap vs. lattice constant for a variety of semiconductor materials..	2
Figure 2: Common kinetic processes involved in epitaxy.....	5
Figure 3: The effects of heteroepitaxial strain on the unit cell.	9
Figure 4: Thin film nucleation modes.	10
Figure 5: Heteroepitaxial approaches to overcome lattice mismatch.	13
Figure 6: A ball and stick model of the unrelaxed unit cell of α -Al ₂ O ₃	17
Figure 7: A schematic representation of the PLD growth chamber	29
Figure 8: Representation of electron beam interacting with a specimen.....	32
Figure 9: Bragg diffraction condition for a periodic crystal lattice.	37
Figure 10: Example (111) pole figures.	38
Figure 11: Epitaxial orientation of CdTe on the basal plane of sapphire.	41
Figure 12: Strain relaxed, high quality CdTe heteroepitaxy on Al ₂ O ₃	42
Figure 13: CdTe film polarity and sapphire surface termination.....	43
Figure 14: EELS O K edge comparison for bulk and surface of sapphire.	45
Figure 15: EELS area and line scans of CdTe/Al ₂ O ₃ interface.....	46
Figure 16: Milling induced necking at the film-substrate interface.	48
Figure 17: STEM micrograph and atomic model of CdTe-Al ₂ O ₃ interface.....	49
Figure 18: Low-loss EELS plasmon feature unique to the interface.	51
Figure 19: Overgrown stacking fault at CdTe-Al ₂ O ₃ interface.	53
Figure 20: Domain preference for CdTe/Al ₂ O ₃ with additional Te interlayers.....	56
Figure 21: Conventions and geometries for the cracking of brittle substrates....	64
Figure 22: PL and XRD comparison of films prior and post layer transfer.....	70
Figure 23: RT PL comparison of thick and thin CdTe (111)/Al ₂ O ₃ (0001) films.....	73
Figure 24: Reusability of sapphire substrate post layer transfer.....	74
Figure 25: Illustration of gas entrapment during lamination.	78
Figure 26: PSU spin coating Si and preliminary adhesion tests.....	80
Figure 27: Illustration of poor metal adhesion during layer transfer.....	83
Figure 28: Patterned CdTe heterostructure layer transfer to PSU.	84
Figure 29: Interpolated thickness of graded platinum deposition.	86
Figure 30: Illustration of layer transfer and substrate reuse process flow.	89
Figure 31: A schematic representation of the MBE system.	95
Figure 32: Simulated pole figures of GaAs and three oxide substrates.	99
Figure 33: Polycrystalline GaAs on YAG substrates.	100
Figure 34: Summary of GaAs (111) on spinel pole figures.....	101
Figure 35: Summary of GaAs (111) on sapphire pole figures.	102
Figure 36: FWHM of GaAs (111) peaks on oxide substrates.	103
Figure 37: Change in 2θ for GaAs films grown on oxide substrates.	105
Figure 38: α -Al ₂ O ₃ (10-2) pole figure for GaAs grown at 525°C.....	106

Figure 39: GaAs layer transfer attempts to polysulfone carrier.....	108
Figure 40: Thermomechanical spalling of spinel and YAG substrates.....	110
Figure 41: Schematic layer transferred CdTe heterostructures.....	120
Figure 42: Proposed CdTe HIT heterostructure band diagram.....	121
Figure 43: Schematic GaAs Diode on oxide substrate structure.....	125
Figure 44: Predicted GaAs layer transfer device band diagram.....	127
Figure 45: Generation one CdTe heterostructure device, photoresistor.....	129
Figure 46: Generation one CdTe heterostructure device, whisker contacted..	131
Figure 47: Generation two CdTe, heterostructure, dark rectification.....	133
Figure 48: Log dark current-voltage plot for generation one device.....	134
Figure 49: Generation two CdTe, heterostructure, photovoltaic activity.....	135
Figure 50: Generation two CdTe heterostructure, negative resistance.....	137
Figure 51: Simulated J-V characteristics of and ideal CdTe heterostructure.....	139
Figure 52: Generation three CdTe heterostructure.....	141
Figure 53: GaAs Device A, photoresistor.....	142
Figure 54: GaAs Device B, small photovoltaic response.....	143
Figure 55: GaAs Device C, largest V_{oc}	144
Figure 56: Table summary of CdTe heterostructure PV characteristics.....	145
Figure 57: Table summary of GaAs PV characteristics.....	146
Figure 58: Optical characterization of ZnO and ZnO:Al films.....	162
Figure 59: Summary table of ZnO and ZnO:Al electrical characterization.....	162
Figure 60: Optical characterization of ZnTe films.....	163
Figure 61: Summary table of ZnTe:N electrical characterization.....	163

List of Abbreviations and Symbols

2D	Two Dimensional
3D	Three Dimensional
3DXRD	Three-Dimensional X-ray Diffraction
Al ₂ O ₃	Aluminum Oxide, i.e. sapphire, corundum
CdTe	Cadmium Telluride
CuTe	Cupric Telluride
DFT	Density Functional Theory
EELS	Electron Energy Loss Spectroscopy
FF	Fill Factor, i.e. the product of voltage and current of a device at maximum power output divided by the product of open circuit voltage and short circuit current density
FIB	Focused Ion Beam
FWHM	Full Width Half Maximum
HAADF	High Angle Annular Dark Field
IRV	Interfacial Recombination Velocity
J _{sc}	Short Circuit Current Density, i.e. short circuit current divided by active device area
J-V	Current Density-Voltage
LAADF	Low Angle Annular Dark Field
LN ₂	Liquid Nitrogen
MBE	Molecular Beam Epitaxy
MELO	Mechanical Epitaxial Lift Off
MgAl ₂ O ₄	Spinel
MOCVD	Metal Organic Chemical Vapour Deposition
PL	Photoluminescence
PLD	Pulsed Laser Deposition
PSU	Polysulfone
R _s	Specific Series Resistance, i.e. resistance per device area impeding the flow of light-generated current in series to performing work outside the cell
R _{sh}	Specific Shunt Resistance, i.e. resistance per device area providing loss path for light-generated current parallel to performing work outside the cell
RT	Room Temperature
STEM	Scanning Transmission Electron Microscopy
TEM	Transmission Electron Microscopy
T _g	Glass Transition Temperature

vdW	van der Waals
V_{oc}	Open Circuit Voltage, i.e. the voltage generated by the device under no load
XRD	X-ray Diffraction
YAG	Yttrium Aluminum Garnet
ZnTe	Zinc Telluride
η	Efficiency, i.e. device output at maximum power point divided by input irradiance.

1 Background

1.1 Introduction

High-quality crystalline semiconductors are a key component in the production of a variety of electronic and opto-electronic devices. A high-quality semiconductor material is not one that is idealistically perfect, since crystalline materials do not exist without some imperfection. In practise, the opto-electronic properties of a device depend both on the material of interest and on the defects that exist in the system such as surface states, grain boundaries, vacancies, and native or impurity substitutions and interstitials. Control of defects through manufacturing and processing allows for both the minimization of unwanted and incorporation of favourable defects, such as dopants, to produce a device with target characteristics.

A predominate industrial process to fabricate high-quality semiconductor materials is through the production of bulk wafers. Only a small subset of material systems, given the breadth of available semiconductors as demonstrated by the variety presented in Figure 1, offer diameters and costs which allow for large scale device fabrication. Further, there are technical limitations in producing large wafers for some materials due to their thermal and mechanical properties.^[1,2] As such, the infrastructure to achieve economies of scale for the vast number of binary

and ternary semiconductor systems does not exist despite possessing technologically relevant material characteristics. For these material systems heteroepitaxial thin film growth can provide an alternative or complementary approach to bulk wafer processing.

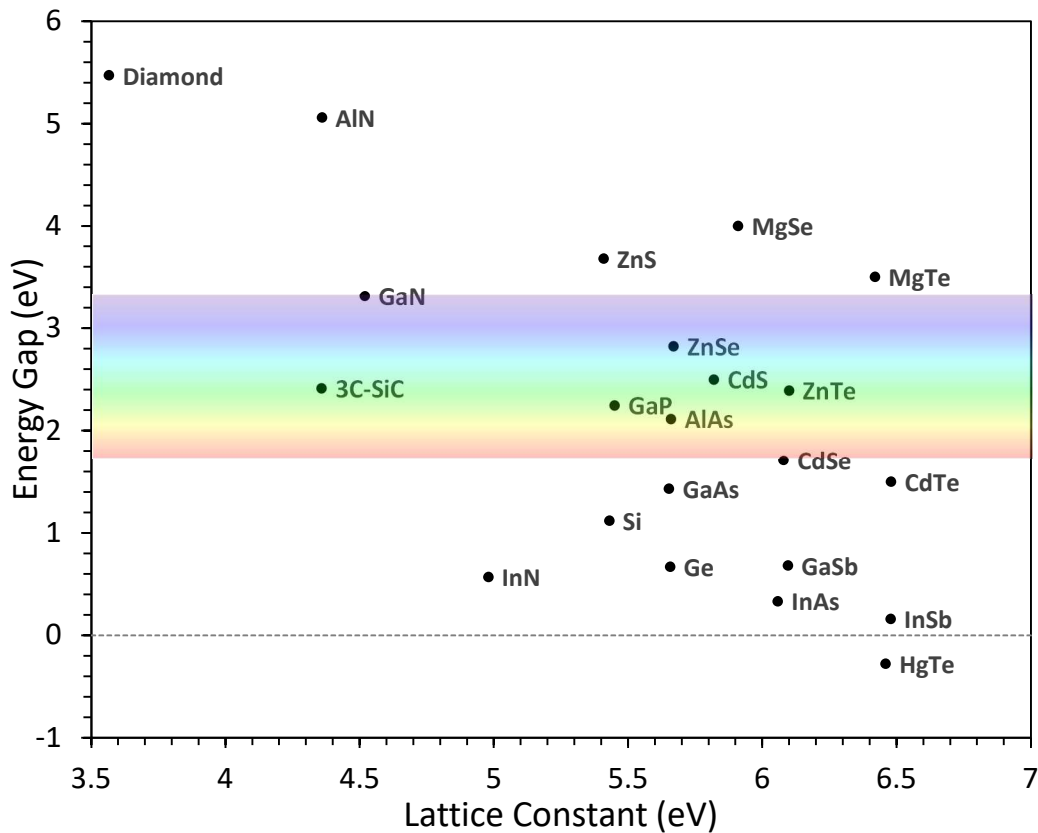


Figure 1: Bandgap vs. lattice constant for a variety of semiconductor materials. Adapted from Montanari.^[3]

A caveat of the direct heteroepitaxial approach to produce monolithically integrated devices from dissimilar materials is requirement of a lattice matched substrate for the thin film. When these substrates exist, they comprise a significant portion of the device cost and often possess non-ideal, even detrimental properties, for device performance.

This problem is further complicated by thermal and lattice strains between dissimilar materials arising during growth which must be overcome to prevent the generation of defects in the active material layer. An emerging class of thin film device technology has focused on the creation of free-standing thin films and/or the layer transfer of thin films to a target carrier substrate with ideal properties for device integration. This methodology offers several processing advantages compared to their direct growth on substrate counterparts for devices such as, but not limited to, flexible electronics, photovoltaics, and lasers.^[4–6] The primary motivation behind such technologies is the promise of higher efficiency optoelectronic devices and increased integration of photonic devices with silicon-based integrated circuits.

In this chapter the fundamentals related to conventional epitaxial approaches are introduced and growth mechanisms are discussed. This includes a discussion of the conventional approaches to overcoming heteroepitaxial misfit strain. Epitaxy on the complex oxide sapphire is introduced, highlighting key differences from epitaxy on some common group IV and group III-V semiconductor substrates due to the unique properties of sapphire and its surface. The chapter concludes with a thesis overview.

1.2 Conventional Thin Film Growth

1.2.1 Homoepitaxy

Epitaxy, from the Greek root words epi, above, and taxis, an ordered manner, has been the dominant technology for developing a variety of modern optoelectronic devices. As the name implies, it involves the deposition of a crystalline material on a crystalline substrate, which it uses as a template for its crystallographic orientation. Epitaxy can be classified into two main processes: the growth of the same material as the substrate, homoepitaxy, or the growth of a dissimilar material to the substrate, heteroepitaxy. The least complex of the two is homoepitaxy, since it is a process between materials which share a congruent crystal structure, lattice constant and chemistry.

Under ideal growth conditions, homoepitaxy allows for the growth of a high-quality single crystalline epilayer. These conditions consider the reaction kinetics and thermodynamics of growth. Reaction kinetics deal with the various rates of interaction for the growth process, while the thermodynamics deal with the direction-in-which and extent-to-which processes occur. A bottom-up growth process of simple adatom interactions on a substrate is illustrated in Figure 2. Obtaining an ideal growth condition for a system involves the control of such interactions by

optimizing parameters such as the material deposition rate and system temperature.

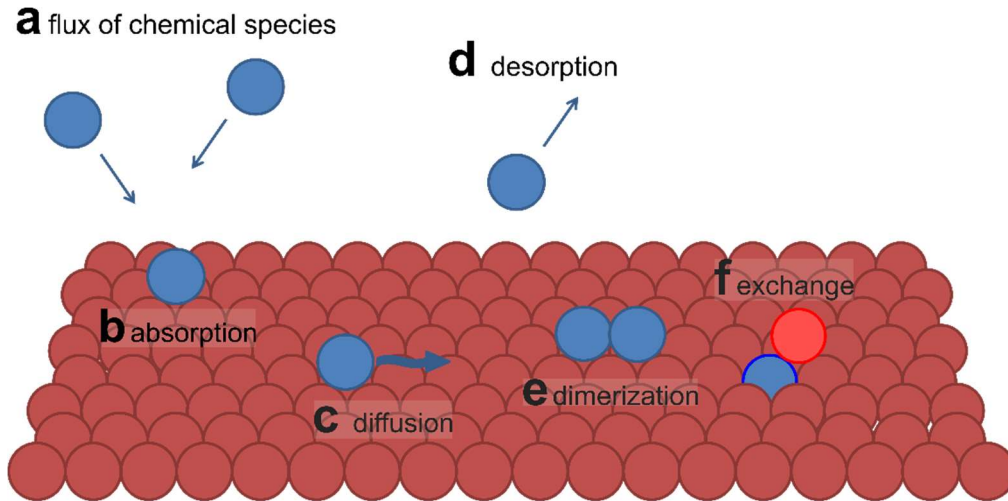


Figure 2: Common kinetic processes involved in epitaxy. Chemical reaction rates take on an Arrhenius form. (a) A variety of processes at different rates may occur for flux of chemical species impinging a surface. (b) For an absorption event from the flux, that adatom may diffuse (c) or desorb (d) along and from the surface, respectively. Two adatoms which are absorbed and diffuse on the surface may aggregate and interact with one another to bond and dimerize (e). Bound aggregates may dissociate, or successive aggregation may form layers or islands of bound adatoms. An adatom may also diffuse into the substrate, through a process of exchange (f).

A flux of chemical species, which can consist of atoms, molecules and/or ions, impinges the substrate surface at a constant rate; for simplicity, in Figure 2, a flux of atoms is considered. Atoms impinging the surface may be absorbed onto that surface and those adatoms then undergo stochastic movement from their absorbed position to lower energy positions through a surface diffusion process. Some adatoms will desorb from the surface, while others will aggregate with other adatoms. Molecular species adsorbed to the surface may first dissociate into smaller constituents which then diffuse on or desorb from the substrate. Diffusion

into the bulk substrate of an adatom by exchange with a substrate atom or an interstitial position may also occur.

Reaction rates of the chemical process such as absorption, desorption, diffusion, dimerization, and exchange are Arrhenius in nature. While the material system of interest determines the pre-factors and activation energy of the processes, the experimenter can influence these rates by changing the growth temperature. The impingement rate and growth rate can also be controlled by varying the flux of chemical species per unit time.

For situations with large growth rates, absorbed species may not have the time to move into the thermodynamically lowest energy position resulting in amorphous or polycrystalline film growth. This can be combated by increasing the mobility of species on the surface, by increasing the growth temperature, or by decreasing the flux of species. Some chemical process rates, such as absorption and desorption, operate in juxtaposition of one another with increasing temperature. As a result, optimized growth for epitaxy is a balance between growth rate and substrate temperature; in more complicated deposition processes additional energy may also be delivered directly to the flux of species prior to absorption, such as by plasma enhancement, resulting in additional experimental controls for growth.^[7]

1.2.2 Heteroepitaxy

For the above discussion, the deposited species and substrate material system was assumed to be homogenous. However, in the case of heteroepitaxy, where the material systems are heterogenous, there are additional considerations. The choice of a heterogenous system may be a consequence of the limited set of commercially available bulk substrate wafers,^[1] or to take advantage of the properties of a combined material system.^[8] Integrating dissimilar materials with defect-free interfaces has been one of the greatest hurdles to, but also fundamental in, the development of modern electronic and optoelectronic devices. Material systems for high quality heteroepitaxy, however, have been limited to those with similar chemical bonding, lattice symmetry and lattice constants.

One central concept to the discussion of heteroepitaxy is lattice mismatch. For a heteroepitaxial material system, exhibiting strong chemical bonding across the interface, a lattice mismatch of substrate and film will lead to a crystallographic distortion from their equilibrium lattice spacings. The resultant strain, associated with the tension or compression of chemical bonds, is called the misfit strain and is given by Equation 1.^[9]

$$\epsilon_{lattice} = \frac{a_s - ra_f}{a_s} \quad \text{Equation 1}$$

In this definition of misfit strain, positive and negative mismatch values indicate film tension and compression, respectively. The ratio parameter, 'r', represents the number of unit cells of the film material which when placed laterally together are closest to the length of one substrate unit cell. This parameter is a rational number for systems which have the same symmetry, e.g. cubic on cubic, or non-rational number for systems which have different crystal symmetries, e.g. cubic on hexagonal.

The effects of heteroepitaxial tensile and compressive strain on the unit cell of a thin film being deposited are illustrated in Figure 3. For a lattice mismatched system, the lattice of the film first accommodates strain elastically such that it maintains the lattice constant of the substrate in-plane and modifies its out-of-plane lattice constant in accordance with Poisson's ratio. This is referred to as pseudomorphic growth.^[10,11] As additional film accumulates the strain energy increases until a critical point in which strain is relieved plastically and the film relaxes so that the system energy is minimized by the introduction of defects such as dislocations.^[12,13]

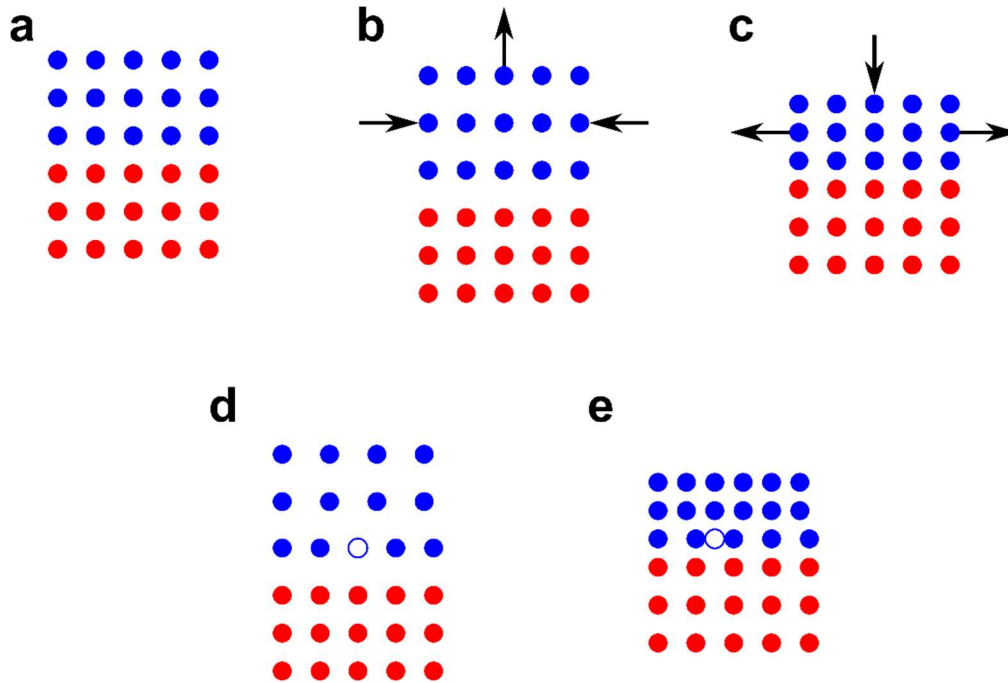


Figure 3: The effects of heteroepitaxial strain on the unit cell. The epitaxial film is shown in blue and the substrate in red. (a) Illustration of homoepitaxy or perfect lattice matched epitaxy with no strain. Growth of dissimilar epitaxial materials can lead to compressive (b), or tensile (c) elastic strain where growth is initially pseudomorphic. As strain, and thus energy, increases inside the epitaxial film beyond a critical point it is relieved to minimize the system energy. This results in the introduction of defects such as dislocations, indicated by open dots, to relax compressive (d) and tensile (e) strain plastically.

The critical thickness depends on the degree of mismatch between the film and substrate, as well as the mechanical properties of the material such as its Young's and shear modulus. Strain modifies the thin film band structure, which may be beneficial or detrimental,^[14,15] creates defects, which are detrimental to the device,^[16,17] and may even lead to the fracture of the thin film and/or substrate.^[18,19] The substrate interface is also subject to strain from lattice misfit to the thin film and responds oppositely to the film to balance the forces given its own elastic and plastic

properties. A more detailed discussion of the film and substrate fracture response is included in section 3.1.

1.2.3 Thin Film Growth Modes

As enough absorbed species begin to accumulate on a substrate's surface, they begin to interact with each other and the substrate to form a film-substrate interface. Nucleation of an epitaxial crystal at this interface is a complex function of the thermodynamics and kinetics of growth, but also the strain and chemical interaction between the film and substrate. Generally, there are three major categories of nucleation and growth for thin films: layer-by-layer (Frank van der Merwe), island growth (Volmer-Weber) and layer-plus-island (Stranski-Krastanov),^[20] as illustrated in Figure 4.

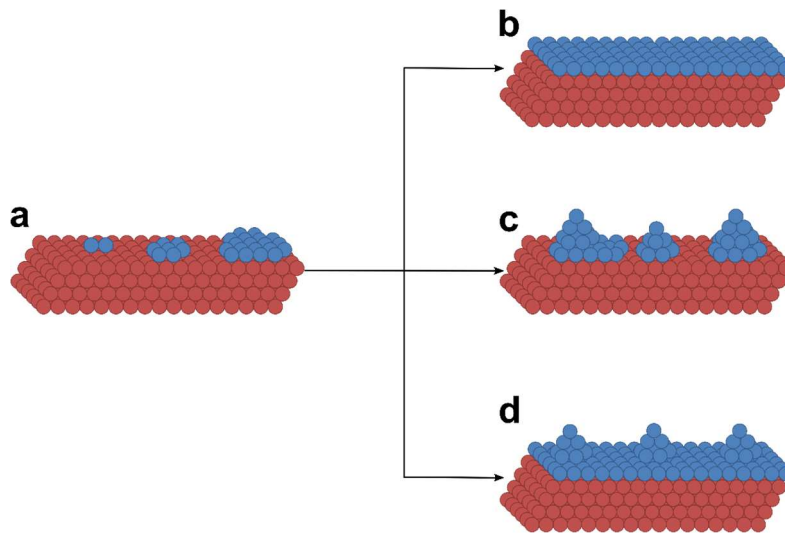


Figure 4: Thin film nucleation modes. (a) As adatoms aggregate on the surface, strain, and chemical bonding influence the growth mode. The three basic growth modes include Frank-van der Merwe (b), Volmer-Weber (c) and Stranski-Krastanov (d) growth. These are also referred to as layer-by-layer, island, and layer-plus-island growth, respectively.

Layer-by-layer growth occurs for material systems in which the interaction between adatoms and the substrate (adhesion) is much larger than the interaction between adatoms on the surface (cohesion) such that a next layer will grow only after the layer before it is completed. This tends to occur for systems which are chemically compatible and are minimally strained.^[21] Island growth occurs for systems when the cohesion interaction of adatoms is larger than the adhesion interaction of adatoms to the substrate,^[22] such as those which are highly strained or chemically dissimilar and non-interacting. The islands may eventually coalesce.

A mixed mode of nucleation, layer-plus-island, can occur when the interfacial energy favouring adhesion changes to cohesion during growth. This can be caused by changes in the strain energy or lattice distortions beyond a critical thickness.^[22] Stranski-Krastanov growth may even be intentionally induced in some systems by changing the growth parameters during deposition.^[23]

1.2.4 Strategies to Combat Heteroepitaxial Misfit

As previously mentioned, one of the major challenges of heteroepitaxy is strain caused by lattice mismatch.^[12] Differences in the thermal expansion coefficient between the film and substrate, further compound strain complexities. Since the lattice parameters for the material are temperature dependent, the film-substrate system may

experience different thermal strains at the growth temperature and while cooling to room temperature after growth. While elastically strained heteroepitaxial layers can be grown up to a critical thickness,^[24,25] beyond that thickness plastic strain relaxation creates dislocations, that act as carrier recombination centres, which negatively impact the optoelectronic quality of the device.

A variety of strategies to combat this and develop high quality heteroepitaxial devices have been researched,^[26] and an illustration of these approaches is summarized in Figure 5. Metamorphic growth employs the use of a compositionally graded, thick buffer layer between the substrate and active film region which allows for a gradual change in lattice match and strain to be accommodated elastically.^[27] Buffer layers may also be used to confine dislocations and defects to the buffer region, accommodating the lattice mismatch between the active layer and substrate.^[28]

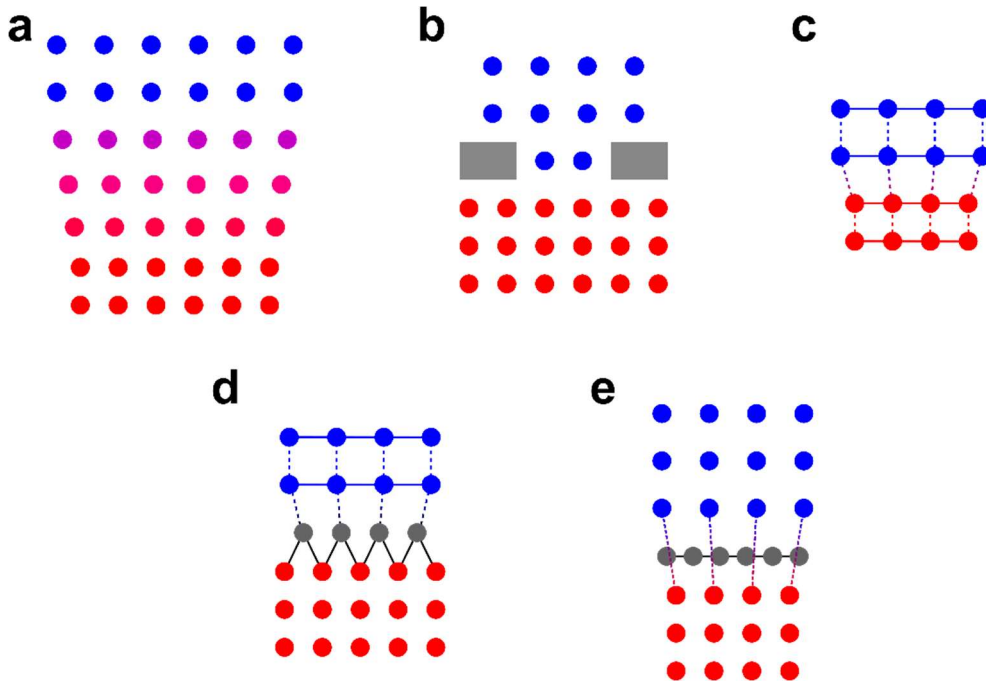


Figure 5: Heteroepitaxial approaches to overcome lattice mismatch. (a) Illustration of metamorphic growth, for which the substrate, red, and epitaxial film, blue, have different lattice constants. A buffer of compositionally graded material is used to gradually change the lattice constant from that of the substrate to that of the film. In some cases, an amorphous buffer layer is used, which accommodates strain from the lattice mismatch between substrate and film. (b) Illustration of lateral overgrowth method. An inert buffer material, such as an oxide, is used to define small areas where heteroepitaxy can occur. Defects are localized to these holes in the buffer and the film grows laterally into a complete film. (c) Illustration of vdW epitaxy of a 2D material on a 2D substrate. Strong bonding, as indicated by solid lines for the substrate and film, occur in-plane. Weak vdW bonding, indicated by the hashed lines, occur out-of-plane and accommodate lattice mismatch. A 2D material can also be deposited on a conventional 3D substrate by vdW epitaxy, (d) by modifying the surface with a certain passivation. The grey atoms strongly bond to the surface of the substrate, as indicated by the dark black lines, and present only weak vdW bonds for the epilayer. (e) An illustration of remote epitaxy of a 3D film on a 3D substrate. The substrate surface is modified by transferring an intermediate layer of 2D material, such as graphene, which allows for weak heteroepitaxial interaction governed by substrate polarity.

Lateral overgrowth is a method where a buffer material, which is only weakly or non-chemically interactive with the adatoms, is used to cover most of the substrate surface except for a few exposed regions where heteroepitaxy can occur. Often this buffer material is a dielectric, like an

oxide or nitride, and confines dislocations to the exposed substrate area, where additional nucleating film overgrows laterally above the buffer layer and then out-of-plane to increase the thickness of the film.^[29]

With the emergence of research in the field of two dimensional (2D) materials and devices, it has been demonstrated that the lattice matching requirement is diminished for a van der Waals (vdW) heteroepitaxial system due to weak interlayer bonding, but strong intralayer bonding.^[30,31] A 2D material substrate has no dangling bonds on its surface, but strong cohesive bonds between atoms in the sheets, and thus provides only weak vdW bonds to adatoms during deposition.

If the deposited adatoms will not reduce or oxidize the 2D substrate, and they form a 2D heteroepitaxial material whose interlayers are normally also held together by weak vdW forces, heteroepitaxial strain is accommodated immediately at the interface between the two 2D layers, allowing them to be incommensurate. 2D heteroepitaxial systems can also be grown on the surface of a three dimensional (3D) substrate if it can be passivated chemically such that it also provides weak vdW bonds for its 2D layer film.^[32–34] This is helpful for the development of large area 2D devices due to the lack of readily available large area 2D bulk substrates.

An even more recent strategy to overcome the challenges with heteroepitaxial mismatch is by employing a technique called remote epitaxy. Remote epitaxy is a process by which a 2D material interlayer,

such as graphene, is transferred to a surface of a conventional 3D substrate and then a 3D thin film is grown on top of the passivated surface.^[35] Due to the transparency of ultrathin 2D materials to some intermolecular interactions, adatoms demonstrate some Coulombic interaction with the substrate allowing for epitaxial registry without the direct formation of rigid bonds which lead to misfit strain.^[36] This weakened interface allows for the spontaneous relaxation of the system.

Remote epitaxy will be discussed in more detail in section 2.1, however, it should be noted that remote epitaxy has not yet been scaled to large wafer scale devices due to technological complications such as pinholes and surface contamination associated with the wet transfer method used on the 2D interlayer.^[37,38]

1.3 Sapphire as a Substrate

Sapphire, the α - Al_2O_3 crystalline form of corundum, is a unique substrate material due to its stable chemical and mechanical properties. It has trigonal crystal symmetry, belonging to the centrosymmetric space group 216 ($R\bar{3}c$), with an 'a' lattice parameter of 4.760 Å and 'c' lattice parameter of 12.993 Å.^[39] Due to its centrosymmetry, sapphire does not exhibit the piezoelectric effect and is non-polar.

Referring to Figure 6, the three-fold symmetric axis is designated the c-axis, presenting the c-plane (0001) consisting of two equal triangles

forming a rhombus. This is also referred to as the basal plane.

Perpendicular to this are the a-axis and m-axis, each being two-fold symmetric and rectangular in shape. Following the c-axis, viewed perpendicular to the a-plane, a repeated layer structure of aluminum and oxygen is visible in the sapphire truncated unit cell. The bonding between the aluminum cations and the oxygen anions is strong and mostly ionic, which creates an alternating charge distribution corresponding to the layered structure.

Sapphire's crystal structure and tight bonding gives it a variety of useful properties such as its mechanical stability seen in its hardness of 9 on the Mohs scale, second to diamond for the hardest material. Additionally, it has a dielectric constant, resistivity, thermal conductivity and band gap of 9.39, $\sim 10^{14} \Omega \cdot \text{cm}$, $0.46 \text{ W/cm} \cdot \text{K}$ and 9.1 eV , respectively, making it a superior insulator to silicon dioxide.^[40,41] Due to these properties it has become an important substrate for modern electronic and optoelectronic devices, seeing applications in silicon-on-sapphire (SOS), GaN and ZnO technology.^[40,42,43]

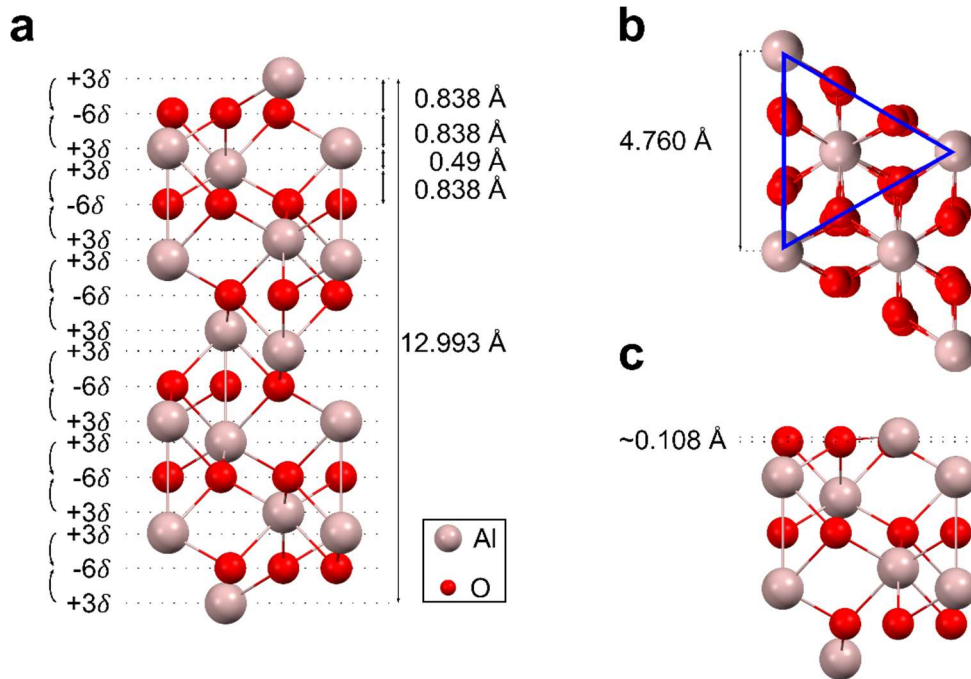


Figure 6: A ball and stick model of the unrelaxed unit cell of $\alpha\text{-Al}_2\text{O}_3$. (a) A projection shown along the a -axis. Sapphire has a hexagonal crystal structure and is in space group $R\bar{3}c$. Its ' c ' lattice constant is 12.993 \AA as shown. Due to the crystal symmetry in its space group, sapphire is centrosymmetric and therefore non-polar despite the ionic nature of its bonds. The balanced redistribution of charge in the c -direction is shown. Viewing instead along the c -axis (b), the ' a ' lattice constant of 4.760 \AA is shown. Sapphire's surface net presents a rhombus made of two equal triangles to adatoms. (c) A relaxed half unit cell of $\alpha\text{-Al}_2\text{O}_3$ illustrates a substantial inward relaxation of the outmost aluminum atom to screen its charge.

The growth of thin film material, such as CdTe, on sapphire presents unique epitaxial and interface complications compared to epitaxy on traditional group IV or III-V bulk semiconductor substrates; three of which will be considered below: surface net symmetry mismatch, relatively weak chemical interaction, and sapphire's surface reconstruction stability. Firstly, from a purely geometrical sense, sapphire's basal plane surface net presents six-fold symmetry. Since zinc blende CdTe films have a well-established propensity to form their (111) plane parallel to the growth

substrate,^[44] a CdTe thin film with three-fold symmetry has two equal and opposite possible domain orientations with respect to the c-plane of sapphire. This does not occur for wurtzite materials, such as GaN and ZnO,^[45,46] grown on Al₂O₃ (0001) substrates or for Si (100) films grown on Al₂O₃ (1 $\bar{1}$ 02) substrates where the cubic crystal structure of silicon aligns with a square surface net arrangement of oxygen atoms of similar lattice spacing.^[47]

Secondly, conventional 3D/3D epitaxial systems rely on strong chemical interactions, such as covalent, ionic, or metallic bonding, to transmit epitaxial information between the substrate and thin film. As discussed previously, the resultant bond lengths and angles between the dissimilar material systems leads to strain in the heteroepitaxial system and strain defects beyond a critical thickness.^[12] For material systems such as Si and ZnO on sapphire, silicon and zinc atoms form bonds with oxygen, respectively.^[47,48] Alternatively, material systems like GaN and ZnO on sapphire (0001) substrates which have undergone nitridation,^[49,50] require the production of an AlN interfacial layer to support the subsequent epitaxy.

However, weak film bonding on oxide substrates, such as Al₂O₃, has long been a topic of study due to issues with adhesion, particularly for metal adatoms, which lead to low contact shear strengths and film delamination.^[51,52] A direct chemical bond for an adatom on a substrate

can be thought of as the combination of covalent (charge sharing) and ionic (charge transfer) components. Unlike strong chemical bonding, weak bonding occurs when the contribution of electron occupation of antibonding orbitals negates the effects of the occupied bonding orbitals and thus covalent bonding, leaving only residual ionic and van der Waals contributions.^[51] Since residual ionic bond strength is proportional to the electronegativity between the adatom and substrate atoms to which it bonds, it is possible to have adatom-substrate bonding which is mostly van der Waals, referred to as physisorption. Given the relatively weak binding of cadmium and tellurium metallic adatoms predicted on $\alpha\text{-Al}_2\text{O}_3$ (0001) substrates,^[53] CdTe epitaxy on sapphire may proceed from a weakly bonded interface.

Lastly, for a crystal substrate of finite size the surface upon which epitaxy will occur represents a truncation of the crystal. Due to unsatisfied bonds and unbalanced charge, atoms which comprise the surface will be at a higher energy state compared to those in the bulk.^[54] If this higher energy state is not the equilibrium state, atoms near a surface will reconstruct to a more stable lower energy configuration. Some material systems have complex surface reconstructions, such as silicon and gallium arsenide,^[55,56] which depend on the crystal surface orientation, temperature and chemical environment, such as vacuum or the presence of chemical species. A much simpler reconstruction, and wide plateau of

reconstruction stability, occurs for Al_2O_3 (0001) by the movement of aluminum surface atoms from their bulk position, into the oxygen layer below as seen in Figure 6c to allow for charge screening. The most energetically favourable c-plane reconstruction of sapphire, a single Al-terminated surface, is non-polar and expected to be stable and lacking dangling bonds below 1400°C in vacuum.^[57,58] This stability allows its surface to form atomically flat terraces for subsequent thin film growth.^[59]

As adatoms arrive on a relaxed reconstructed substrate surface during epitaxy, given the thermodynamics and kinetics of growth, the surface reconstruction can become dynamic. For example, homoepitaxial growth can be thought as deposition on a reconstructed surface which translates forward with the new growth surface. As new adatoms arrive, the surface atoms will break their surface bonds to interact with adatoms and form additional epitaxial layers, where the newly formed surface then minimizes its energy by relaxation and reconstruction. During deposition of a heteroepitaxial system, atoms in the reconstructed surface will break bonds to form new bonds or interchange with adatoms forming an abrupt or diffuse interface which satisfy bonds and charge to minimize the system energy. Further, for polar on non-polar heteroepitaxy, such as for GaAs on germanium or silicon, balances of the surface charge at the interface are resolved by an atomic exchange between Ga and As adatoms and with atoms in the reconstructed Ge or Si surface.^[60]

This is not the case for the c-plane of sapphire, at growth temperatures well below 1400 °C, which is not expected to provide dangling bonds, unshielded charge, polarity or to break its surface bonds to form new bonds with adatoms easily. Consequently, adatoms can only interact with the local weak chemical environment of the surface and satisfy any unbalanced charge, polarity, or dangling bonds by only changes to the local surface structure in the film to that interface. As such, a CdTe (111)/Al₂O₃ (0001) interface is an interesting heteroepitaxial system since it must resolve a polar film and non-polar substrate system without significant surface reconstruction of, or chemical interaction, with the substrate surface.

1.4 Thesis Overview

This thesis presents a study of the CdTe/Al₂O₃ system using microscopy and X-ray diffraction (XRD) techniques. Analysis of these results is used to create a model of the interface which postulates why the system has sufficiently strong interaction for heteroepitaxial alignment but has weak enough adhesion interaction such that inherent stress caused by heteroepitaxy and additional thermomechanical stress can be used to separate the film from the substrate at the interface. Since the layer transferred thin films retain their optical and structural properties following the transfer process, further work presented in this thesis develops the

mechanical process of transferring epitaxial thin films from their oxide substrates and investigates this mechanism as a means to produce simple lifted-off semiconductor devices.

In addition to the results and discussion of each chapter topic, the following core four chapters contain a summary of relevant literature and previous work, as well as the experimental methods and details as they relate to their respective chapter. Chapter 2 studies the interface of the CdTe/Al₂O₃ material system, revealing a 3D/3D vdW-like epitaxial interface. The interface is predominately studied through electron microscopy techniques, which is analysed and used to create an interface model consistent with X-ray diffraction and observations of the ease of film delamination. This work was submitted for publication in *Small*.^[61]

Chapter 3 presents a more detailed study of the layer transfer methods to create flexible devices and the processes required for robustness to overcome layer handling challenges. Part of this work was previously published in *Materials Research Express*,^[62] combined with IV characteristics from devices fabricated and presented in Chapter 5. Chapter 4 studies secondary semiconductor/oxide material systems, GaAs on sapphire, spinel and yttrium aluminum garnet as candidates which also exhibit the ability to be layer transferred. First, a preliminary film growth quality refinement was performed and then the previously developed layer transfer techniques discussed in Chapter 3 were applied, revealing a

successful layer transfer method for a GaAs thin film from an oxide substrate.

Chapter 5 studies the utilization of the layer transfer technique developed to create simple proof-of-concept rectifying and photoactive devices by processing both sides of the thin film to create a heterostructure device. This takes advantage of access to the previously inaccessible buried interface surface. The devices presented have either CdTe or GaAs active absorber layers. The light and dark current density-voltage characteristics for these devices are probed and compared with some device modeling to provide insight into the devices' behaviours. Lastly, chapter 6 presents the conclusions of the work and potential future steps that could be taken as related to the thesis topic.

2 Incommensurate van der Waals Heteroepitaxy and Weak Chemical Interaction

2.1 Relevant Literature and Previous Work

To overcome strain dislocation defects in heteroepitaxial systems, a variety of strategies have been employed to create strain compliant substrates or layers. Substrates modified to have a compliant interface, through defect engineering or intentional surface modification, prevent strain from traveling through the deposited thin film, reducing the system strain energy in the substrate or surface layers.

One such defect engineering mechanism is heteroepitaxy on nano-porous or amorphized interlayer coated substrates,^[63] which involves the low temperature deposition of a nano-porous interlayer, or ion implantation and amorphization or weakening of the surface and subsurface layers on the substrate. In these cases, the damaged, weakened, and porous interface layers accommodate strain plastically and elastically, trapping strain defects at the interface where the film overgrows the interface and achieves improved quality compared to a non-compliant interface. A notable recent example of the successful implementation of this strategy has been in the heteroepitaxial growth of GaAs on Si, using SrTiO₃ and amorphous SiO₂ buffer layers to create high speed transistors.^[28]

More recently, a compliant interlayer strategy for epitaxy relies on the layer transfer of graphene to a growth substrate called remote epitaxy.^[35,64] Due to weak interlayer bonding to the substrate, vdW heteroepitaxial systems have a reduced lattice matching requirement.^[31,32,65] However, the direct deposition of a 3D thin film on a 2D material, such as graphene, tends to form adatom clusters and instead suppress single crystal epitaxy when the islands coalesce. Remote epitaxy utilizes both a 2D interlayer and 3D substrate to provide long-range interaction, between the film and the 3D substrate, in addition to the weak interaction with the 2D interlayer.

This phenomenon was first observed in the wetting translucency of graphene, where a single layer of graphene was shown to transmit 30% of the water-substrate interactions, which influences the contact angle the water makes on the graphene as if it was interacting with the substrate.^[66] This implies the uniform weak binding 2D surface is modified by the substrate below to have regions of low and high potential energy for adatoms to preferentially bind. As such, while the 3D substrate in remote epitaxy does not form direct covalent or ionic bonds with the adatoms to grow a 3D film, due to the interlayer separation distance, it instead influences their epitaxial alignment and polarity remotely by Coulombic interaction.

Remote homoepitaxial growth of GaAs demonstrated that the weak van der Waals interactions of one graphene layer could not completely screen the potential fields of the substrate from the thin film, but it could prevent the film and substrate from forming strong covalent bonds, allowing for a high quality homoepitaxial film to be grown which can be easily layer transferred from the grow substrate.^[35] It was subsequently determined that while purely covalent bonding was screened by graphene, materials with ionic or partially ionic bonding could not be fully screened implying polarity governed the remote epitaxial interaction.^[36]

The remote epitaxy technique was expanded to and demonstrated in heteroepitaxial systems,^[64,67] where strain was shown to spontaneously relax at the film/vdW interface with graphene allowing films to grow incommensurately and strain relaxed with improved quality compared to their non-compliant interface counterparts. Films were also easily removed and transferred from their growth substrate due to weak interfacial bonding. However, such techniques have not translated well to wafer scale devices commercially. While the size of pristine 2D layers that can be produced and transferred has improved, it is still technologically limited by complications such as pinholes and surface contamination associated with the wet transfer method,^[37,38] as well as costs which limit scalability in manufacturing due to the required substrate pre- and post-processing.

However, a novel direct heteroepitaxial growth method of a 3D heteroepitaxial system on a 3D substrate is possible, discussed in this section and published in *Small*,^[61] which forms a spontaneous vdW-like bond at the interface without the need for a transferred 2D interlayer. This process for a spontaneously forming compliant interface integrates well into established semiconductor manufacturing processes and could be used to support subsequent epitaxy or produce layer transferred thin films for flexible electronics from reusable substrates.

2.2 Experimental Methods and Details

2.2.1 Pulsed Laser Deposition

Pulsed laser deposition (PLD) is a non-equilibrium physical vapor deposition technique,^[68] in which focused laser fluence is used to ablate a material's surface to create a plasma plume. Some major advantages of PLD compared to other physical deposition techniques are its ability to maintain stoichiometry between the target and the deposited film, grow metastable material phases, and its high nucleation density per pulse during deposition.

Film growth can be categorized into five major phases: laser absorption, plasma creation, dynamic expansion, condensation, and film growth. The laser incident on a specific material is first absorbed at a depth related to its wavelength dependant absorption depth, heat of

vaporization, beam energy density and laser pulse duration. The excitation of electrons results in a rapid increase in temperature for the absorbing volume, a dissociation of bonds between constituent atoms and subsequent ionization.

The generated plasma rapidly recoils from the material's surface perpendicularly by Coulombic repulsion and thermal expansion. The vapor then travels towards the substrate where it can undergo scattering or diffusion depending on the medium in which it is travelling. Inert gas with pressures on the order of mTorr can be used to modify the energetics of the plume, however, reactive gases can also be introduced to participate chemically with the plasma or film, as is the case with deposited materials such as oxides and nitrides. The high energy plume interacts with the substrate and is quenched, condensing on the surface.

One such condensation mechanism is the interaction of the high energy vapor plume with atoms sputtered from the substrate or deposited film.^[68] As the plasma condenses on the substrate it cools and nucleates in a local minimum position for its chemical environment, according to the mechanisms described in section 1.2. Before thermalizing, the condensate typically has more energy than with other growth techniques, which allows for lower substrate growth temperatures. Additional heating of the substrate and film is often still used to promote nucleation and growth into energy minimized positions that lead to good crystal quality.

The laser used to ablate materials for the CdTe films and heterostructures on sapphire is a Light Machinery IPEX-848 excimer laser using a mixture of krypton and fluorine in a buffer of neon in its laser head. In this configuration, the apparatus produces laser light with a wavelength of 248 nm and pulse duration of 12 ns to 20 ns full width half maximum (FWHM) with a beam size of 12 mm by 26 mm. The energy per pulse can be varied between 100 mJ to 450 mJ per pulse at a set repetition rate, up to a maximum pulse repetition rate of 200 Hz. The internal energy monitor of the laser is calibrated using an external meter, a calibrated ScienTech 365 power and energy meter.

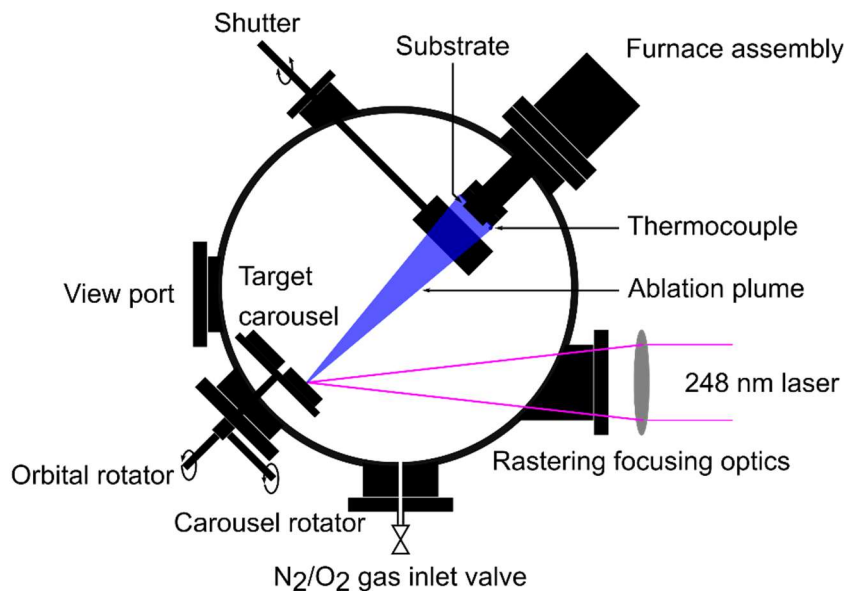


Figure 7: A schematic representation of the PLD growth chamber

A schematic cross section of the PLD growth chamber is shown in Figure 7. Along the optical path, the center of the UV laser beam is first masked using a copper shield to a 15 mm by 6.3 mm rectangle shape.

This masking of the beam edges removes the Gaussian profile of the beam, to create a more flattop profile and uniform energy across the beam image. This shaped beam is focused through the deposition chamber front optic onto a 1-inch target to an image area size of 4.25 mm².

This focused image is raster scanned along the target radius while it rotates by moving the focusing lens horizontally back and forth using a controlled stepper motor. This broadens and creates a more uniform deposition profile, but also more uniformly uses the target material and prevents laser trenching. Three different material sources per growth are made possible by using targets mounted onto an orbital style rotator, such that a carousel of up to three targets can be rotated about a central axis to put a target into the beam path while each target also rotates about its own centre.

A shutter, made of Incoloy sheet, is used to shield the substrate from the deposition plume when necessary. The substrate is mounted using various Incoloy sheet masks to a platinum coated Incoloy heater face. A temperature controller powering a cartridge heater, separated from the growth medium or vacuum, heats the substrate through the Incoloy face to a set-point measured by a Pt-Rh thermocouple mounted near the substrate on the furnace assembly face.

While most depositions occurred in vacuum at the system base pressure, $\sim 2 \times 10^{-7}$ Torr without liquid nitrogen (LN₂) in the cold jacket and

$\sim 8 \times 10^{-8}$ Torr with LN_2 in the cold jacket, the chamber is also designed to operate at a variety of partial pressures as well. A Granville Philips 275 Convector gauge is used to measure pressure in the range of 760 Torr to 1 mTorr and the Varian SenTorr gauge with a hot cathode is used for pressures below 1 mTorr. For growths in a partial pressure gaseous medium, gas is introduced by a Granville-Philips 216 pressure controller, with flow rates monitored by a Sierra Top Trak 821 mass flow meter.

2.2.2 Electron Microscopy

Electrons are an important tool to probe the properties of materials.^[69] Since they are charged particles, they interact strongly with matter. Free electrons can be generated from thermionic or field emission and accelerated to high velocity in vacuum using electric fields, giving them smaller de Broglie wavelengths than most standard X-ray sources. These electrons, since charged, can be focused on or raster scanned across a sample using electric and magnetic fields. Often a beam of monochromatic electrons, electrons with a tight distribution of energy, is used to interact with a specimen in a variety of ways, as shown in Figure 8, to provide both chemical and structural information about a sample.

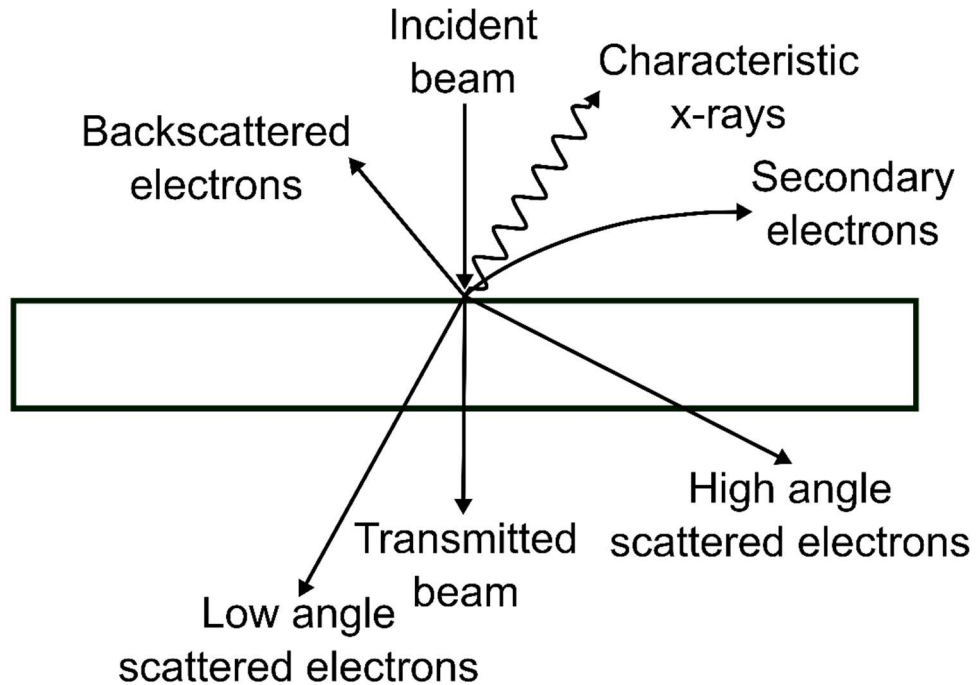


Figure 8: Representation of electron beam interacting with a specimen. The transmitted beam, as well as the low and high angle scattered electrons are used in TEM and STEM analysis. Backscattered and secondary electrons are used for SEM analysis, while characteristic X-rays are used for EDXS.

The predominate types of electron microscopy are scanning electron microscopy (SEM), transmission electron microscopy (TEM), and scanning transmission electron microscopy (STEM). While SEM relies on information generated from interaction at the surface and sub-surface of arbitrarily thick samples, TEM and STEM rely on information generated from the transmission of electrons through relatively thin samples. TEM and STEM were the predominate microscopy tools used in this thesis, to analyse cross sectional samples prepared by focused ion beam (FIB) milling to acquire structural and chemical information.

As seen in Figure 8, there are three major electron beam transmission interactions with the column of atoms in the specimen, which will depend on the incident beam energy and atomic weight of the atoms in the specimen as well as the sample thickness, tilt, density and crystallinity.^[70] For STEM, the scattering profile of transmitted electrons is collected within defined angular ranges on angular detectors, which is converted to an intensity signal corresponding to the scanned probe location.

High angle angular dark field (HAADF) detectors measure electrons scattered at angles 2 to 3 times or greater than the convergence angle of the incident electron beam. The high angle scattering of electrons is very sensitive to the atomic number, approximately $Z^{1.7}$, and provides chemical and structural information, with heavier elements appearing brighter in micrographs. Alternatively, low angle angular dark field (LAADF) detectors measure electrons scattered with angles up to 2-3 times the convergence angle of the incident electron beam and is useful for light element specimens which exhibit weak large angle scattering at high angles.

An electron spectrometer can also be used to measure the energy loss from the incident electron beam, with a narrow and known energy range, undergoing elastic and inelastic scattering at very small angles, near direct transmission. An electron spectrometer uses an energy dispersing magnetic prism to spatially separate electrons of different

energy where they can then be focused and detected on a charge coupled detector. For electrons that scatter forward elastically, there is no loss of energy and thus they contribute to a sharp and intense zero loss peak on the spectrum. They indicate the limit of the experimental energy resolution. As for electrons which scatter forward inelastically, the amount of energy they lose can be interpreted as the type of inelastic interaction which occurred such as plasmon, inter-band, intra-band, and inner shell ionizations. With electron counts plotted as a function of energy, these peaks are characteristic to the elements and chemistry in the probed region of the cross section.

Cross sectional CdTe/sapphire TEM samples were prepared using a NVision 40 SEM equipped with a gallium FIB. Before cutting, lift out and bonding to a grid, the crystallographic directions of the sample were determined by 3DXRD. Before cutting, the region of interest was protected beneath a 100 nm carbon and 3 μm tungsten film. Cross sections were thinned until transparent to a 5 keV electron beam. The thickness was less than 100 nm for the CdTe when later measured by TEM. Before analysis, samples were cleaned using a 30 W plasma mixture of argon, neon, and helium for three minutes.

High resolution STEM imaging and electron energy loss spectroscopy (EELS) of samples was performed using an FEI Titan 80-300 Cubed TEM with a high brightness electron gun and two spherical

aberration correctors in both the probe and the image forming lenses.

STEM images were collected at 200 keV with a dose rate of ~ 100 electrons/ $\text{\AA}^2\cdot\text{s}$ from 50.5 mrad to 200 mrad collection angles, through the 50 μm C2 aperture, at a camera length of 115 mm on a Fischione HAADF detector.

Core-loss EELS maps at the interface were acquired at 200 keV, 37 mm camera length, 100 pA screen current using a Gatan K2 direct electron detector at 0.32 \AA pixel size, 0.0025 s pixel time and 0.5 eV/channel electron dispersion and 4 eV FWHM energy resolution. The low-loss EELS maps at the interface were acquired at 300 keV with a monochromated electron beam of 0.14 eV FWHM energy resolution achieved at 0.05 eV/channel electron dispersion. The low-loss maps were acquired at the same sample camera length and screen current as the core loss maps, but with a 1.6 \AA pixel size, and 0.1 s pixel time using a Gatan US1000FTXP CCD camera.

2.2.3 X-ray Diffraction and Texture Analysis

High energy photons, X-ray and gamma radiation, are also an important probe used to characterize materials, although they have a weaker interaction with matter relative to electrons.^[71] X-rays can be generated from the transitions of electrons between core shell energy levels and Bremsstrahlung radiation. Since X-rays have wavelengths

comparable to the typical atomic spacing in crystals, they can be used to measure crystal structural information. In the reflection geometry, the Bragg geometry, X-rays scatter elastically off the periodic arrangement of atoms to produce a diffraction pattern with maxima and minima, related to the constructive and destructive interference of waves, given by Bragg's law in Equation 2:

$$2d\sin\theta = n\lambda \quad \text{Equation 2}$$

For a monochromatic X-ray beam, with angle of incidence θ and a periodic arrangement of atoms with spacing d , the reflected beam for an integer multiple n of the X-ray wavelength λ is depicted in Figure 9 as a one-dimensional example. A 2θ diffraction experiment, scanning a wide range of incident θ angles and their corresponding reflection angles for positions of maximum and minimum intensity, is most suitable for polycrystalline samples. This is because multiple d -spacings and orientations may exist along the X-ray/detector measurement path, producing a series of lattice parameters from spacings perpendicular to the surface.

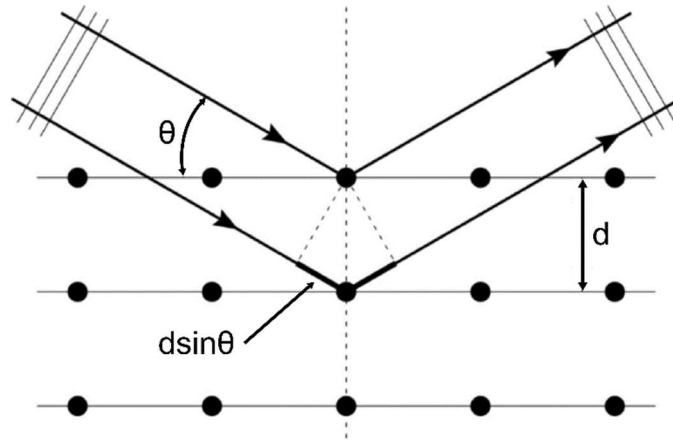


Figure 9: Bragg diffraction condition for a periodic crystal lattice. The spacing of between periodic crystal planes, d , and angle of incident of the X-ray beam, θ , result in constructive interference for a monochromatic X-ray beam of λ .

For samples where the lattice spacing or crystalline orientations vary in directions non-perpendicular to the surface, the relationships between the source and reflected X-rays in all three dimensions provide additional structural information. Three-dimensional diffraction is often discussed in terms of momentum space, the Fourier transform analog of real space, using an Ewald's sphere. For a monochromatic X-ray wavelength, λ , an Ewald's sphere is a geometric construction centred at the origin of reciprocal space whose surface intersections with reciprocal lattice points indicate positions of constructive interference. If no energy is gained or lost (elastic scattering) in the diffraction process, the reflected wave vector, K_r , must be equal to the incident wave vector, K_i , whose magnitude is $2\pi/\lambda$. Thus, the Bragg diffraction condition is satisfied for reciprocal lattice points which intersect an Ewald's sphere construction of radius $2\pi/\lambda$.

Three-dimensional XRD (3DXRD) measurements were made using a Bruker SMART6000 CCD detector on a Bruker 3-circle D8 goniometer with a Rigaku RU200 copper rotating anode X-ray generator while parallel-focusing mirror optics were used for data collection. A single collected CCD frame represents a two-dimensional slice of a hyperbola, a quarter of the sphere, providing diffraction spots or arcs at angular coordinates θ and X . 3DXRD measurements are obtained by capturing and then combining multiple frames while rotating the sample through a third dimension, ω .

Data collected was processed into (111) pole figures for the films, stereographic projections of intensity for the $\{111\}$ spacings present in the sample, using the Bruker GADDS software. A pole figure was also generated for the substrate to determine the orientation of the film relative to the substrate. For a polycrystalline sample with random growth orientation (no epitaxial relationship to the substrate), the experimental pole figures is the convolution of the diffraction intensity information from a number of crystalline sources, producing an image as demonstrated in Figure 10.

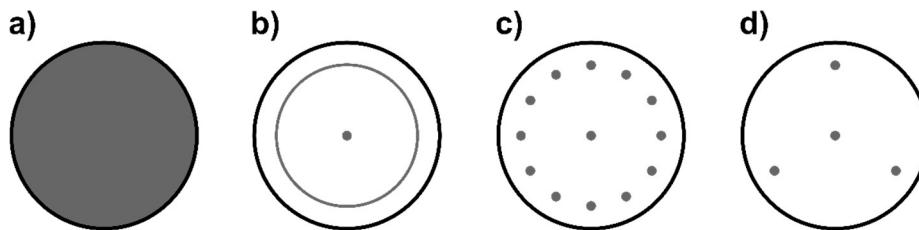


Figure 10: Example (111) pole figures. Pole figures illustrate a (a) polycrystalline randomly oriented sample, (b) (111)-up but in-plane random orientation sample, (c) (111)-up textured epitaxial sample, and (d) (111)-up single crystal face centred cubed crystal sample.

The central peak in a pole figure corresponds to spacings normal to the sample surface, where peaks at the edge of the pole figure correspond to spacings parallel. Thus, broadening in the azimuthal directions indicate that individual crystallites in the sample have in-plane misalignment. As a broad ring transitions to more confined points in a pole figure, it indicates that the number of orientations present in the sample is reduced, the structure is more textured and has preferred crystallographic growth directions relative to the substrate. In a single crystalline sample, the number of diffraction spots reduce to the film crystal symmetry. Broadening of spots in the radial dimension is an indicator of strain present in a crystal and that the unit cell has been distorted.

2.2.4 Substrate Preparation and Growth

CdTe thin films in this section were grown by PLD on 12 mm by 12 mm squares diced from single crystal $\alpha\text{-Al}_2\text{O}_3$ (0001) $\pm 0.5^\circ$ obtained from MTI Corporation. Prior to deposition, the substrates were cleaned with isopropanol, methanol, and acetone. Targets were abrasively smoothed with a fine grit emery paper to remove the influence of macroscopic surface defects from previous laser interaction, such as trenches, before loading. Substrates loaded into the growth chamber were degassed at 450°C for 1 hour before growth, at a base pressure of 3×10^{-7} Torr. CdTe

targets, of purity 99.999%, were ablated with an average fluence of ~ 1.9 J/cm².

Targets were cleaned for 4 minutes at a 2 Hz pulse rate before opening the shutter to remove target surface contaminants. During growth, substrates were held at a nominal temperature of 300°C and target to substrate spacing of 8 cm. The pulse rate during growth was set to 0.5 Hz.

2.3 Results and Discussion

It has been previously demonstrated that single crystal thin films of CdTe (111) can be grown on α -Al₂O₃ (0001) substrates,^[44,72] which by spectroscopic measurement indicate high quality thin film material of comparable or better quality than bulk CdTe.^[73] These films exhibit a single domain of CdTe (111) rotated 60° azimuthally in-plane as seen in XRD ϕ -scans in Figure 11a extracted from 3DXRD measurements. This result, however, is surprising given the azimuthal orientation preferences of CdTe on other oxide substrates.^[44] The geometric surface net of the α -Al₂O₃ (0001) has six-fold symmetry, providing two possible in-plane domain rotations for a three-fold CdTe illustrated in Figure 11b.

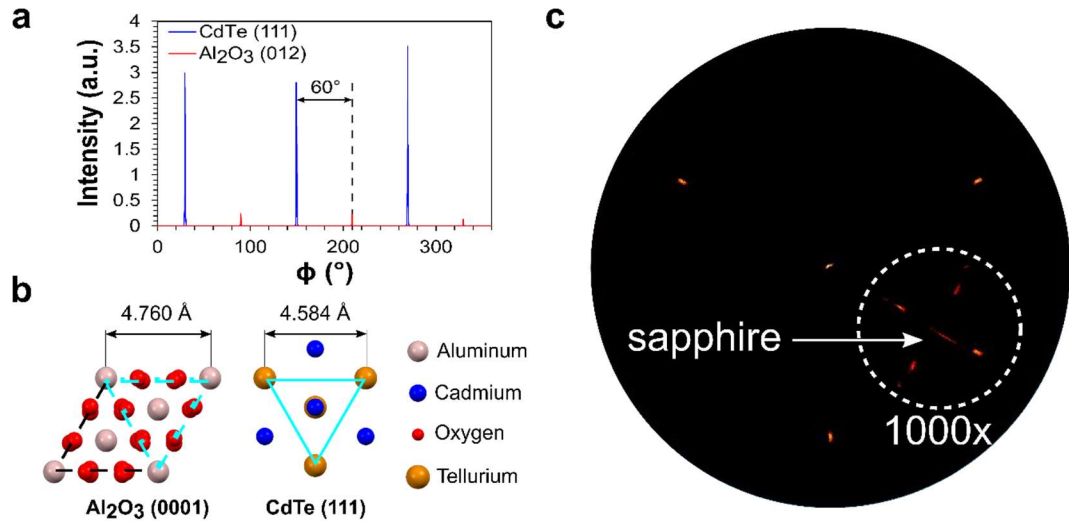


Figure 11: Epitaxial orientation of CdTe on the basal plane of sapphire. (a) XRD ϕ -scans for a set of CdTe (111) and sapphire (012) peaks. A single CdTe domain is azimuthally rotated by 60° from sapphire. (b) Schematic illustration of the in-plane alignment of CdTe (111) on α -Al₂O₃ (0001). The CdTe [110] d-spacing aligns with a 3.697% tensile misfit to twice the α -Al₂O₃ a-plane spacing. (c) (111) count normalized pole figure from the 3DXRD data collected for CdTe on α -Al₂O₃ (0001). The CdTe film grows [111] perpendicular to the c-plane of sapphire. The film has a single domain with a relative micro-twin density of <0.1%.

CdTe is a semiconductor with zinc blende or wurtzite crystal structure with lattice spacings of $a_z=6.483$ Å and $a_w=4.582$ Å $c_w=7.615$ Å, respectively.^[74,75] While the energy of formation between these two structures is small relative to other systems, leading to low stacking fault energies,^[76] bulk CdTe crystals and films tend to grow with a zinc blende structure having the propensity to form its (111) plane parallel to the substrate surface.^[44] As such, the expected lattice mismatch for a domain between an aligned CdTe (110) diagonal and twice the α -Al₂O₃ a-plane spacing, 4.760 Å, is 3.697% with the film in tension.

Despite the geometric equivalence the films grow with a single domain preference and relatively low micro-twin density, seen in Figure

11c. Further these films are strain relaxed and without the density of dislocation networks that would be expected for the mismatch of the system, as seen in Figure 12. Further, the films demonstrate the ability to be facily transferred from their growth substrate, discussed in more detail in Chapter 3, to another carrier while preserving their structural and optical quality.

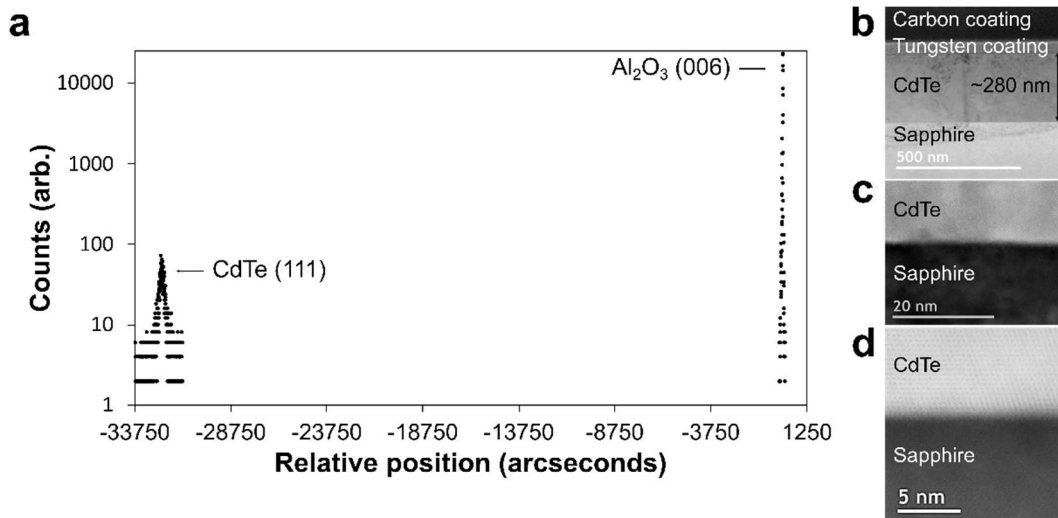


Figure 12: Strain relaxed, high quality CdTe heteroepitaxy on Al₂O₃. (a) High resolution XRD measurement for residual strain in a CdTe film. The position of the CdTe (111) film peak relative to the Al₂O₃ (006) substrate peak provides an accurate measure of the out-of-plane lattice space of the CdTe film. Compared to the bulk lattice spacing for CdTe, the CdTe film is mostly relaxed with a residual compressive strain of 0.097% out-of-plane. Micrographs of CdTe/Al₂O₃ provide a complementary dataset at low (a), medium (b) and high (c) magnifications demonstrating a lack of strain induced defects extending from the interface as would be expected from the system misfit strain.

Utilizing STEM and EELS analysis, the polarity of the CdTe (111) films were consistent with a CdTe (111)A polarity, as demonstrated in Figure 13. This implies a tellurium terminated surface at the sapphire interface and cadmium terminated surface in the growth direction. The termination of the sapphire surface was investigated by EELS of the

aluminum-K (A K) and oxygen-K (O K) edges to produce area and line scans. These were used to determine atomic composition maps of the sapphire surface at the film/substrate interface, seen in Figure 13, which was consistent with a single aluminum layer termination, the most stable and non-polar reconstruction of $\alpha\text{-Al}_2\text{O}_3$ (0001).

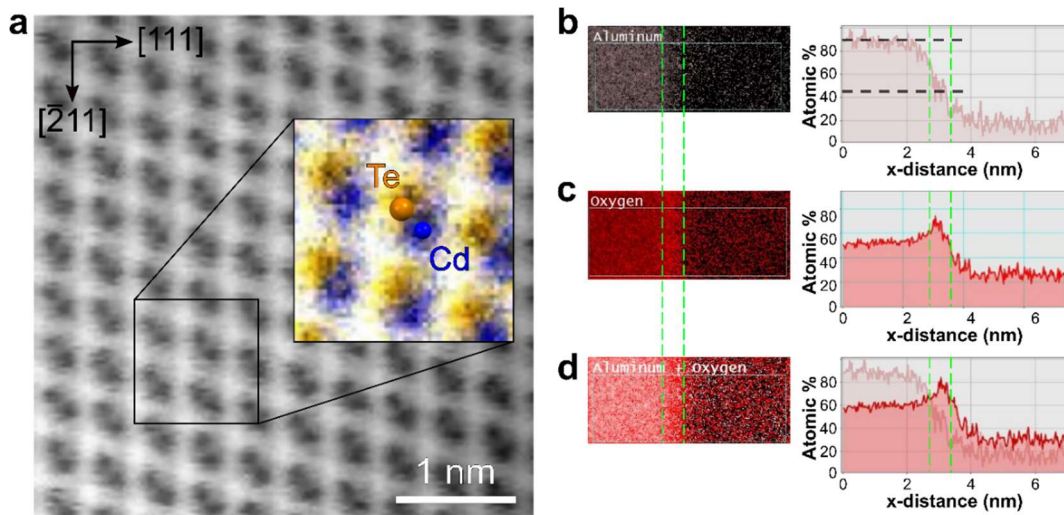


Figure 13: CdTe film polarity and sapphire surface termination. (a) Annular dark-field STEM micrograph of CdTe with magnified atomic resolution inset providing EELS colour composite image indicate films are CdTe (111)A. This implies a Cd-terminated surface in the growth direction and a Te-initiated surface at the interface with sapphire. (b) Chemical profile for aluminum using the Al K edges and corresponding atomic composition map across the substrate film/interface. The region of the last atomic layer of sapphire is indicated by the green dashed region. (c) Chemical profile for oxygen using the O K edges and corresponding atomic composition map across the substrate film/interface. (d) Composite aluminum and oxygen chemical profile map and atomic composition map at the termination of sapphire. Atomic percentage of aluminum at the termination of sapphire is half of the bulk value, consistent with a single aluminum termination.

It has been previously postulated that small local differences in the chemical environment from surface-exposed aluminum atoms could act as adsorption sites for adatoms,^[77] which drive the nucleation of a single domain for CdTe (111) during growth.^[53] Density functional theory (DFT)

modeling of adatoms on the single aluminum terminated surface of Al_2O_3 (0001) indicates a chemical binding energy preference for tellurium compared to cadmium,^[53] in particular for the tellurium to bind above oxygen sites in a continuation of the sapphire crystal structure substituting for the next aluminum layer.

Given the two-order magnitude difference in the vapour pressures of tellurium and cadmium, 269 μTorr and 50.4 mTorr , respectively,^[78,79] at a nominal substrate temperature of 300° during deposition, it is also rational to assume it is more kinetically favourable for tellurium to nucleate rather than desorb compared to cadmium during growth. The slight increase in EELS intensity for the composite aluminum and oxygen chemical profile maps of the last sapphire oxygen layer was investigated further by comparing the integral normalized oxygen-K edge signal, after background subtraction, for the bulk and surface oxygen signals.

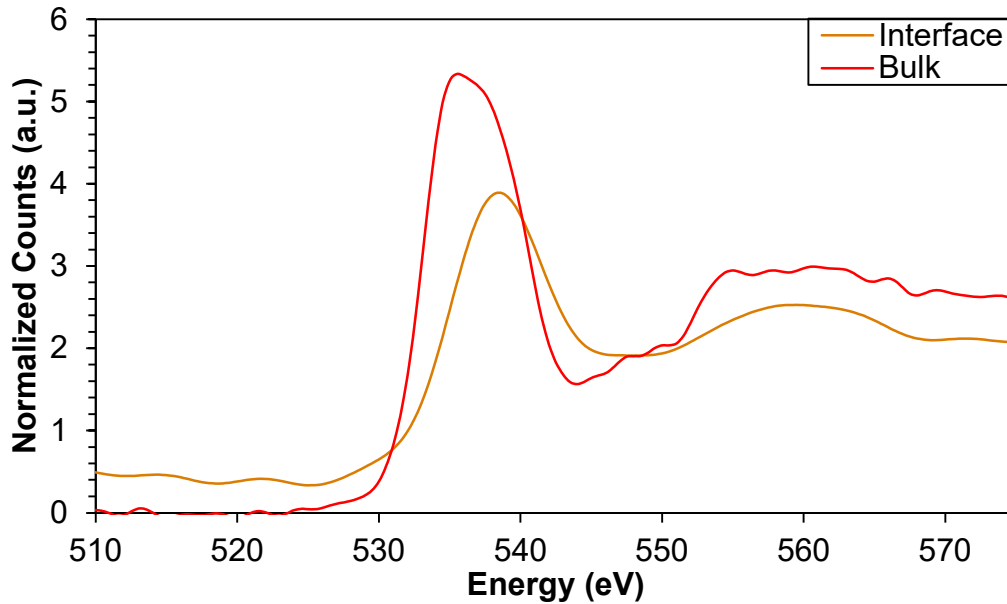


Figure 14: EELS O K edge comparison for bulk and surface of sapphire. The atomic oxygen-K and tellurium- $M_{4,5}$ edges occur at 532 eV and 572 eV, respectively. Comparison of the normalized line shapes of the interface and bulk O K edge reveal a ~ 2 eV shift right in energy at the interface. Further, the sharp step like increase in the region after the O K peak in the bulk towards the Te $M_{4,5}$ peak, is replaced by a rounded transition. These line shape feature transitions are consistent with a change in chemical bonding for the oxygen atoms on the surface of sapphire compared to the bulk. Each curve is normalized by its integral, after performing a background subtraction. Curves are also smoothed by filtering with a low-pass filter after determining the signal and noise contributions from a power spectral density analysis.

Referring to Figure 14, the atomic O K and tellurium- $M_{4,5}$ (Te $M_{4,5}$) edges are expected to occur at 532 eV and 572 eV, respectively. Comparatively, the Al K edge occurs at 1560 eV, well away from these two edges of interest given the instrument resolution. The normalized O K edge line shapes demonstrates a ~ 2 eV increase, toward the Te $M_{4,5}$ edge, for the interface oxygens relative to the bulk oxygens. Further, in the energy regions between O K and Te $M_{4,5}$ peaks the bulk oxygen response exhibits a sharp step like increase while the interface oxygen's response is

a rounded transition. The line shape energy shift and transition shape are consistent with changes to the chemical bonding for the oxygen atoms on the surface of sapphire compared to the bulk. Since bonding represents a mechanism to minimize the system energy for stability, these observations support earlier DFT predictions that surface oxygen sites act as nucleation centres for adatoms for film growth.^[53]

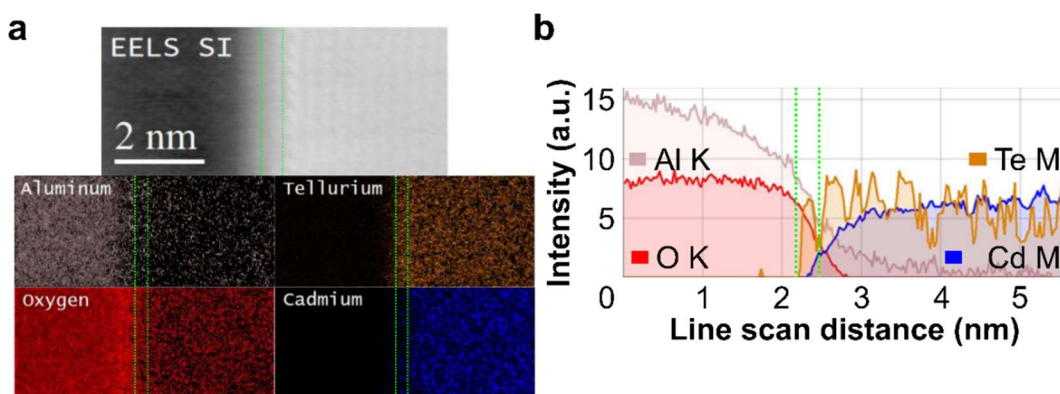


Figure 15: EELS area and line scans of CdTe/Al₂O₃ interface. (a) EELS SI map with corresponding false coloured EELS area maps of CdTe and sapphire regions. The hashed green line section indicates a missing layer of Cd and the presence of Te across the surface of the substrate at the interface with the film. (b) EELS line scan, across the Al₂O₃-CdTe interface, using the K edges for Al and O as well as the M edges for Cd and Te to map the chemical composition, indicates the presence of a tellurium monolayer. This region is outlined with hashed green lines.

Additional chemical analysis of the cross-sectional interface between the CdTe film and the α -Al₂O₃ substrate by EELS, introducing the Te M_{4,5} and cadmium-M_{4,5} (Cd M_{4,5}), which occurs at 404 eV, reveals the presence of an unexpected tellurium monolayer decorating the surface of the sapphire substrate at the interface with the film. This tellurium monolayer can be identified in the EELS area maps and line scans of the interface as shown in Figure 15. This additional tellurium monolayer

decoration occurs before an abrupt interface with a CdTe (111) tellurium terminated surface, as predicted from the determined polarity of the film.

Taking successive STEM-HAADF micrographs of the same interfacial region after defocusing by 50 nm reveal additional CdTe layers and the tellurium monolayer at the interface not seen when the film and substrate are in focus. This observation is consistent with necking at the film-substrate interface, as shown in Figure 16. This phenomenon, having a thinner 'neck' region at the film and the substrate interface, would be expected during the FIB lift-out preparation of a sample with an interfacial rate of milling faster than the substrate or film, such as for a weakly bound interface compared to bonding in the substrate or film. As is mentioned previously, the CdTe (111) films demonstrate the ability to be layer transferred from the growth substrate, while the α -Al₂O₃ (0001) substrates, post film transfer, have been shown to support multiple film regrowths without significant film quality degradation. This ability and the observed preferential etching of the interface during lift-out preparation, seen in Figure 16, are both consistent with weak bonding at the film-substrate interface.

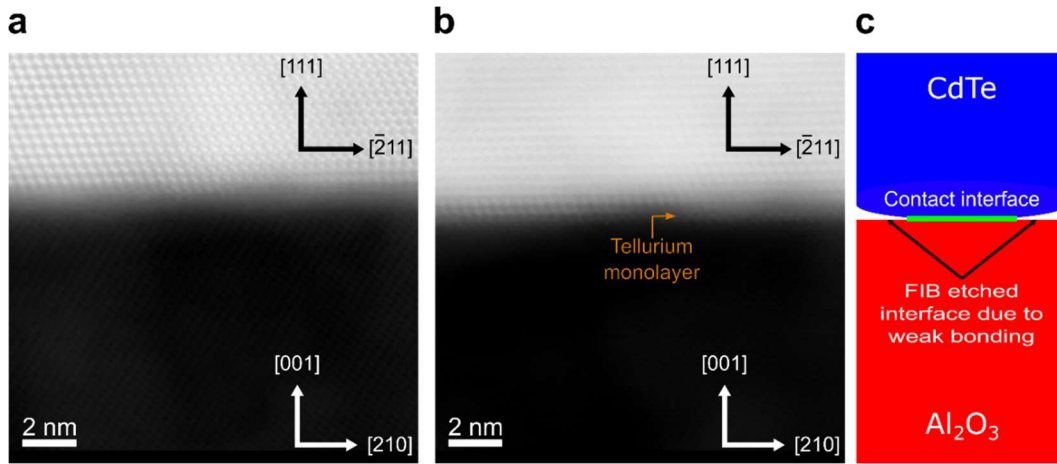


Figure 16: Milling induced necking at the film-substrate interface. (a) HAADF-STEM image at current focus shows unclear CdTe-Al₂O₃ interface, however, has visible film and substrate lattices. (b) Repeated HAADF-STEM of same sample site with beam defocused 50 nm, reveals additional CdTe layer toward the interface not seen when the film and substrate lattice was in focus. This is consistent with necking at the film-substrate interface. (c) An illustration of milling induced necking at the CdTe-Al₂O₃ interface for the FIB prepared sample. A faster rate of milling would be expected at a weakly bound interface and is consistent with the ease of film layer transfer from the substrate.

Probing the interface of the CdTe film and the α -Al₂O₃ directly by STEM, see Figure 17, reveals the CdTe (111) film epitaxially aligned in- and out-of-plane, as indicated in the XRD analysis, but incommensurate to the sapphire substrate spacing. Extended dislocation networks, as would be expected from the 3.7% lattice mismatch of the film-substrate system, are not observed. Rather, epitaxial strain predominately relaxes spontaneously across the film-substrate interface, due to the apparent weak bonding. The observed tellurium monolayer, see the Z-contrast in the HAADF micrograph of Figure 17a, terminates the sapphire surface as expected from the EELS line and area scans of the interface. The spacing between the layer of tellurium atoms decorating the surface of sapphire

and in the first layer of tellurium of the CdTe crystal, Figure 17b, is found to be 3.171 Å, while the regular spacing of tellurium atoms in CdTe in the [111] is 3.743 Å. A simulated epitaxial system overlay is provided in Figure 17c, providing an atomic model of the interface which is consistent with the observed Z contrast, atomic spacing and EELS data.

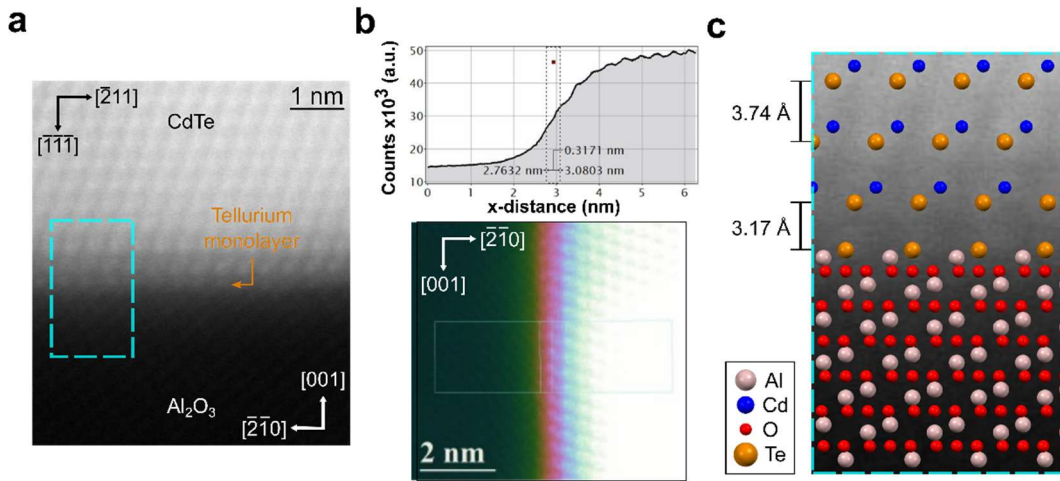


Figure 17: STEM micrograph and atomic model of CdTe-Al₂O₃ interface. (a) HAADF micrograph of the CdTe-Al₂O₃ interface, indicating the presence of a tellurium monolayer at the interface of the sapphire substrate. (b) A colour adjusted HAADF image is used to measure the interlayer spacing between the Te monolayer and first CdTe layer. The interlayer spacing estimates the distance between the tellurium atoms in the monolayer and first layer of CdTe to be 3.171 Å. The regular spacing of tellurium atoms in the CdTe [111] is 3.743 Å. (c) Magnified region of micrograph, as indicated by the blue hashed box in (a), with simulated ball atom epitaxial system overlaid at the observed spacing and positions.

This relatively large spacing between the tellurium surface decoration and abrupt tellurium termination of the CdTe film at the interface is consistent with Te-Te vdW bonding. This phenomenon and tellurium surface decoration of sapphire is similar to observations of the spontaneous Te-termination of α -Al₂O₃ (0001) substrates following the

deposition of the vdW layered 2D material Bi_2Te_3 by PLD.^[33] However, unlike the 2D on 3D vdW epitaxial system, CdTe (111)/ Al_2O_3 (0001) is a material system exhibiting 3D on 3D vdW-like bonding at the interface, with implications for widespread application.

As indicated in sub-section 2.2.4, prior to deposition the sapphire substrates are only solvent cleaned and then degassed for 1 hour under vacuum at a temperature of 450°C before growth. While the non-polar single aluminum terminated reconstruction of c-plane sapphire during this growth is expected to be stable and lacking dangling bonds, as inferred from surface studies and modeling of the (0001) surface by Chang and Godin et al,^[57,58] the surface has demonstrated and has expected weak chemical interactions with adatoms.^[51,77,80]

Te adatoms have been observed here and during the deposition of Bi_2Te_3 , by Hwang et al.,^[33] to bind to the vacant aluminum site suggesting the film-substrate system energy is minimized by the creation of this pseudomorphic surface decoration during growth. The expected equilibrium condition for this system, tellurium, and cadmium adatoms on a sapphire c-plane surface at 300°C , is for the adatoms to desorb and leave the surface bare. Thus, it is postulated that the spontaneous formation of a tellurium pseudomorphic layer at the interface occurs dynamically, influenced both by energy minimization and growth kinetics.

Deposition of films on a pure vdW surface, such as CdTe on graphene,^[81] generally leads to large azimuthal orientation dispersions. However, for systems where weak chemical interaction and vdW forces contribute to the interfacial energy, such as CdTe on Mica,^[82] decreased in-plane orientation dispersion has been observed leading to higher epitaxial quality. Similarly, it is postulated that for this system, CdTe on sapphire, weak chemical interaction drives the dynamic formation of a Te surface decoration during deposition to minimize energy, which constrains the in-plane orientation for the CdTe epilayer to a single domain.

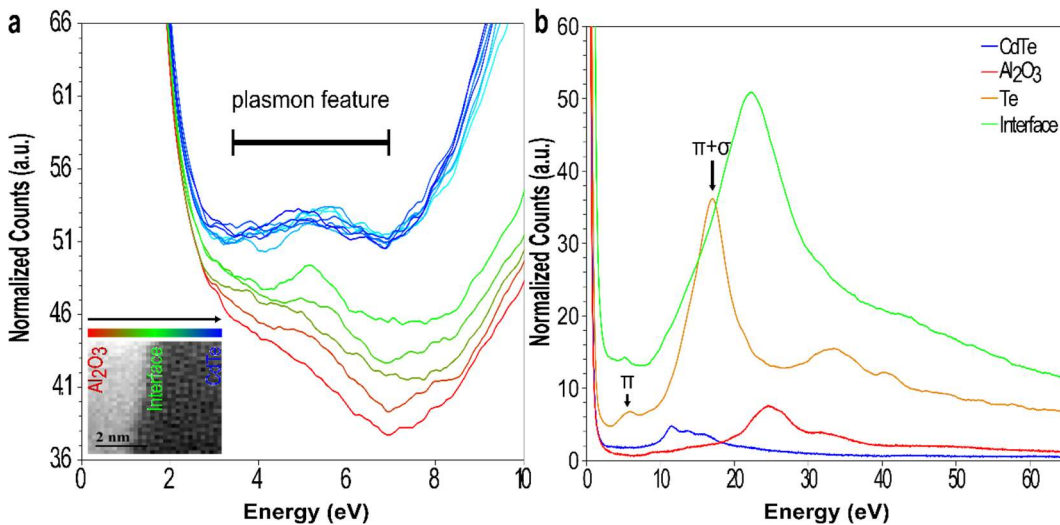


Figure 18: Low-loss EELS plasmon feature unique to the interface. (a) EELS spectrum image inset, was acquired by a monochromated beam at the interface with a colour bar and arrow to indicate the scan transition from the substrate to the film where spectra were collected. As the spectra evolve from red (Al_2O_3), to green (the interface), and then blue (CdTe) a unique plasmon feature at the interface with peak intensity at ~ 5.6 eV appears. Spectra are normalized to have equivalent zero loss peak integrals. (b) Surface and bulk plasmon spectra for the interface, CdTe, Al_2O_3 , and pure tellurium signals, are compared using the same normalization. The reference low-loss EELS for CdTe and Al_2O_3 are collected from regions ~ 100 nm away from the interface while the tellurium spectrum is collected from a separate pure tellurium sample using the same experimental microscopy conditions and similar FIB preparation. The plasmon feature at the interface is not seen in the film or substrate but corresponds to the π plasmon seen in pure tellurium.

Referring to the obtained low-loss region EELS spectra for the CdTe-sapphire system, as shown in Figure 18, a plasmon feature at ~ 5.6 eV is uniquely observed at the interface. Comparing the interfacial EELS spectrum to that of CdTe and sapphire measured ~ 100 nm away from the interface as well as a bulk tellurium spectrum, reveals that the low energy feature is aligned with a low energy plasmon peak observed in pure tellurium. Pure bulk tellurium consists of strongly covalently bonded helical chains with interchain vdW interactions.^[83] As such, for bulk tellurium a low energy plasmon feature, corresponding to the energy region of interest at about 5.6 eV is attributed to the π -plasmon from weak interchain bonds. It is also observed in the low-loss EELS maps between layers of chalcogen and non-chalcogen containing 2D van der Waals materials and is assigned to the π -plasmon peak.^[84,85]

Combined with the measured Te-Te interlayer spacing at the interface and the ease of film transfer, the low-loss region EELS peak for the interface of the CdTe-sapphire system is attributed the observed weak bonding. A localized detection of plasmon peaks at the interface is expected for van der Waals like bonding and is indicative of the anisotropic conductivity of electrons traveling along π -bonds at the interface. The weak chemical interaction driving the spontaneous Te-termination of α -Al₂O₃, as well as the unique vdW interaction between the epilayer and substrate surface decoration, allows for strain to

spontaneously relax at the interface. As such, high quality CdTe epitaxial films on sapphire are possible due to a compliant interface, similar to other epitaxial systems where the strain is accommodated by engineered interface layers.^[28,86]

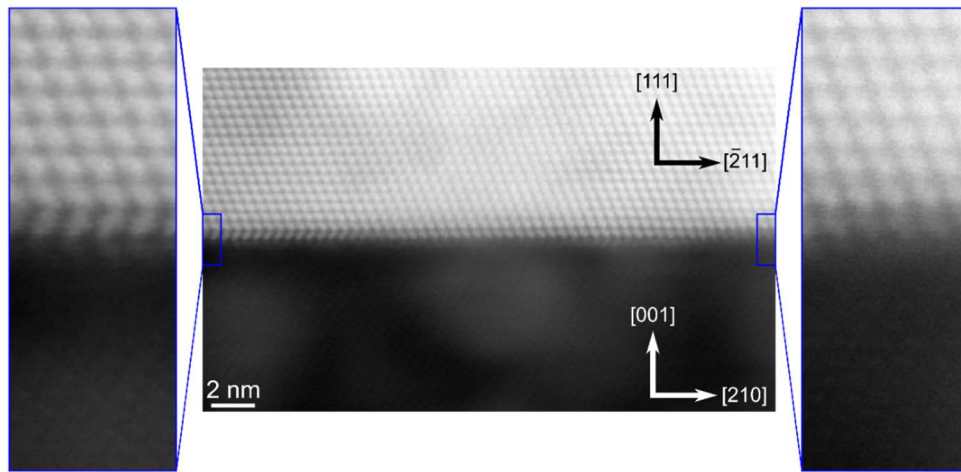


Figure 19: Overgrown stacking fault at CdTe- Al_2O_3 interface. (Right) HAADF-STEM image demonstrates one compliant strain relief mechanism for the $\text{Al}_2\text{O}_3/\text{CdTe}$ system occurring spontaneously and abruptly at the van der Waals-like interface. (Centre) A local variation in the sapphire topology, is observed to introduce a laminar stacking fault layer at the interface which is overgrown moving away from the interface. While the first CdTe layer is seen to be incommensurate to Te-terminated sapphire surface, as the vertical alignment of Te atoms across the interface shifts from right-sidedness to left-sidedness, a laminar stacking fault at the intersection of two relaxed regions can occur. (Left) This type of stacking fault is overgrown by subsequently deposited layers and localized to the interface.

The predominate mechanism for misfit strain relaxation of the compliant interface of the CdTe- Al_2O_3 system appears to be weak vdW-like bonding for large flat areas of the sapphire surface. For local variations in the topology of the sapphire surface such as steps between terraces, as shown in Figure 19, a laminar stacking fault is observed at the interface which is overgrown in the CdTe moving away from the interface.

In the HAADF-STEM micrograph in Figure 19, sections of the first CdTe layer appear to be commensurate to the pseudomorphic Te surface layer of sapphire.

As the spacing increases across the horizontal the CdTe becomes incommensurate, with the vertical alignment of Te atoms between the sapphire surface and first layer of the film shifting from a bond with right-sidedness to left-sidedness. A lamellar stacking fault can occur at the intersection of these two relaxed regions. This lamellar stacking fault which is overgrown is essentially a dislocation loop trapped at the interface which relieves strain to make the substrate compliant, occurring instead of the normal threading dislocations which would extend for a mismatched epitaxial system interface into the film.

Recall that the non-centrosymmetric symmetry of the sphalerite structure gives rise to crystallographic polarity for CdTe. However, the growth of a polar film, CdTe (111), on a non-polar substrate, Al₂O₃ (0001), does not produce the expected antiphase boundaries observed in other polar on non-polar systems.^[60] Since the CdTe [111] contains alternating planes of cadmium and tellurium atoms, each layer in that direction has a +Q and -Q charge, respectively, due to the ionicity of the CdTe bond. Both the growth surface and interfacial surface must resolve the accumulation of a large electric field across the film, in the out-of-plane direction, by a surface electronic rearrangement. It is postulated that the observed Te

pseudomorphic interfacial layer and vdW-like bond to Te in the first CdTe layer both constrains the azimuthal orientation and resolves the polarization of the CdTe film.

Recall remote epitaxy through graphene sheets and other 2D interlayers is governed by polarity dependant atomic interactions over short distances.^[36] In polar on non-polar systems such as GaAs (111)/graphene/Si (111), the lack of Coulombic interactions penetrating the graphene from Si surface atoms to gallium and arsenic adatoms lead to island growth and fibre texture, and no in-plane orientation preference.^[87] In addition, in the GaAs/graphene/GaAs system, remote epitaxy demonstrates single crystalline growth for a single graphene layer, but a loss of in-plane orientation preference and island growth for bilayers and tri-layers of graphene. This occurs as the spacing of the substrate and film increases beyond an interaction gap of $\sim 5 \text{ \AA}$.

Given the observed 3.171 \AA separation between the Te surface decoration and tellurium atoms in the first CdTe layer, growth of a CdTe film on a thicker tellurium layer deposited on sapphire was proposed to verify that the unique behaviour and single crystal nature of the CdTe film was due to the Te-terminated surface of sapphire and not a property of CdTe films deposited on tellurium surfaces in general.

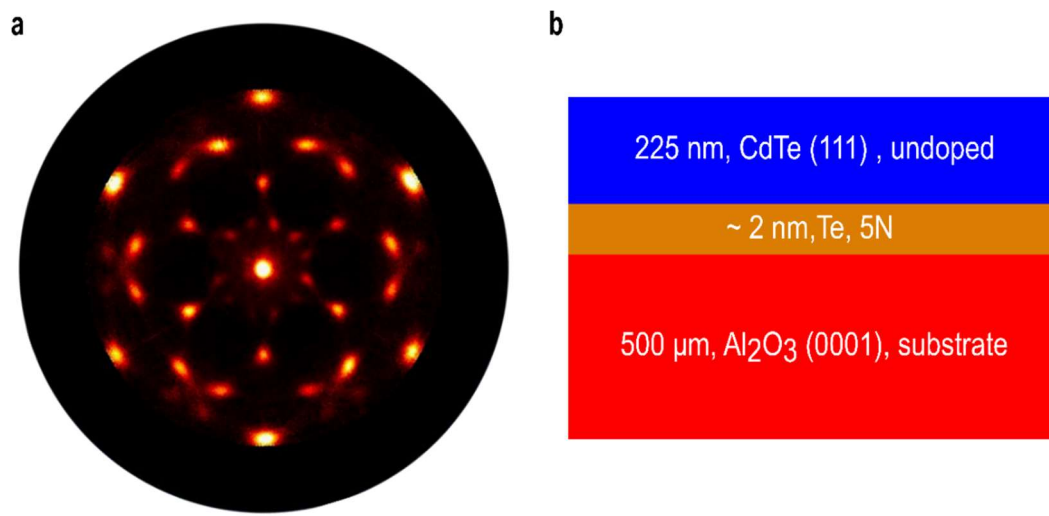


Figure 20: Domain preference for CdTe/Al₂O₃ with additional Te interlayers. (a) (111) pole figure from the 3DXRD data collected for CdTe grown on α -Al₂O₃ (0001) with an additional tellurium interlayer. Pole figure indicates loss of single domain preference to a 70:30 ratio of the regular domain to another in-plane domain rotated by 60°. Sample also exhibits pronounced secondary twinning. Further, the position of the 2 θ (111) and breadth of the peak in the XRD single frames is shifted indicating the films are ~1.36% compressed out-of-plane, where CdTe films directly on sapphire exhibit almost no strain. (b) Schematic representation of CdTe film grown on sample with additional intentional Te interlayer having a thickness of ~2 nm. Degenerated epitaxial alignment of film with intentional tellurium interlayer, well beyond one pseudomorphic monolayer, is consistent with remote epitaxial interactions extending only a short range from the Te reconstructed substrate surface.

As seen in Figure 20, the addition of a ~2 nm Te interlayer on the surface of sapphire before the deposition of CdTe leads to a highly twinned film texture and loss of single domain preference. A position shift and increase in FWHM for the CdTe 2 θ (111) peak indicates these films are also strained by 1.36%, compressed out-of-plane, while CdTe films grown directly on sapphire are mostly relaxed, as shown in Figure 12. This degenerated epitaxial alignment for films grown with an intentionally thick tellurium interlayer, increased interaction gap, is consistent with remote epitaxial interactions extending only a short range from the Te-

reconstructed surface of sapphire through the vdW-like bonds to the first layer of CdTe.

2.4 Conclusions

The direct growth of a 3D heteroepitaxial system on a 3D substrate, CdTe (111)/Al₂O₃ (0001) by the formation of a spontaneous vdW-like bond at the interface, instead of the two 3D crystals being strongly bound, has been demonstrated. Despite the large lattice mismatch, polar on non-polar epitaxy and the system having a cubic on hexagonal symmetries, the thin films are single crystalline maintaining a high quality due to the strain compliance of the interface. The weak bonding of the interface is accomplished by the self-assembly of a pseudomorphic chalcogenide layer, tellurium, on the surface on sapphire during growth.

The demonstrated ease of thin film transfer, preferential etching of the interface during lift-out preparation and lack of residual strain in the film are all consistent with weak bonding at the interface. EELS chemical analysis, the observed Z-contrast in HAADF micrographs and the atomic spacing at the interface all support that the source of this weak bonding is a van der Waals like bond between the tellurium atoms decorating the surface and sapphire and those tellurium atoms in the first layer of the CdTe crystal. Further, an analysis of the low-loss region of the EELS

spectra for the interface reveals the presence of a π -plasmon peak consistent with vdW-like bonding.

Like engineered compliant interfaces in literature, the misfit strain is accommodated at the interface and constrained to the interface. Changes in sapphire surface topology, however, are accompanied with a stacking fault at the interface that are overgrown. Evidence also suggests that tellurium decoration of sapphire interacts with the first CdTe layer at a short distance to constrain the in-plane orientation and polarity of the film, instead of this interface being a feature of CdTe growth on tellurium.

The formation of this interface happens spontaneously in-situ during growth, without the need for wet chemical processing or 2D layer transfer. As such, it has the potential to integrate well into standard semiconductor epitaxial processes for large wafer sizes, acting as a mechanism to template novel materials or produce freestanding thin film devices which can be processed on both sides. Chapter 3 will discuss the methodologies employed to utilize the ability of the films to be transferred from their growth substrate, while Chapter 5 will explore some proof-of-concept heterostructure devices fabricated from these thin films transferred to flexible polymer substrates.

3 Transfer Methods for Epitaxial Thin Films

3.1 Relevant Literature and Previous Work

High quality semiconductor materials processed into bulk wafers by melt growth, such as the Czochralski, zone melting and traveling heater methods,^[88] remain a key component of electronic and opto-electronic devices. However, only a small subset of material systems offers wafer diameters and costs which allow for large scale device fabrication. The infrastructure to achieve economies of scale for most binary and ternary semiconductors do not exist, and is further hindered by technical limitations in producing large diameter wafers for some materials due to their thermal and mechanical material properties.^[1,2] Further, kerf-loss from the dicing of bulk crystals into wafers, even for materials which are readily mass produced,^[89,90] presents challenges of reduced wafer yield and material waste, which worsen as wafers become thinner.

Thin film growth presents an alternative production route for those materials without readily available and inexpensive wafers, and it overcomes the issues of kerf-loss for thin devices. As previously mentioned, high quality epitaxial films are normally grown on lattice-matched single crystal wafer substrates which act as growth templates and the subsequent carriers for the films. Where these substrates exist, they often comprise a significant fraction of the total device cost and

possess properties which are non-ideal or detrimental to the performance of the device.

As such, there has been an effort to produce thin wafers, less than 50 μm in thickness and freestanding films. These offer several advantages, in addition to reduced material costs, as demonstrated in devices such as flexible electronics and for light management in photovoltaic devices.^[4,5] Current state-of-the-art kerf-less fabrication processes focus on the removal of thin layers from bulk substrates by selective wet chemical etching,^[91–94] controlled spalling,^[95] Smart Cut™,^[96,97] and by the layer transfer of films grown by van der Waals or remote epitaxy.^[35,98,99] However, common drawbacks of these techniques include the requirement for substrate post-processing for subsequent regrowths and the limitation to materials with large wafer diameters which are already commercially available.

The discovery of the spontaneous relaxation of heteroepitaxial thin films by vdW-like bonding on chalcogen monolayer-terminated sapphire substrates represents a novel mechanism to produce high quality single crystal films which can be layer transferred from their growth substrate, leaving the substrate for future reuse. This method is advantageous as it integrates well into standard semiconductor manufacturing processes, with minimal pre- and post-processing of the growth substrate such as chemical etching, ion implantation, or post growth surface recovery

polishing. However, like the other techniques mentioned, it still requires the careful control and handling of transferred layers to produce free-standing or hybrid bonded devices.

Thin film layer transfer technology relies on the use of a handle layer which imparts a strain on the thin film to initiate either edge delamination or spalling from the substrate and prevent wrinkling or cracking as a support carrier during transfer. This includes wet thin film transfer methods, which utilize surface wettability and liquid surface tension to decohere films from their substrate and then support films taut while floating on the liquid surface.^[100,101] In essence, thin film transfer techniques are methods to control the direction of separation, like cleavage of bulk crystal, and therefore dependent on the fracture mechanics of the system under study.

As mentioned in section 1.2.2, strain in the film/substrate system which cannot be accommodated elastically is released by the formation of crystallographic defects and by fracture, if the stress intensity factor exceeds the fracture toughness of the film or substrate. For a bi-material system, the Dundurs' parameters are given by Equations 3 and 4:^[18]

$$\alpha = \frac{\Gamma(\kappa_2 + 1) - (\kappa_1 + 1)}{\Gamma(\kappa_2 + 1) + (\kappa_1 + 1)} \quad \text{Equation 3}$$

$$\beta = \frac{\Gamma(\kappa_2 - 1) - (\kappa_1 - 1)}{\Gamma(\kappa_2 + 1) + (\kappa_1 + 1)} \quad \text{Equation 4}$$

The Dundurs' parameters, α and β , are dimensionless parameters used to measure the elastic dissimilarity of a two-material system. The subscripts 1 and 2 denote the deposited layer and the substrate materials, respectively, as denoted in Figure 21. For plane strain, $\kappa=3-4\nu$, where ν is the material's Poisson's ratio, while Γ is the ratio of the shear modulus for the two materials, μ_1/μ_2 .

The first parameter, α , can be interpreted as a measure of the dissimilarity in stiffness for the two materials. If $\alpha>0$, then the layer is stiffer than the substrate, while if $\alpha<0$ the substrate is stiffer than the layer. As such, it is an indicator of which material will be compliant and which material will be stiff during a fracture. The parameter β describes the oscillatory behaviour of the crack tip as it propagates. For crack propagation occurring in a homogenous material or along a plane of relative weakness it is often assumed to be zero. However, it can describe the oscillatory behavior seen in inhomogeneous systems for which fracture occurs, e.g. when a crack does not run parallel with cleavage planes.

Cracking and decohesion processes have been studied for a variety of bi-material systems with their fracture paths found to have a dependence on the relative fracture resistance of the film, substrate and interface, as well as whether the strain is tensile or compressive.^[102] For films in compression on a substrate, the predominate failure modes are buckling and delamination,^[103] and splitting of the film and substrates in a

direction perpendicular to the interface.^[104] However, for films in tension on a substrate, such as the predicted tensile strain in the CdTe (111)/Al₂O₃ (0001) system based upon the lattice mismatch, fracture or decohesion can initiate at the edge of the sample and proceed parallel to the interface.^[19] This fracture can propagate parallel to the interface in the film, at the interface causing film-substrate decohesion, or down into the substrate and then parallel to the interface, spalling, depending on the relative film and substrate fracture toughness to minimize the strain energy in the system.

Such a system where the deposited layer is in tension on a substrate causing spalling is illustrated in Figure 21. Assuming both the thin film and substrate are isotropic and linearly elastic, a crack travels parallel to the interface based upon the longitudinal load and moment, P and M , respectively. Depending on the substrate thickness, $\lambda_0 h$, and film layer thickness, h , and elastic properties of the two materials, the fracture will continue to travel parallel to the film/substrate interface at a depth, λh , depending on the position of the neutral axis.

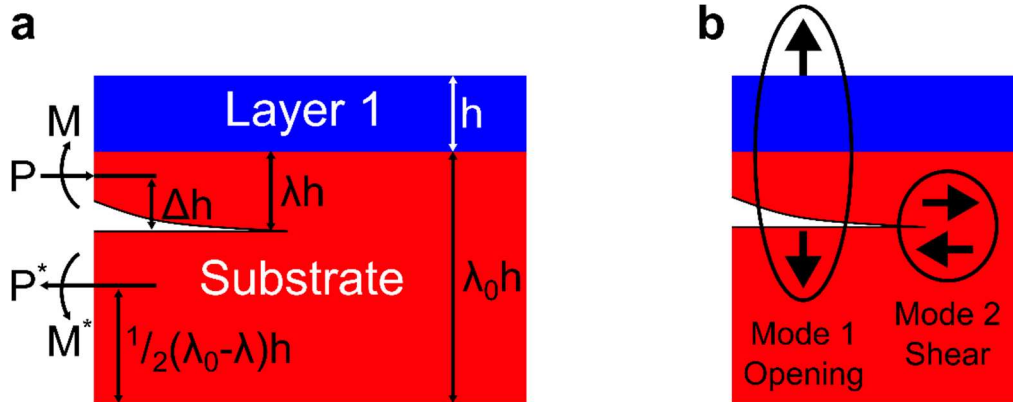


Figure 21: Conventions and geometries for the cracking of brittle substrates. (a) Crack system diagram for a uniform tensile layer on a substrate. The tensile misfit stress of the layer translates to compressive stress in the substrate, causing longitudinal loads and moments in the substrate as it spalls. This diagram ignores the initiation stage of spalling at the edge, and illustrates that the crack tends to run parallel to the interface at a characteristic depth. (b) A simplified illustration of spalling fracture of a substrate due to the presence of a layer 1 material in tension. The resultant longitudinal loads and moments from the tensile strain cause the propagating crack tip to experience opening mode stress and shear mode stress as the spalled surface layers contract.

The neutral axis is the line or plane where the system is neither in tension nor compression. In this example system, this condition occurs at the plane where the longitudinal load and moment at a distance Δh above the plane are balanced with an equal and opposite longitudinal load and moment, P^* and M^* , a distance $0.5 \cdot (\lambda_0 - \lambda)h$ below that plane,^[18] shown in Figure 21a. This analysis is based upon the principle that shear stresses will deflect the crack tip on a path where the energy release rate, G , for the bi-material system is maximized and the shear stress is minimized.^[102,105] The stress intensity factors of a crack tip, shown in Figure 21b, for opening mode, K_I , and in-plane shear mode, K_{II} , are linearly dependent on P and M , and complexly dependent on the relative properties and thicknesses of the material system.

While this thesis does not rigorously study the fracture mechanics of the CdTe/Al₂O₃ system, there are three important general principles from the discussion above of steady-state interface decohesion and substrate spalling which are considered in the development and discussion of the mechanical layer transfer technology of CdTe films and II-VI heterostructures from sapphire in this chapter and published in *Materials Research Express*.^[62] Firstly, for fracture to occur parallel to the interface, the strain must be uniform and biaxial. Defects in the uniformity of the applied strain from a handle layer for film transfer will result in a deflection of the crack tip and prevent large uniform areas from being transferred. Secondly, the strain applied from additional handling layers and applied peel forces should keep the CdTe film in tension, to promote edge delamination at the film edge and prevent film buckling.

Lastly, since fracture trajectory is assumed to follow a path which minimizes the in-plane shear, the crack tip will follow a path parallel to the interface where both K_{II} is approximately zero and K_I , the opening mode stress intensity, exceeds the fracture toughness substrate or interface to continue propagating. As such, the magnitude of strain applied during layer transfer must be in a range where the ratio of the energy release rate at the fracture tip, G , to the energy release rate at the interface, G_I , is less than the ratio of the substrate fracture toughness to the interface fracture toughness, as expressed by Equation 5.

$$\frac{G}{G_l} < \frac{G_{substrate}}{G_{interface}} \quad \text{Equation 5}$$

3.2 Experimental Methods and Details

3.2.1 Photoluminescence Spectroscopy

Optical material characterization of CdTe films by photoluminescence (PL) spectroscopy was performed using a 0.55 m Horiba Jobin Yvon iHR 550 spectrometer and dispersed onto a LN₂ cooled silicon charge coupled array. Light collection from the film was achieved using a microscope with a 60x objective with a numerical aperture of 0.7. A 130 mW argon ion laser at 488 nm was used as the excitation source and focused to a spot size of 2 μm through the microscope objective. Low temperatures were achieved using an open-cycle helium cryostat.

3.2.2 Substrate Preparation and Growth

CdTe thin films and thin film heterostructures in this section were grown by PLD on 12 mm by 12 mm squares diced from single crystal α-Al₂O₃ (0001) ± 0.5° obtained from the MTI Corporation. Prior to deposition, the substrates were cleaned with isopropanol, methanol, and acetone in ultrasonic baths. Before loading into the vacuum chamber substrates were plasma cleaned for 2 minutes with a mixture of neon, hydrogen and argon at 15 W. Substrates were dedusted with a nitrogen gun and visibly

inspected for surface contamination by reflection and transmission of white light. Substrates loaded into the growth chamber were degassed at 450°C for 1 hour before growth, at a base pressure of 3×10^{-7} Torr.

Targets were abrasively smoothed with a fine grit emery paper to remove the influence of macroscopic surface defects from previous laser interaction, such as trenches, before loading. Targets were also cleaned for 4 minutes at a 2 Hz pulse rate before opening the shutter to remove target surface contaminants. A GSI Lumonics IPEX-848 KrF excimer laser, with wavelength of 248 nm, was used to ablate rotating CdTe (Princeton Scientific, 99.999% purity), Cd_{0.6}Mg_{0.4}Te (5N Plus Inc., 99.999% purity), and ZnTe (5N Plus Inc., 99.999% purity) pressed powder targets, as necessary depending on the desired structure for deposition. The laser spot size was 4.5 mm² and average energy density for ablation was 1.9 J/cm². The beam was rastered along the target radius to prevent trenching and the target-substrate spacing was held at ~9 cm.

During growth, the substrates were held at a nominal temperature of 310°C, as measured by a Pt-Rh thermocouple mounted on the growth furnace surface next to the sample and at the base pressure of the vacuum system. Transferred CdTe thin films relied only on the deposition from a CdTe target source; however, transferred heterostructures involved a combination of ZnTe, CdTe and CdMgTe sources. The design and detailed deposition procedure of those heterostructures is detailed in

subsection 5.2.2, where the device performance attributes are then analysed in subsection 5.3.

Rear side metalization of CdTe and CdTe heterostructures, prior to lamination, was performed at room temperature. Platinum and chromium sources were RF sputtered at a power of 75 W and 50 W, respectively. Copper sources were DC sputtered at a power of 55 W. Sources were sputtered in an argon partial pressure of 4.53 mTorr achieved at a flow rate of 10 SCCM for various deposition times in order to achieve the desired thickness as measured by a crystal thickness monitor in-situ.

3.3 Results and Discussion

3.3.1 Film Structural and Optical Quality after Layer Transfer

The thin film epitaxy of high-quality single crystal CdTe on the complex oxide α -Al₂O₃ has been previously shown,^[44] including demonstrating superior optical properties in comparison to reference bulk CdTe wafers.^[73] During experimentation, to measure the electrical properties of undoped and doped films, lithographic patterning of platinum contacts, in a van der Pauw Greek cross geometry, resulted in the decohesion of CdTe films from sapphire. These films remained bonded to their metal film carrier and intact. Subsequent experimentation demonstrating the ease of layer transfer for larger film areas by peeling with tapes and epoxies, provided initial observations of apparent weak

bonding to the substrate and initiated the detailed interface study and discovery of the spontaneous relaxation of these heteroepitaxial thin films by vdW-like bonding on a Te-terminated sapphire surface, as discussed in Chapter 2.

3DXRD measurements processed into CdTe (111) pole figures for samples prior to layer transfer indicate a dominant single domain with sharp peaks. As seen in Figure 22, the magnified portion of the pole figure for as-deposited films corresponds with a 0.1-0.5% first and second order twin content in the film and a faint central substrate signal bleed-through from the Al₂O₃ (012) reflection tail. 3DXRD analysis post layer transfer to epoxy carriers, reveal no change to the crystal structure of the film from the transfer process, except for the disappearance of the Al₂O₃ (012) reflection tail from the growth substrate.

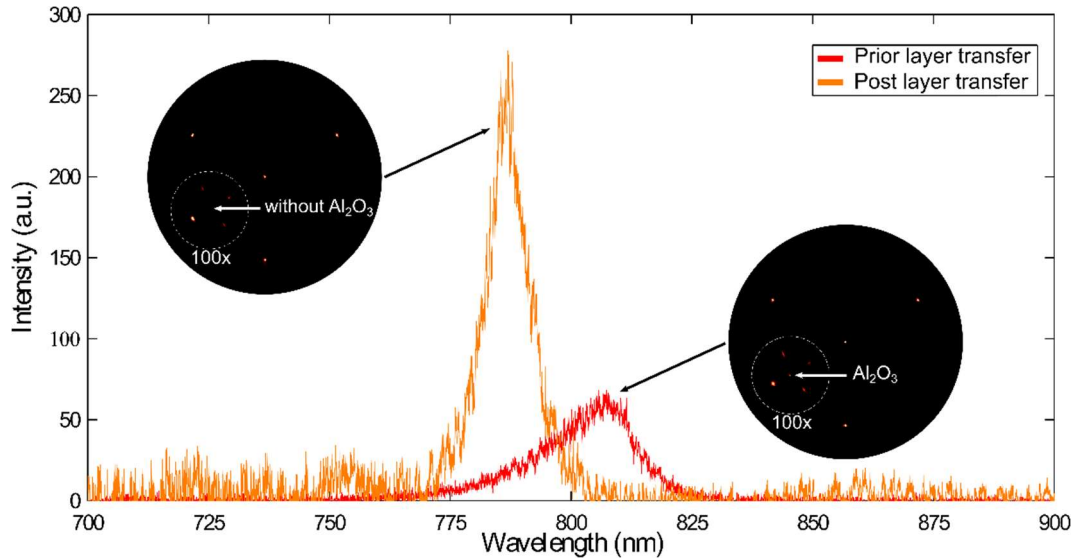


Figure 22: PL and XRD comparison of films prior and post layer transfer. 10K PL spectra for as-deposited CdTe thin films on sapphire and layer transferred CdTe thin film onto an epoxy resin carrier. A blue shift occurs post layer transfer, as well as an increase in PL intensity. Inset: CdTe (111) pole figures post and prior to layer transfer, right and left respectively, demonstrate the disappearance of Al₂O₃ (012) bleed through peak when transferred from growth substrate.

Low temperature PL spectroscopy of films prior to layer transfer, measured at 10 K, demonstrate a single emission at 808 nm with a FWHM of 23 nm, as seen in Figure 22. The line shape of this demonstrates inhomogeneous broadening. Contributions to line width and shape are often divided into two types, homogeneous and inhomogeneous, where at low temperature a Lorentzian and Gaussian line shape, respectively, is expected.^[106] Homogeneous broadening implies that the broadening mechanism effects all transitions in the same way, whereas inhomogeneous broadening implies different local environments for the transitions leading to a superposition of a number of slightly different transitions.

The same film post layer transfer demonstrates a 10K PL emission blue-shifted by approximately 21 nm, with four times the emission intensity and a FWHM reduced by half. The 3DXRD analysis and PL spectra for the pre- and post-layer transferred films are consistent with the preservation of high quality of the film during the handling process. The line shape for post-layer transfer films also exhibits significantly reduced inhomogeneous broadening. It should be noted the post transfer spectrum does not represent spectral emission from an ideal freestanding CdTe film, but rather from one transferred and bonded with epoxy to a glass substrate.

Before the microscopy interface study of the system, it was proposed that the cause of the inhomogeneous broadening was a spatial gradient of strain extending from the interface into the film, seen in the low temperature PL spectra of other heteroepitaxial systems.^[107,108] However, STEM micrographs of the CdTe (111)/Al₂O₃ (0001) cross section FIB samples reveal an abrupt interface and interfacial strain relaxation, due to weak vdW-like bonding between a Te-terminated sapphire surface and the Te-terminated CdTe interfacial surface.

As previously discussed in subsection 2.3, the ionicity of the Cd-Te bond and the non-centrosymmetry of the zinc blende crystal structure require an electron reconstruction at the interface of the polar CdTe (111) on the non-polar Al₂O₃ (0001). The localized π -plasmon observed in the low loss EELS spectra at the interface, attributed to a vdW-like bond, is

indicative of the anisotropic conductivity of electrons travelling along π -bonds at the interface.^[84] Interfacial surface charges at vdW interfaces and surfaces for chalcogenides and non-chalcogenides has been shown to cause inhomogeneous broadening due to the unscreened Coulombic potential.^[109,110] As such, it is more consistent that the observed low temperature inhomogeneous shape broadening of the PL spectra is due to the interfacial surface charge in addition to any inhomogeneous strain effects which are translated across the weakly bond interface due to thermal mismatch in the film/substrate system during cooling.

The reduction of room temperature (RT) photoluminescence intensity by non-radiative recombination at native surfaces of CdTe, like many semiconductors, is expected,^[111] worsening for thin films as the surface to volume ratio increases. However, the effect of the interfacial surface charge between CdTe and sapphire may contribute to the pronounced quenching of RT PL for thin, ~ 100 nm, versus thick, ~ 300 nm, CdTe films grown on sapphire, as seen in Figure 23. In addition, electrostatic depletion of carriers from the thin film volume towards the surface may explain why earlier doping attempts of CdTe films on sapphire using pre-doped CdTe target material, ~ 100 nm in thickness, was unsuccessful, consistently measuring high resistivity in four-point probe transmission line and van der Pauw geometry.^[112]

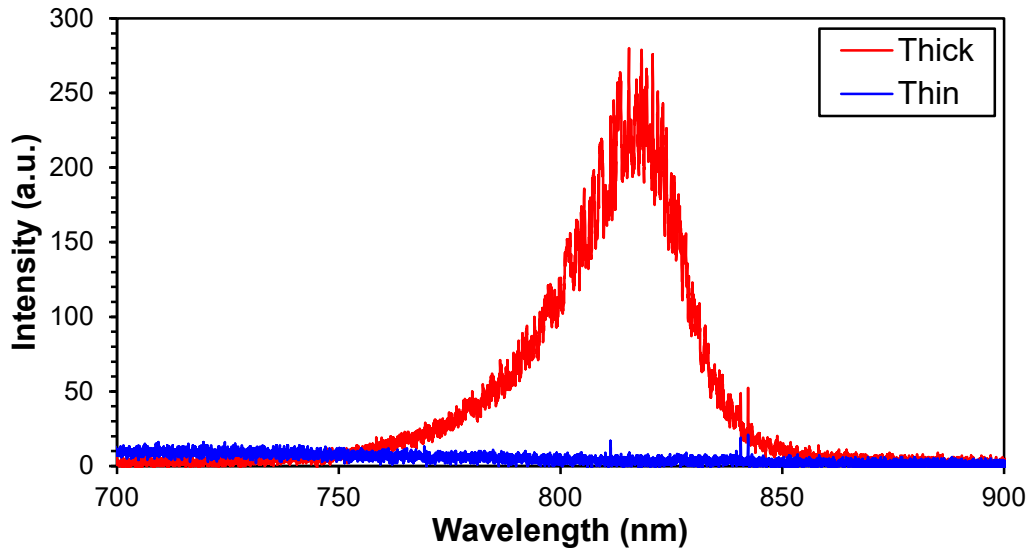


Figure 23: RT PL comparison of thick and thin CdTe (111)/Al₂O₃ (0001) films. Thick and thin films are grown on similarly prepared sapphire substrates by PLD at the same fluence and growth rate, from a CdTe pressed powder target at similar substrate temperature during growth. The thick film was grown longer and had a thickness of ~300 nm while the thin film was grown for a shorter time, having a thickness of ~100 nm. Room temperature photoluminescence intensity appears quenched for the thin sample relative to the thick sample.

Complete lift-off and layer transfer of these CdTe films, while maintaining their high quality, can be accomplished by several methods called mechanical epitaxial lift-off (MELO). MELO provides a route to produce high quality flexible and large area thin film devices, which can be processed and passivated on both sides during device fabrication. As well, layer transfer removes the influence of the sapphire substrate on the device, such as its non-conductive nature or the surface charge at the interface.

Additionally, following layer transfer the original sapphire substrates have been utilized for additional CdTe thin film growth through a process

involving thermal annealing. Reused sapphire substrates are heated to 600°C in a tube furnace and soaked for 30 minutes to desorb any residual film or contaminants from the surface and then undergo the same solvent cleaning procedure as detailed in subsection 3.2.2 before regrowth.

Preliminary structural quality study, using 3DXRD, of CdTe grown on reused substrates shows minor variation, as seen in the Figure 24.

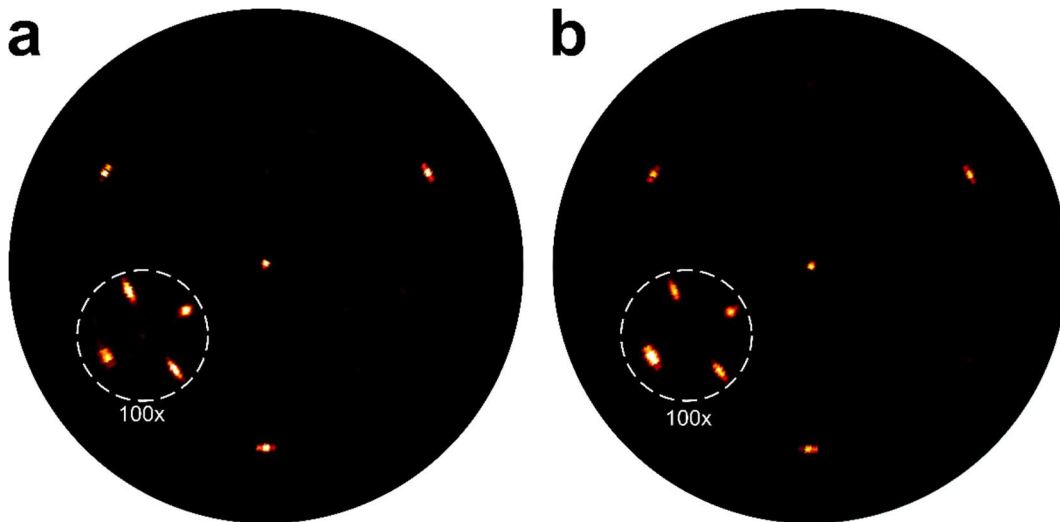


Figure 24: Reusability of sapphire substrate post layer transfer. (a) (111) count normalized pole figure from the 3DXRD data collected for CdTe on α -Al₂O₃ (0001). (b) (111) count normalized pole figure from the 3DXRD data collected for CdTe reused α -Al₂O₃ (0001) substrate showing only minor variation.

3.3.2 Layer Transfer Methodologies: Challenges and Solutions

The simplest method of layer transfer is the uniform application of a strong adhesive tape to a clean film surface followed by peeling, although care must be taken to control the curvature of the tape and rate of peeling to prevent unwanted fracturing of the film. Utilizing Equation 3, the Dundurs' parameter for elastic dissimilarity between CdTe and sapphire is

-0.766, indicating the substrate is much stiffer than the film. Due to this, it is reasonable to assume all bending occurs by the CdTe film during decohesion, with the sapphire remaining stiff and flat, in response to the force applied when peeling with a constant radius of curvature and peel velocity. The generated stress from peeling and associated radius of curvature for the bent CdTe cannot exceed the yield stress of CdTe, ~ 5 MPa,^[113] given the film and tape thickness without inducing fracture of the thin film.

As such, direct manual peeling of films by adhesive tapes did not produce repeatable complete large area yield as a layer transfer technique. Concurrently to testing with tapes, transfer was attempted with liquid adhesives such as cyanoacrylate, two-part epoxy, and UV-cured resins by bonding to rigid glass carriers and applying leverage. Initiating edge delamination proved difficult due to the stiffness of the carrier when bending and often resulted in delamination and glass fracture. Like direct peeling of films with tapes, applying uniform strain during transfer was difficult, in addition, to the strain mainly occurring uniaxially, instead of biaxially, due the directionality of the peel force.

The most mature MELO methodology from preliminary layer transfer study and the focus of refinement and discussion in this section, however, was the use of polymer films about 0.5 mm in thickness. Using polysulfone (PSU), polycarbonate and polymethylmethacrylate sheets, large complete

layer transfer of clean sample surfaces was accomplished by heating the polymer sheet stacked the sample using a hot plate to approximately 50°C to 80°C above their glass transition temperature (T_g) of 186°C, 150°C and 105°C for the listed polymers, respectively,^[114] until the polymer was in a melt state. As the polymer melts it adheres to the CdTe film. After slowly cooling to room temperature the polymer solidifies and an additional peeling force is applied to release the thin films. This original technique, with some caveats to be discussed below, was successful for transferring of CdTe films from sapphire, as well as demonstrating the transfer of ZnTe, $Cd_xZn_{1-x}Te$ and InSb thin films from sapphire.

The use of metallic or polymer handling layer to induce uniform biaxial stress is common to a variety of layer transfer techniques for spalling and decohesion.^[35,95,98,115–118] Such a handle layer is generally removed by dissolving or etching if the film is to be free-standing or remains as a secondary carrier for the device. In-plane biaxial strain from these handle layers is due to lattice and thermal mismatch. The lattice mismatch, as discussed, is given by Equation 1, while the thermal mismatch for a change in temperature, ΔT , and coefficients of thermal expansion for the film and substrate, α_f and α_s , respectively, is given by Equation 6:

$$\varepsilon_{thermal} = \Delta T \cdot (\alpha_f - \alpha_s) \quad \text{Equation 6}$$

Supporting thin film transfer with uniform biaxial tension prevents film wrinkling and buckling, requiring the selection of handle materials with properties yielding positive strain after decohesion or spalling. For spalling layers from wafers, such as silicon, it is common to use a nickel layer.^[95] The nickel/silicon system has a Dundurs' parameter for elastic dissimilarity of 0.218, implying the silicon is compliant. With the nickel film in tension on a silicon wafer, given its lattice and thermal mismatch and the residual tension from the film deposition,^[119,120] edge delamination and spalling of a silicon layer occurs such that it is on the convex side of the bilayer and is kept in tension as the nickel relaxes.

For a PSU sheet on CdTe film on sapphire, the Dundurs' parameter of elastic dissimilarity for the polymer/CdTe system is -0.977. Conversely to the Ni/Si spalling system, this implies that strain relaxation primarily occurs in the soft PSU. When a PSU sheet is placed on a CdTe film/sapphire and is heated on a hot plate for lamination all materials expand due to their positive coefficient of thermal expansion. The difference in lattice and thermal strain between room temperature and the growth temperature for the CdTe (111)/Al₂O₃ (0001) is small, 3.694% versus 3.693%, and can be neglected.

3.3.2.1 Gas Entrapment and Polymer Layer Adhesion

The first major challenge of a polymer lamination technique for layer transfer is the air gap between the PSU sheet placed on the CdTe film. While heating the thick laminate layer exerts virtually no strain on the CdTe during heating. Above the glass transition temperature, in a melt state, the polysulfone wets the CdTe surface as it adheres and ideally pushes out air from the interface. However, as the PSU wets the film surface it may entrap air as illustrated in Figure 25a. Alternatively, gases or solvents dissolved in the PSU may be released at the polymer-CdTe interface as it melts leading to regions of incomplete adhesion.

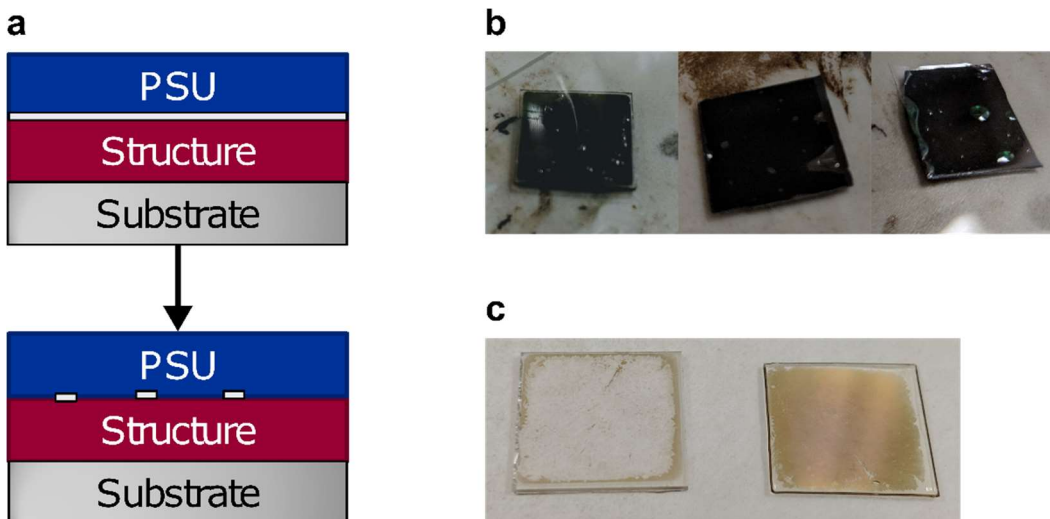


Figure 25: Illustration of gas entrapment during lamination. (a) Illustration of gas entrapment during lamination process shows flat PSU sheets placed on films have a thin air interface with the structure to be layer transferred prior to melting. (b) Above the glass transition temperature, when the PSU begins to wet the film surface, air not pushed out or desorbed through the flow of PSU becomes entrapped preventing adhesion of the polymer to the surface of the film. Alternatively, gas or solvent absorbed into the PSU before melting may desorb at the polymer-film interface during heating leading to regions of incomplete adhesion. (c) Photograph of a layer transferred CdTe film where incomplete adhesion to the polymer carrier during lamination led to incomplete layer transfer and pin holes.

Regardless of the entrapment mechanism during lamination, as shown in Figure 25 b and c, regions of incomplete adhesion lead to non-uniform strain at the interface between the handling layer and thin film. Non-uniform strains between the tensile transfer layer and film for poorly or partially adhered polymers, cause the deflection of the fracture front during decohesion of the CdTe. As such, instead of travelling in-plane and parallel with the weakly bound CdTe/sapphire interface, fracture occurs out-of-plane, leaving residual islands of CdTe on the sapphire and a transferred CdTe film with large or pin-sized holes on the PSU carrier.

Complete and uniform polymer adhesion of CdTe films and devices to be layer transferred can be accomplished by first spin-coating a PSU/cyclohexanone 9.9% weight/weight (w/w) solution before melting of the PSU laminate stack. The CdTe film or device surface on sapphire is first solvent rinsed with isopropanol, methanol, acetone and deionized water then dried with filtered compressed nitrogen and by annealing at 110°C on a glass slide placed on a hotplate for 5 minutes. In order to determine the optimal spin coating parameters, a series of tests on squared silicon wafer pieces, as shown in Figure 26, was conducted by dropping the PSU/cyclohexanone and spinning at 3.25, 3.5, 4.25, 4.5 and 5.5 kRPM for 2 minutes. All coated samples were then baked on a glass slide on a hot plate for an additional 5 minutes at 110°C to degas remaining solvent, and then ramped slowly to the glass transition

temperature, 186°C, and held there for 5 minutes before being allowed to cool slowly to room temperature.

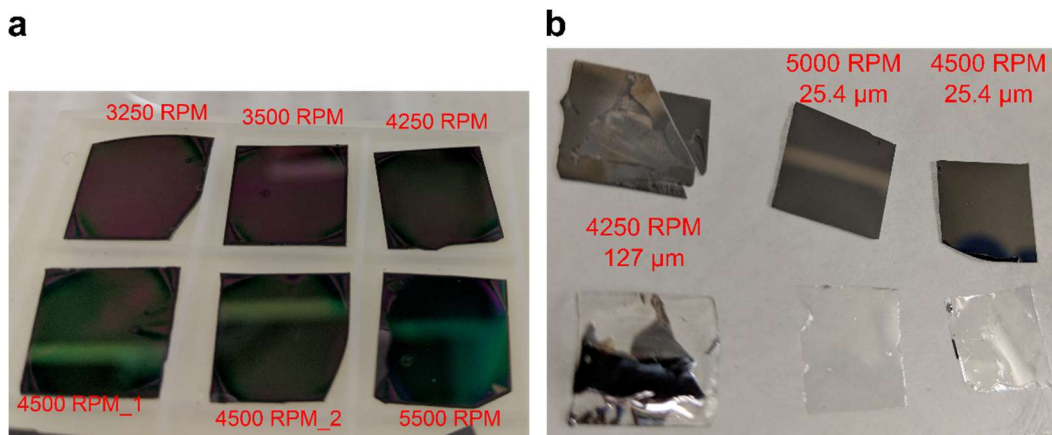


Figure 26: PSU spin coating Si and preliminary adhesion tests. (a) Photograph of 9.9% w/w PSU solution in cyclohexanone spun coat on various cleaned silicon substrate pieces at different speeds. Solutions were dropped from a glass pipette, unfiltered, and allowed to flow before spinning at the indicated speeds for 2 minutes. Coated substrates were then heated to 110°C and held there for an additional 5 minutes to drive out any remaining solvent before cooling back to room temperature. Comets seen in coatings indicate solution required filtering before dropping. Uncoated section of film spun at 5500 RPM allowed for PSU thickness measurement of 648 nm. (b) 25.4 μm PSU sheets were laminated onto Si substrates that had been previously spun coat. Bubble formation occurred when PSU films were held at 50°C above the glass transition temperature, for 5 minutes, leaving some PSU residue on the substrate surface after PSU removal. A 127 μm PSU sheet was laminated onto a pre-coated Si substrate but degassed first under the PSU glass transition temperature. This led to more uniform adhesion of the PSU layer and resulted in spalling of the Si substrate during peel stage of layer transfer.

Two preliminary issues were the appearance of comets in the spin coated film and edge effects. Comets were solved by switching to a glass syringe with a polytetrafluoroethylene (PTFE) 0.45 μm filter. Edge effects were addressed by adding more solution before spinning, flooding the substrate surface until a meniscus was visible. A rotational speed of 4500 RPM was selected since it produced PSU coatings with the smoothest surface measured by alpha-step profilometry.

Thinner PSU sheets, 127 μm and 25.4 μm , cut with a scalpel to the size of the silicon substrate, were prepared by rinsing with isopropanol, methanol and deionized water and then dried with filtered compressed nitrogen. Melting 25.4 μm thick PSU sheets, 50°C above the glass transition temperature, at 236°C for 5 minutes led to the formation of bubbles in the PSU layer and incomplete adhesion leaving sections of PSU on the silicon surface after cooling the laminated substrates to room temperature and peeling.

The 127 μm thick PSU sheet was easier to manipulate with tweezers than the 25.4 μm sheet and thus experienced reduced wrinkling during handling. They could also be mechanically pre-strained by bending with tweezers to a convex shape. This thicker sheet, after solvent cleaning and drying, was preheated to T_g , and held at that temperature for five minutes to degas before being allowed to cool back to 100°C. At 100°C the laminate stack was assembled onto the silicon wafer and then heated together to 230°C and held there for 5 minutes. After allowing the system to cool slowly to room temperature by turning the hotplate off, the interface had no visible regions of non-adhesion and further a peel force on the PSU led to the large area spalling of the silicon substrate beneath indicating a strong uniform adhesion of the PSU, as seen in Figure 26b.

The introduction of these new procedures, spin coating and PSU laminate degassing, before the melting of polymer tensile transfer layer

dramatically increased the transfer yield of CdTe thin films in a reproducible fashion. This technology for MELO was further adapted for the layer transfer of II-VI heterostructure devices, whose properties are discussed in more detail in section 5.3.

3.3.2.2 Adhesion of the Rear Metal Contact

The layer transfer of thin film devices introduces the secondary major layer transfer problem, adhesion between the metalized back contact and the II-VI heterostructure device, as illustrated in Figure 27. Poor metal contact adhesion, like uniform polymer handle layer adhesion, resulted in incomplete layer transfer and large visible holes in the transferred structure to the PSU carrier, even without gas entrapment and uniform polymer wetting of the metal surface.

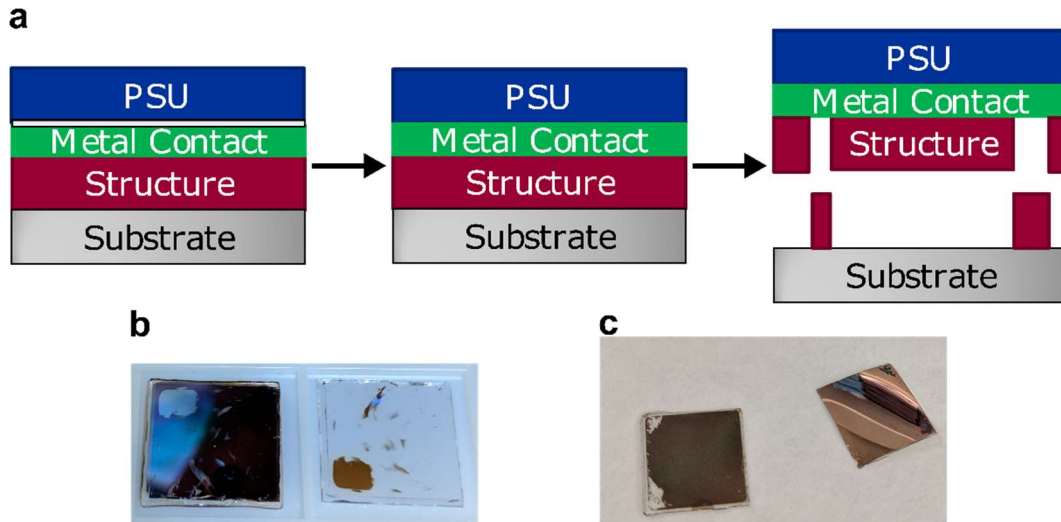


Figure 27: Illustration of poor metal adhesion during layer transfer. (a) Illustration of low adhesion of rear contact to target layer transfer structure on oxide substrate. Assuming no air entrapment and uniform wetting of the metal surface by the PSU laminating sheet, poor adhesion of the metal contact to the semiconductor film leads to incomplete layer transfer and large visible holes in the transferred structure on PSU carrier. Front side metallization of layer transferred films may then lead to shorts and shunts via the through-holes. Photographs of layer transferred CdTe heterostructures with platinum and copper rear metal contacts, seen in (b) and (c) respectively, demonstrating incomplete layer transfer and pin holes due to weak adhesion of the metal film to the heterostructure.

Candidate rear metal contact materials for heterostructure devices, platinum, and copper, were found to have partial or no adhesion, respectively. Incomplete layer transfer of heterostructures metalized with platinum, suffer from shorting and shunting through pin-holes after the front side contact was metalized, whereas copper contacts could be transferred off the rear of the heterostructure completely, leaving the heterostructure intact.

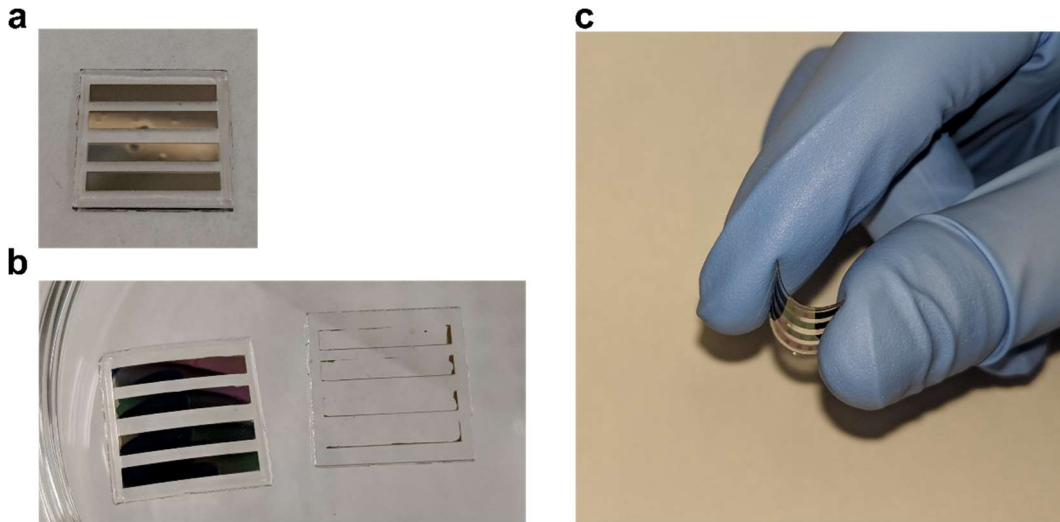


Figure 28: Patterned CdTe heterostructure layer transfer to PSU. (a) CdTe heterostructure is metalized with platinum rear contact with a chromium adhesion layer. PSU 10% w/w solution is first spun through a Teflon filter onto a cleaned metalized surface and then degassed. A degassed and clean PSU sheet is then mechanically pre-stained, so it is plastically curved. Controlled slow melting from the centre to the exterior substrate edges prevents gas entrapment. (b) Upon cooling, a scalpel wedge at one corner between the PSU and sapphire is used to initiate the layer transfer of a large smooth pattern film. (c) The heterostructure on a flexible substrate is then further metalized with front contacts, dark ZnO:Al pads are visible in the image, to complete the device.

Rear contact adhesion to the heterostructure was addressed by the introduction of a chromium interlayer, 5 nm to 10 nm in thickness, before platinum metallization. With this additional interlayer, reproducible and complete layer transfer CdTe heterostructures and films has been demonstrated, including flexible two-side processed heterostructure devices as seen Figure 28.

3.3.2.3 Influence of Tensile Strain Magnitude and MELO Limits

Spalling of sapphire substrates has not been observed during the MELO of CdTe films or heterostructure devices, despite the mechanical

and thermal strains due to the apparent weakness of the CdTe sapphire vdW interface and the high fracture toughness of sapphire. Recalling Equation 6, this implies the right side of the inequality is the larger number. Layer transfer has also never demonstrated spontaneous delamination, instead requiring initiation of an edge crack by wedging between the sapphire and the PSU handle to drive the spontaneous decohesion of the rest of the film or structure.

The energy release rate at the fracture tip, G , is proportional to the product of the stressor layer thickness and the square of the stress in the tensile layer, as seen in Equation 7.

$$G \propto \sigma^2 h \quad \text{Equation 7}$$

Different PSU and Pt rear contact metallization thickness were investigated in order to evaluate the process range of layer transfer in the controlled decohesion regime, with stress above the sub-critical regime for any fracture and below the spontaneous regime where the films delaminate on their own. All polysulfone handle layer thicknesses tested, 25.4 μm to 500 μm , demonstrated controlled interfacial decohesion and remained flat, but flexible after layer transfer. PSU adhesion strength and uniformity for metalized CdTe films and structures was observed to be invariant between 220°C-230°C. As such, the recipe for layer transfer of metalized CdTe films was adjusted to a maximum melt temperature of

220°C instead of 230°C, with the same 5 minute anneal at maximum temperature, to reduce the total layer transfer time.

A gradient of different Pt thicknesses, with a 10 nm Cr interlayer, was also deposited on a heterostructure for layer transfer, visualized in Figure 29, with thickness ranging from ~350 nm to ~650 nm. This provided a spatial gradient of energy release rates for the handle layer across the sample. Regardless of the energy release rate for these thicknesses, transferred films by MELO were still complete and uniform, occurring in a controlled manner when initiated at the edge.

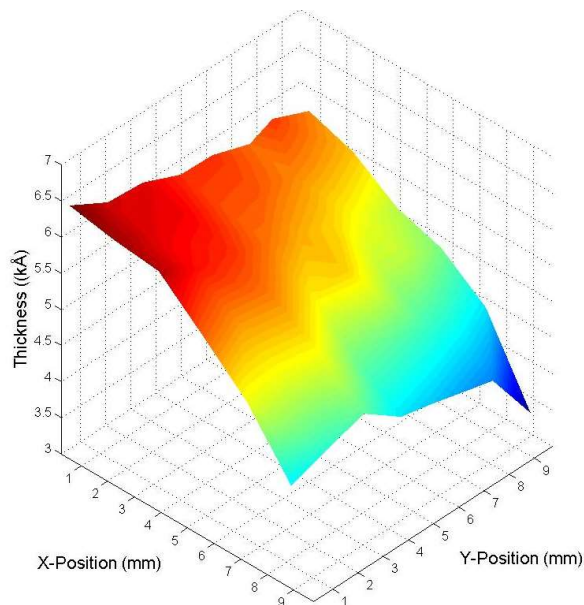


Figure 29: Interpolated thickness of graded platinum deposition. Before sputtering a gradient of platinum thicknesses, a uniform 10 nm chromium layer was deposited for adhesion. Using alpha step profilometry, the thickness of the deposited film and graded platinum contact was estimated, relative to bare sapphire. Data points were collected at various locations to create a thickness grid map.

These results are unsurprising given the known and inferred material fracture properties of the CdTe/sapphire system with a polymer tensile handle layer. The left side of the inequality of Equation 6 is a ratio of the energy release of steady-state substrate cracking to the energy release rate of steady-state interface decohesion. The decohesion number, derived from this ratio, comes from the evaluation of the energy release rate at a depth in the substrate where the shear-strain is zero, and the interfacial energy release rate where the spall depth is zero, $\lambda=0$. It has been demonstrated that the decohesion number for substrate/film is indifferent for thickness ratios ranging from 10 times the film thickness to an infinitely thick substrate, $10 < \lambda_0 < \infty$, however, is strongly dependent on the Dundurs' parameter for elastic dissimilarity.^[18]

For CdTe thin films and metalized heterostructures in this study with thicknesses $\sim 300\text{nm}$ to $\sim 800\text{ nm}$, $1/\lambda_0=0.0006$ to $1/\lambda_0=0.0016$, relative to the sapphire substrate thickness of $500\ \mu\text{m}$ one can assume $1/\lambda_0\approx 0$. As such, fracture by interfacial decohesion or substrate spalling for this material system is dominated by the elastic dissimilarity, a trend which is expected to hold for film and heterostructure thicknesses up to $\sim 50\ \mu\text{m}$.

Recalling the elastic dissimilarity of the CdTe/sapphire system is ~ 0.766 , evaluation of G/G_I by Suo and Hutchison for a system with elastic dissimilarity of -0.8 and $1/\lambda_0=0$ results in a ratio of energy release rates of ~ 0.81 .^[18] Therefore, compared to the fracture toughness of sapphire,

$\sim 3.46 \text{ MPa}\cdot\sqrt{\text{m}}$,^[121] the interface toughness, for the vdW-like bonded system must be much less than $2.77 \text{ MPa}\cdot\sqrt{\text{m}}$ to enable interface decohesion for all magnitudes of applied strain in this study.

3.3.2.4 Optimized MELO and Proposed Scaling of Process Flow

Given the material and system properties for the weak interfacial adhesion of CdTe to sapphire, large fracture toughness of sapphire and the elastic strain compliance of the PSU, MELO has demonstrated robustness and repeatability as a controlled layer transfer method for CdTe films and heterostructures on sapphire. When integrated into standard semiconductor processing, it is proposed MELO can form a closed loop of epitaxial film growth and substrate re-use.

This process is illustrated in Figure 30. The complex oxide substrate sapphire, acting as the epitaxial template, has a heteroepitaxial thin film grown on it. The rear side of this device is then processed with subsequent depositions, etching or metalization to modify that side's electrical or optical properties. Spin coating and PSU melting of the structure, by the described process above, laminates the structure for layer transfer when cooled.

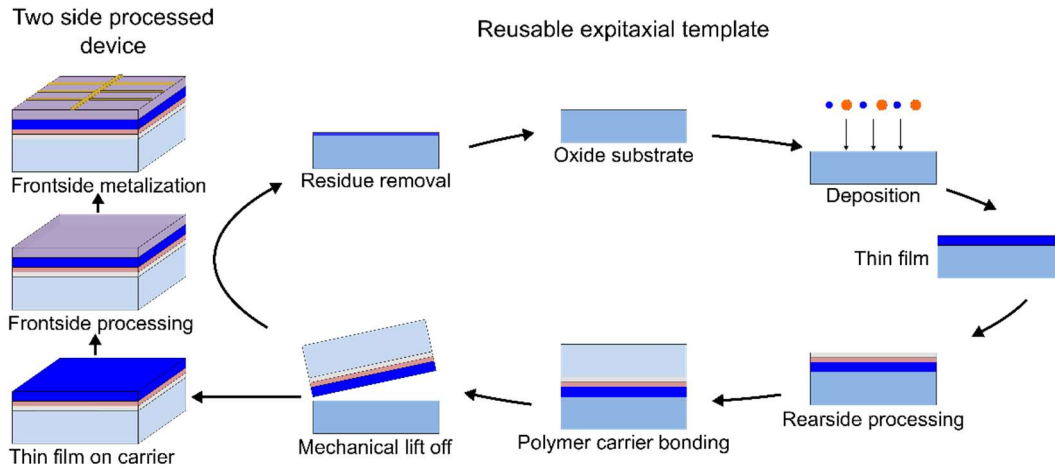


Figure 30: Illustration of layer transfer and substrate reuse process flow.

The initiation of an edge delamination by wedging between the PSU and sapphire allows the layer to be transferred by a mechanical lift-off method. The closed loop for the original epitaxial template occurs with a post-process cleaning step of the sapphire, to remove residual contaminants, before the deposition of the next heteroepitaxial film. Meanwhile the front side of the layer transferred structure, previously inaccessible at the heteroepitaxial interface, is then processed by deposition or etching to modify its electrical and optical properties as required and ultimately metalized for front side contacting to create a two-side processed thin film device. Alternatively, the MELO of a thin film structure could be used to produce freestanding structures, or hybrid structures by first bonding the structure to another carrier and then dissolving the PSU.

3.4 Conclusions

MELO is an epitaxial thin film transfer method which utilizes a film/substrate system, CdTe (111)/ α -Al₂O₃ (0001), with strong enough interaction for heteroepitaxial alignment, but with weak adhesion interaction such that thermomechanical stress can induce decohesion of deposited structures at the interface. Due to the weak binding to the growth substrate and compliance of the polymer handling layer, thin films retain their optical and structural properties following the transfer process to a secondary carrier, leaving the growth sapphire substrate for further reuse. Further, the observed inhomogeneous broadening of low temperature PL and quenching of RT PL emissions of thin CdTe films on sapphire, compared to layer transferred and thick CdTe films on sapphire respectively, is consistent with the surface charge observed at the interface in the low-loss EELS.

To ensure the complete layer transfer of films using a PSU tensile handling layer laminated onto the surface, surface preparation to achieve uniform biaxial stress was found to be critically important. The thinnest of PSU sheets achieving robust layer transfer was 127 μ m, limited by handling of the polymer sheets with tweezers. Surface cleaning to remove contaminants, spin coating with a filtered PSU/cyclohexanone solution prior to lamination and degassing of the polymer handling layer was introduced to address the issue of uniform adhesion due to gas

entrapment. For layer transferred heterostructures, the addition of a metal adhesion interlayer, 5 nm to 10 nm of Cr, allowed for the adhesion of rear metal contacts to the heterostructures during layer transfer.

Combined, these methods allow for the reproducible and complete layer transfer of CdTe heterostructures and films, including flexible two-side processed heterostructure devices. Spalling of sapphire substrates was not observed during the MELO of CdTe films or heterostructure devices, despite a range of mechanical and thermal strains, nor was the spontaneous delamination. Decohesion, as compared to substrate spalling, was found to be preferred for the CdTe/ α -Al₂O₃ system due of the relative thicknesses of the film and substrate, their elastic dissimilarity and an expected two order of magnitude fracture energy difference between the fracture sapphire compared to the fracture along a surface with vdW-like bonding.

The MELO process window for transfer supports a large range of structure thicknesses and polymer tensile layer strains. Further study is required to support the handling of thinner transfer layers as well as to develop bonding methods for the transfer of CdTe films and heterostructures to other substrates such as silicon to create vertically integrated devices.

4 GaAs on Oxide Preliminary Growth Study

4.1 Relevant Literature and Previous Work

Following the discovery of the ease of layer transfer for CdTe films from sapphire substrates, but before the discovery of the vdW interface, a variety of thin film II-VI semiconductor on oxide systems were tested for interfacial decohesion capability using a polymer tensile layer.

Transferable single crystalline ZnTe and $\text{Cd}_{0.96}\text{Zn}_{0.4}\text{Te}$ heteroepitaxially grown on sapphire were demonstrated. CdTe deposited on MgO (111) substrates was also found to be transferable with a tensile polymer handle, however, 3DXRD analysis found its structure to have two (111) domains with azimuthally broad peaks, instead of being single crystalline.

Preliminary investigation of some III-V semiconductors, InSb and InAs deposited by molecular beam epitaxy on sapphire and yttrium aluminum garnet (YAG, $\text{Y}_3\text{Al}_5\text{O}_{12}$), respectively, also revealed interfacial decohesion of films with a polymer tensile layer, but also when evaluated structurally were not single crystalline. After refinement of the polymer layer transfer techniques for CdTe and CdTe heterostructures, an exploratory study was proposed to investigate the commercially relevant III-V material, GaAs. The focus of this chapter, and goal of the preliminary study, was to evaluate if GaAs thin films could be directly heteroepitaxially grown on one of three oxide substrates with reasonable structure quality

and then be layer transferred using a tensile polymer handle without wrinkling or cracking.

The growth of GaAs films on oxides share many similarities to the growth of CdTe on oxides.^[44] Like CdTe, GaAs has a cubic structure but a smaller lattice constant of $a_c=5.652 \text{ \AA}$. The notion of GaAs/oxide heteroepitaxy is also not a new concept, like CdTe/sapphire heteroepitaxy.^[122–125] The expected lattice mismatch for a domain, with two possible domains, between an aligned GaAs [110] diagonal and twice the $\alpha\text{-Al}_2\text{O}_3$ a-plane spacing, 4.760 \AA , is $\sim 16\%$ with the film in tension. Despite this lattice mismatch, GaAs films have been successfully grown on sapphire by metal organic chemical vapour deposition (MOCVD) and molecular beam epitaxy in literature to produce semiconductor on oxide devices.^[126–128]

GaAs semiconductor on oxide devices have also been grown on the mismatched substrate spinel (MgAl_2O_4), where the best material quality occurred for the GaAs (111) on MgAl_2O_4 (111) system.^[129,130] Both semiconductor on oxide systems attempt to control the interface termination during deposition, utilize buffer layers and require annealing to achieve high film quality and electron mobility.^[127,130] No study, to the author's knowledge, has been conducted towards the intentional layer transfer of such GaAs films since these semiconductor on oxide devices normally utilize their substrates optical transparency, high resistivity and

immunity to radio frequency signals in their device design. As such, effort has been focused on adhesion and film quality for this material system.

A final potential substrate candidate for GaAs on oxide is YAG. Like sapphire it belongs to a centrosymmetric space group, however, it has a cubic structure with lattice constant $a_c=12.01 \text{ \AA}$. Looking at the surface net of YAG (111) there are two possible geometric matches for GaAs. The first is a [100] diagonal match of the half lattice constant with 5.85% misfit in tension. The second, is a rotation of the GaAs cubic structure 45° in-plane relative to YAG, to the $\frac{1}{3}$ lattice constant of YAG with 0.15% misfit in tension.

4.2 Experimental Methods and Details

4.2.1 Molecular Beam Epitaxy

Molecular beam epitaxy (MBE) is a method for the epitaxial deposition of thin films developed by J. R. Arthur, J.J. LePore and A. Y. Cho.^[131,132] It provides a wide range of growth rates, precise control of atomic ratios and allows for abrupt changes in composition. A standard MBE growth system, illustrated in Figure 31, consists of a large ultra high vacuum vessel, sample load lock and a series of evaporation or gas sources.

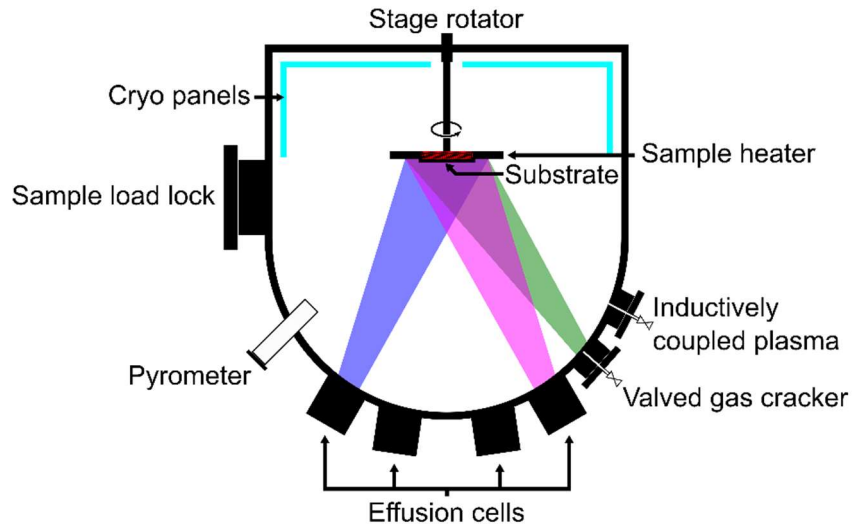


Figure 31: A schematic representation of the MBE system. An unlabeled thermocouple in the sample heater is also used as a mode of temperature measurement and control for the substrate. Effusion cells have unlabeled mechanical shutters. Some effusion cells are used for source material, while others are used for doping.

Due to the high vacuum, atomic and molecular species have a long mean free path and travel in beams from their source. Abrupt changes to thin film composition are possible by allowing or preventing these beams from reaching the substrate with mechanical shutters. Evaporative sources rely on effusion cells, which use high temperature ceramic vessels to heat a pure solid material in a controlled manner until it evaporates; the evaporation rate is temperature dependent. Effusion cells can also be used to produce lower flux dopant sources from a solid, by using the overpressure of a species component during its material decomposition, e.g. Ga_2Te_3 can be decomposed into tellurium vapour and liquid gallium when melted in a certain temperature range.

Gas sources rely on metalorganic or hydride gas species which contain a species of interest. Regulating their flow through a mass flow controller, to adjust the amount of gas entering the system and thus the species flux, these gases can be decomposed or ‘cracked’ using high temperature filaments to generate a beam of the species of interest. ‘Crackers’ may also be used to further decompose evaporated material into smaller species for improved incorporation into the film.

4.2.2 Substrate Preparation and Growth

An SVT Associates gas-source MBE at McMaster University was utilized to deposit GaAs on oxide substrates. Up to six samples were loaded through the load lock per growth into a molybdenum holder, which was mounted to a rotating resistive heater in the deposition chamber. Oxide substrates were diced from bulk wafers from MTI Corporation, into 5.45mm by 9.45 mm rectangles.

Prior to loading, the rear side of the oxide substrates were metalized, protecting the epi-surface during deposition, with 5 nm of titanium and 300 nm of platinum. This allowed for pyrometry prior to deposition since all three of the uncoated oxide substrate candidates are transparent in the infrared. The substrates, with care to prepare the epitaxial faces, were cleaned with isopropanol, methanol and acetone and then treated to a

two-minute 15 W plasma cleaning using a neon, hydrogen, and argon gas mixture.

Temperature of the sample was measured using a pyrometer and a thermocouple mounted near the holder. Prior to growth, substrates were degassed for 15 minutes at 300°C in ultrahigh vacuum. Sample batches were grown at different constant temperatures of 350°C, 450°C, and 525°C, to evaluate the effect of growth temperature on the structural quality of the deposited films.

Desorb and pre-growth steps were also performed, without the use of an inductively coupled hydrogen plasma, for 5 minutes each. For samples deposited at substrate temperatures of 350 and 450°C, the desorb and pre-growth steps occurred at 400°C and 500°C, respectively. For depositions at a substrate temperature of 525°C both desorb, and pre-growth also occurred at 525°C. Growth rates were held at 0.5 $\mu\text{m}/\text{hour}$, using a solid gallium and AsH_3 gas source.

Films in this section were not extrinsically doped during growth, however, the system has the capability to dope the films p-type or n-type with beryllium and silicon solid dopant sources. It also has an indium solid source and PH_3 gas source to deposit lattice matched InGaP layers on GaAs.

Rear side metallization, to improve adhesion to the polysulfone to the GaAs films, was performed by e-beam evaporation of a standard p-type

contact recipe: 25 nm of titanium, 45 nm of platinum, and 120 nm of gold with thickness as measured by a crystal thickness monitor in-situ.

4.3 Results and Discussion

4.3.1 Structural Analysis of GaAs Films on Oxide Substrates

Structural analysis of heteroepitaxial GaAs films on the three candidate oxide substrates was carried out by 3DXRD and texture analysis, techniques discussed in more detail in subsection 2.2.3. Pole figures were generated from captured XRD frames, taken with a 2° spacing, for GaAs (111) as well as the closest low index of reflection from the substrate to determine the relative orientation of the films. Recall that for non-ideal epitaxial growth, the experimental pole figures are a convolution of the diffraction intensity from several crystalline sources. Broadening of the diffraction peaks radially is due to a distortion of the unit cell due to strain. Azimuthal broadening, however, indicate individual crystalline regions in the film are misaligned in-plane.

Simulated pole figures for GaAs, Al_2O_3 , MgAl_2O_4 and YAG were generated as seen in Figure 32. The pole figure index and crystal orientation up were selected based upon the predicted surface net matching of the films to the substrates selected. While most diffraction spots are captured in the experimental pole figures, diffraction spots on

the pole figure circumference, X-rays parallel to the substrate surface, do not appear for the ranges of 3DXRD data collected.

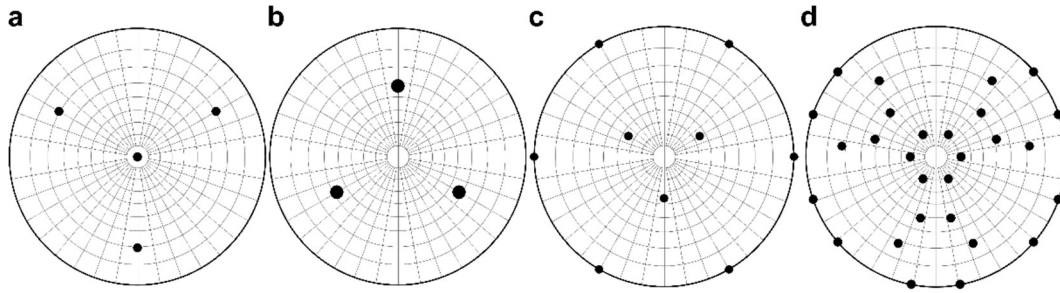


Figure 32: Simulated pole figures of GaAs and three oxide substrates. (a) Simulated GaAs (111) pole figure with [111] direction up. For comparison, the pole figures for the three oxides are generated at the closest allowed 2θ peak, (b) Simulated Al_2O_3 ($10\bar{2}$) pole figure with [0001] direction up. (c) Simulated MgAl_2O_4 (220) pole figure with [111] direction up. (d) Simulated $\text{Y}_3\text{Al}_5\text{O}_{12}$ (321) pole figure with [111] direction up. Diffraction spots appearing on the polar net limits for spinel and YAG are from X-rays parallel to the substrate surface and will not appear in experimental pole figures for the ranges of 3DXRD data collected.

Based upon the methodology described in subsection 4.2.1, two sample sets of GaAs films, 250 nm in thickness, were grown by MBE on all three prepared oxide substrates at a constant growth temperature of 350°C and 450°C for comparison. An additional third sample set of GaAs films, of the same thickness, were grown on sapphire and spinel at a constant growth temperature of 525°C as well. Films grown on all substrates, at all temperatures visually appear optically smooth and mirror like. Further, the structural quality of films on all substrates appeared to increase with growth temperature.

Despite the two potential surface net matches, and the lowest projected mismatch strain for any surface net match of the oxide substrates considered, GaAs films on YAG (111) substrates were

polycrystalline, but not randomly oriented, for both growth temperatures as seen in Figure 33. A presumptive surface net match does not infer successful epitaxially latticed match growth since it does not consider chemical compatibility, substrate topology or surface reconstructions. In this case, the alignment of GaAs (111) planes has some in- and out-of-plane preference to the YAG (321) planes but are not epitaxial since they are not well-defined orientations.

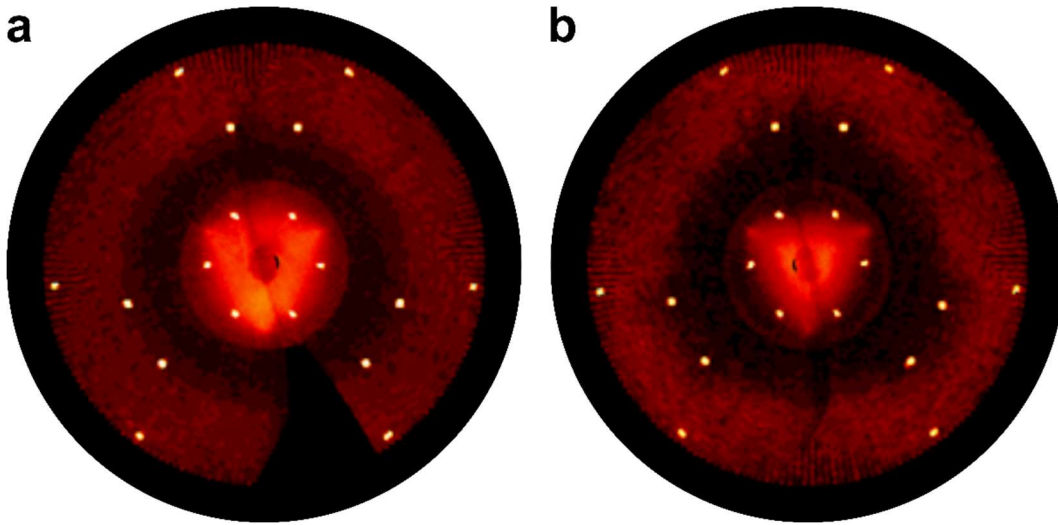


Figure 33: Polycrystalline GaAs on YAG substrates. GaAs (111) pole figures generated from the 3DXRD data collected for GaAs on YAG (111) for samples grown with a substrate temperature of 350°C and 450°C shown in (a) and (b), respectively. Bleed through of YAG (321) peaks into pole figures agree with the simulated pole figure values. GaAs (111) texture indicates films are polycrystalline, but not randomly oriented for both temperatures. The three-fold symmetry of YAG substrates appear to influence but not restrict the in- and out-of-plane orientations of the GaAs film. Missing pole figure information for region of non-interest seen in (a), is due to experiment collection error, which was corrected for the collection of data seen in (b).

GaAs films grown on MgAl_2O_4 (111) had a strong propensity to align their [111] direction perpendicular to the substrate's surface, as seen in Figure 34. While a fibre textured polycrystalline structure with no in-plane

alignment was observed for GaAs films on spinel grown at 350°C, a highly textured structure with strong two domain in-plane alignment appears when grown at 450°C. These two domains share equal diffraction intensity at this growth temperature.

At a substrate growth temperature of 525°C, one domain dominates, with approximately ~90.2% of the intensity, aligning the GaAs $(11\bar{1})$, $(\bar{1}11)$ and $(1\bar{1}1)$ planes with the spinel $(11\bar{1})$, $(\bar{1}11)$ and $(1\bar{1}1)$. The secondary domain with ~9.8% of the intensity is a 180° rotation of the first. At this higher growth temperature, there is still some evidence some in-plane misalignment that is polycrystalline in nature and secondary twins from both domains.

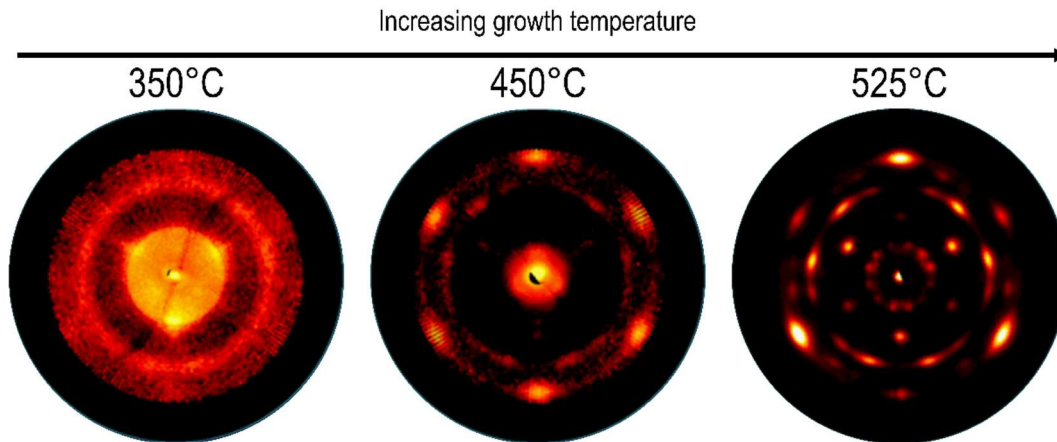


Figure 34: Summary of GaAs (111) on spinel pole figures. GaAs films grown on spinel were all optically smooth and mirror like, indicating the increased growth temperature across experiments did not cause macroscopic surface roughening. GaAs films on spinel transition from polycrystalline with fiber texture to having texture with two equivalent domains when grown at 350°C and 450°C, respectively. Further improvement is seen at a growth temperature of 525°C, where one domain dominates 90.2% of the intensity, which aligns the GaAs (001), (100) and (010) peaks align parallel to the spinel (001), (100) and (010) peaks, respectively. All films exhibit second order twinning.

The growth of GaAs films on c-plane sapphire substrates, as shown in Figure 35, were highly epitaxial even at the lowest growth temperature, presenting one dominate domain rotated 180° such that the GaAs $(11\bar{1})$, $(\bar{1}11)$ and $(1\bar{1}\bar{1})$ peaks align parallel to the sapphire $(\bar{1}02)$, (012) , and $(1\bar{1}2)$ peaks. Increasing the substrate growth temperature from 350°C to 450°C , the dominate domains' relative intensity to its twin, increased from $\sim 70\%$ to $\sim 90.4\%$. Increasing the temperature to 525°C further improved the structural quality of the films by reducing in-plane misorientation broadening and the relative intensity of second and third order twins.

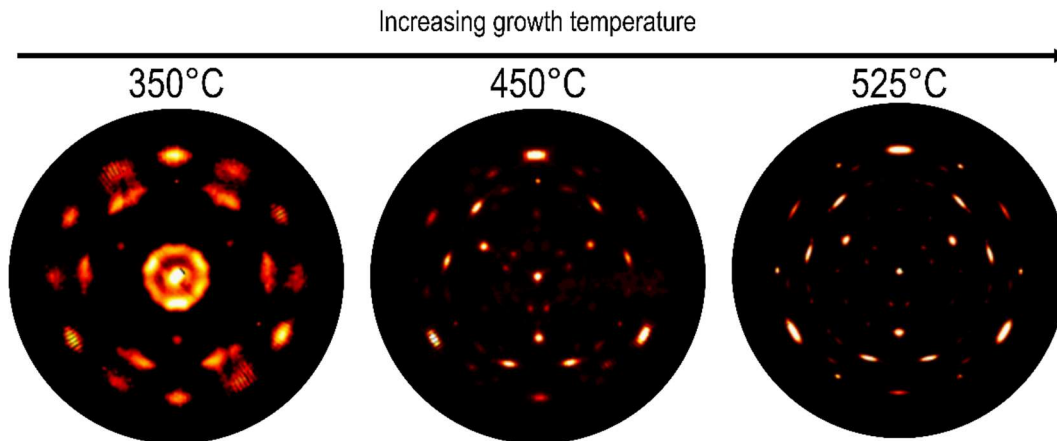


Figure 35: Summary of GaAs (111) on sapphire pole figures. GaAs films grown on sapphire were all optically smooth and mirror like, indicating the increased growth temperature across experiments did not cause macroscopic surface roughening. Even at the lowest growth temperature, 350°C , GaAs films have one dominate domain rotated 180° the $(11\bar{1})$, $(\bar{1}11)$ and $(1\bar{1}\bar{1})$ peaks align parallel to the sapphire $(\bar{1}02)$, (012) , and $(1\bar{1}2)$ peaks, respectively. Increasing the growth temperature to 450°C and 525°C , increases the dominate domain's relative intensity from 70% to 90.4% and associated texture, respectively. An increase in growth temperature improves the structure quality of the films and decreases the relative intensity of secondary twins.

The FWHM of the central GaAs (111) XRD peaks, shown in Figure 36, is also an indicator of film quality. For the growth of GaAs on the three

oxide substrates, increasing the growth temperature was observed to decrease the FWHM of the GaAs (111) peak, consistent with the observations on the pole figures. However, GaAs growth on YAG (111) was not epitaxial like growths on spinel and sapphire, and therefore was not included as a substrate candidate for the third set of samples deposited at 525°C.

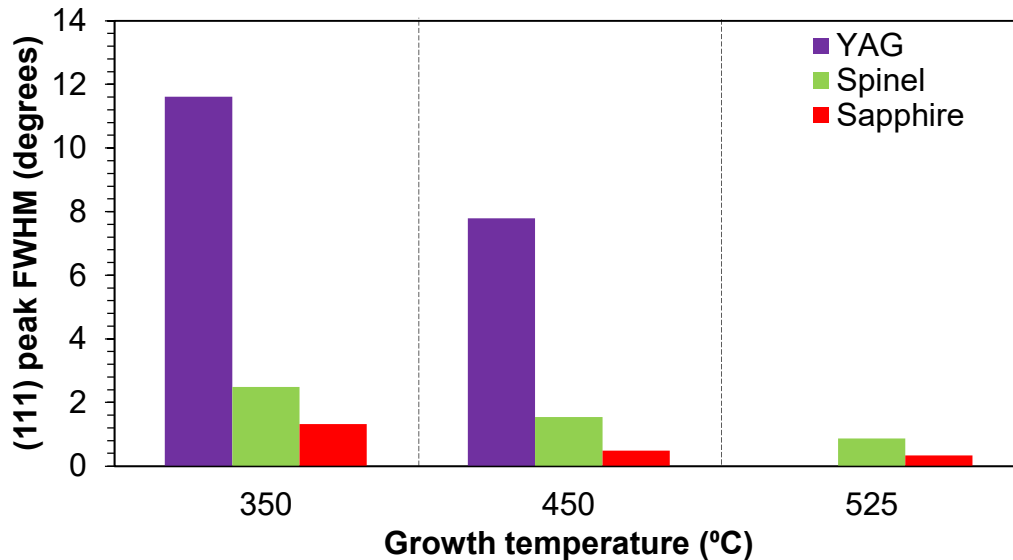


Figure 36: FWHM of GaAs (111) peaks on oxide substrates. The FWHM extracted from 3DXRD data for this low index diffraction peak is comparable to the peak that would be seen for a XRD rocking curve measurement of these films. Increasing the growth temperature for all oxide substrates decreases the FWHM of the GaAs (111) peak, consistent with an increase in quality, with sapphire showing the smallest FWHM across all temperatures.

Growth on sapphire demonstrated the smallest FWHM across all temperature for all substrates, 8 times smaller than growth on YAG and 2 times smaller than growth on spinel. However, even at the hottest growth temperature the (111) peak FWHM for GaAs on sapphire, ~1200 arcseconds, was 60 times larger than the smallest (111) peak FWHM for

the optimized growth of CdTe on sapphire, ~60 arcseconds,^[133] indicating further refinement of the growth is required.

Comparing the GaAs (111) peak positions, by the percent difference between measured film 2θ and bulk 2θ values, allows for additional structural analysis of the films for distortion of their unit cells and residual strain. With positive values indicating residual tension, and negative values indicating compression, the percent difference of 2θ was plotted and grouped for the films by substrate type and temperature in Figure 37. An increase in growth temperature was associated with the relaxation of residual film stress towards the bulk GaAs spacing for all substrates.

Increasing the growth temperature from 350°C to 450°C relaxed all tensile strain in the GaAs films on YAG but did not improve the crystallographic texture. As such, it can be assumed that strain was relaxed by the introduction of defects. GaAs films deposited on sapphire and spinel substrates were observed to be under residual tensile and compressive stress, which was reduced with increasing growth temperature. While GaAs films on spinel demonstrated a greater rate of change for residual stress than films on sapphire as a function of increasing temperature, they also had larger in-plane misorientation comparatively.

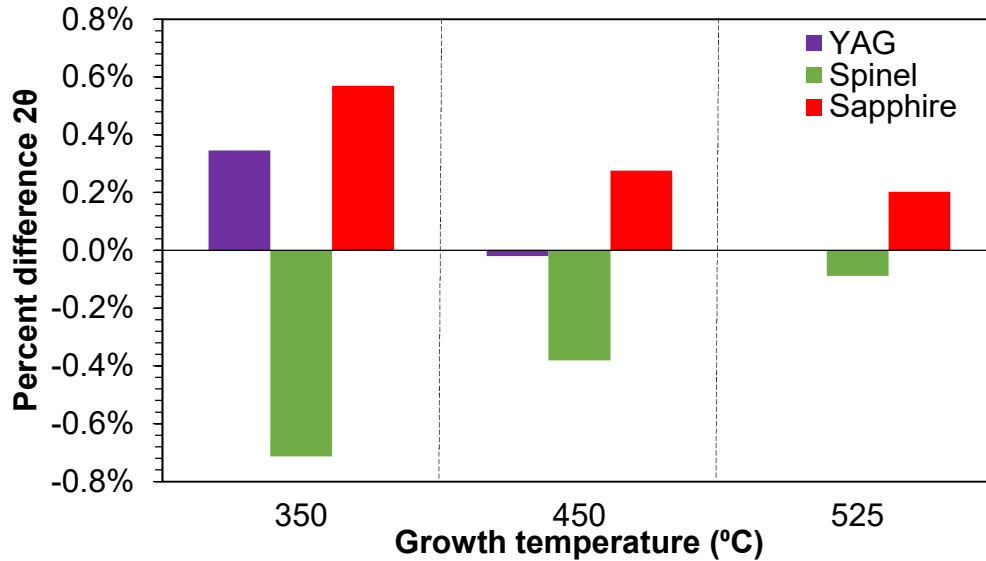


Figure 37: Change in 2θ for GaAs films grown on oxide substrates. The difference of the 2θ films is relative to the relaxed bulk values and is displayed for all experimental growth temperatures. Positive values indicate tension and negative values indicate compression, with smaller absolute values indicating the film is approaching the bulk unit cell. GaAs films on YAG and sapphire experience residual tensile stress, while films on spinel experience residual compressive stress. An increase of growth temperature is associated with a relaxation of residual film stress towards the bulk spacing for all substrates.

The thin GaAs films grown directly on sapphire by MBE present the highest epitaxial quality of the three oxide substrates studied based upon the XRD structural analysis. Literature suggests that the GaAs/sapphire system suffers from poor surface wetting, weak film/interaction and twin formation, however, pre-growth substrate treatments and in-situ annealing have been used to further reduce the twin volume to as low as 2%.^[134] As such, further optimization of the growth of GaAs, on sapphire is likely to yield higher quality films.

Of further interest is the $\alpha\text{-Al}_2\text{O}_3$ ($10\bar{2}$) pole figure from the substrate of a GaAs/sapphire sample, as shown in Figure 38, generated to verify the

epitaxial alignment of the film to the substrate. Observed bleed through of the GaAs (111) peaks into the pole figure, against the bright star like diffraction spots from the substrate, show diffraction intensity streaks occurring between the (111) peaks and their second order twins. These two-dimensional line diffraction features are consistent with the GaAs film on sapphire having planes of coherent twin boundaries and RHEED observations in literature of a Volmer-Weber growth mode for the direct MBE growth of GaAs on sapphire, where in-situ annealing was used to reduce the volume of these low energy twin defects.^[134]

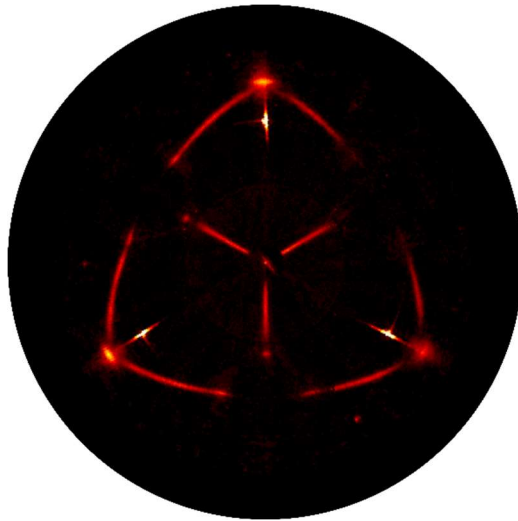


Figure 38: $\alpha\text{-Al}_2\text{O}_3$ (10-2) pole figure for GaAs grown at 525°C. Star like diffraction spots are associated with sapphire while other intensity is mapped to bleed through of GaAs (111) peaks and diffraction occurring between (111) peaks and second order twins.

4.3.2 MELO of GaAs from Oxide Substrates

Layer transfer of GaAs films from all oxide substrates and growth temperatures with a tensile polymer layer was also investigated.

Successful partial layer transfer by the direct melting of 127 μm PSU sheets was observed for all samples without cracking or wrinkling of the GaAs films. Adhesion of the GaAs films to the polysulfone carrier by direct melting was poor in all cases as seen in Figure 39. Increasing the maximum lamination temperature from 230°C to 240°C, did not improve adhesion or gas entrapment and in fact led to bubble formation in the PSU, as shown in Figure 39a.

Introduction of the spin coated PSU layer and degassing of the PSU sheet before lamination demonstrated improved coating uniformity between polymer layer and film, but did not improve the adhesion strength, as shown in Figure 39b. However, inclusion of an adherent standard GaAs contact metallization process, thermally evaporated 25 nm Ti/45 nm Pt/120 nm Au, before spin coating and lamination drastically improved adhesion strength to the structure. Like the metalized CdTe system, the optimal maximum lamination temperature was found to be 220°C, with a hold time of 5 minutes before slow cooling by turning the hotplate off. Through this combined process large areas of optically smooth and uncracked GaAs films were able to be transferred from sapphire substrates onto flexible PSU carriers, as shown in Figure 39c.

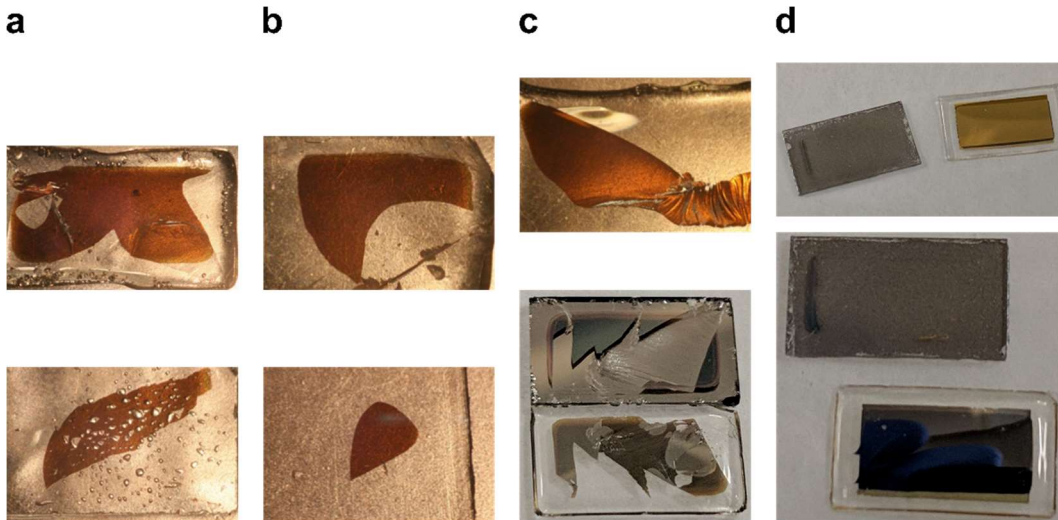


Figure 39: GaAs layer transfer attempts to polysulfone carrier. (a) Brightfield optical micrographs of layer transferred GaAs films on a PSU carrier which demonstrate gas entrapment, and bubbling during the lamination process. (b) Brightfield optical micrographs of layer transferred GaAs films on a PSU carrier which demonstrate incomplete film transfer due to poor adhesion of the polymer to the film. Transferred sections that do adhere are smooth and uncracked. (c) Brightfield optical micrograph and photograph of GaAs films which induced substrate spalling during the layer transfer. (d) Photograph of complete and uniform layer transfer of GaAs film from a sapphire substrate, which has been metallized before lamination. Some unmetallized regions, around the perimeter of the rectangular back film contact remain after transfer from the substrate. The rear contact pad was masked to a slightly smaller rectangular shape than the film deposited, which was rectangular with rounded corners.

For the GaAs films on YAG and spinel, as seen in Figure 39c, substrate spalling was observed for uniform PSU laminations, in addition to partial GaAs film transfer, upon initiation of edge delamination after cooling. Increasing the cooling rate of the PSU lamination exacerbated this problem, increasing amount the of material spalled from YAG and spinel. While above T_g the PSU layer is a viscous liquid, slow cooling of the polymer and laminated system causes the polymer to go through a glass transition at a lower temperature, reducing the strain.

Recalling Equation 7, the energy release rate at the fracture tip increases proportional to the strain squared, and thus rapid cooling of the polymer modifies the inequality of Equation 6 such that the system moves from preferred interfacial decohesion to fracture spalling of the substrate at a steady-state depth where the stress intensity factor of in-plane shear is minimized. Spalling, however, was never observed for the GaAs/sapphire system during layer transfer with a PSU layer.

Optical micrographs reveal thermomechanical spalling features for YAG and spinel substrates, as shown in Figure 40. The fracture toughness of YAG and MgAl_2O_4 substrates are $1.5 \text{ MPa}\cdot\sqrt{\text{m}}$ and $1.2 \text{ MPa}\cdot\sqrt{\text{m}}$, respectively, only ~ 2.5 times smaller than the fracture toughness of sapphire. Despite similar strains from the tensile layer for all three film/oxides system, clear arrest and river line features are visible in the original spinel substrate, as shown in Figure 40a. River lines in spinel, as identified in the magnified region of Figure 40, orient themselves parallel to the fracture front, while arrest lines are oriented perpendicular to the fracture front.^[135]

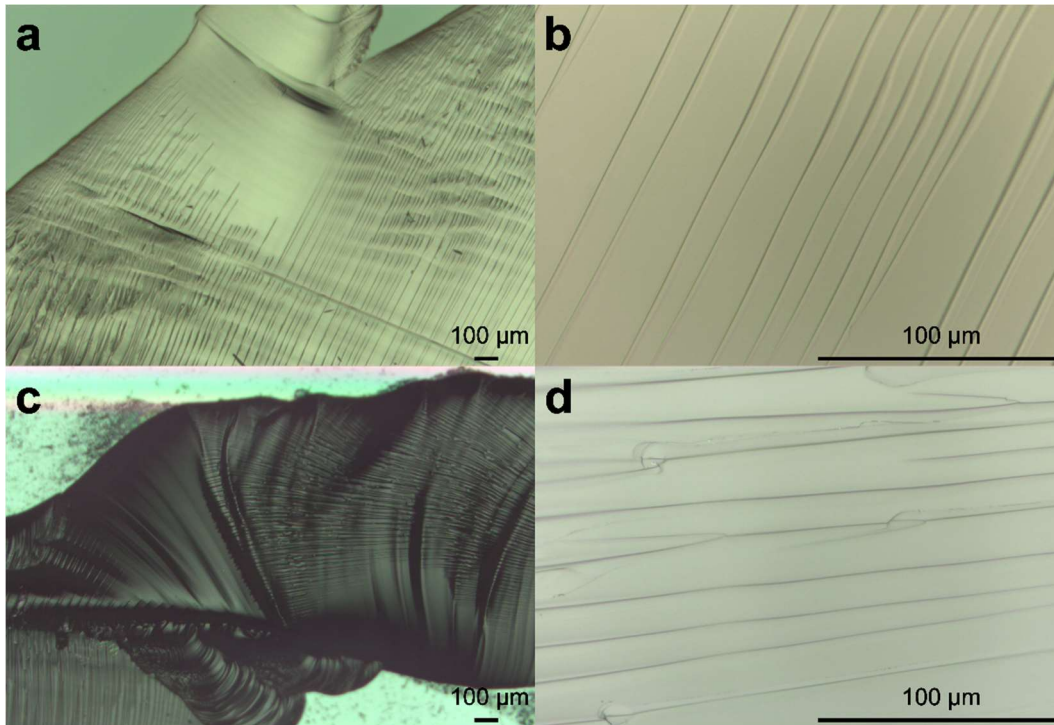


Figure 40: Thermomechanical spalling of spinel and YAG substrates. (a) Spinel substrate optical micrograph viewed under 5 times magnification, of substrate surface after layer transfer demonstrates spall fracture of substrate. Arrest and river lines identified, are perpendicular and parallel to the spall direction, respectively. (b) Viewed at 50 times magnification spall parallel to direction of characteristic branching river lines. (c) YAG substrate optical micrograph viewed under 5 times magnification, of substrate surface after layer transfer demonstrates spall fracture of substrate. Arrest, river, and twist haggles can be identified. (d) Viewing a river line feature set at 50 times magnification, shows more complex fracture patterns in steady-state regions. Rough surface features, which do not align with layer transfer peel direction, result from interacting fracture fronts.

In this case, despite the samples being rectangular and edge delamination being initiated for peel along the length, the major fracture front appears to have moved in the direction of the rectangle's shorter width. Optical micrographs of the spalled surface of YAG, Figure 40 b and c, reveal a much rougher spalled surface, and evidence of interacting fracture fronts which again do not align with the layer transfer peel direction. These observations are consistent with a spontaneous spalling

process for the combined GaAs film and polymer handle layer strains on YAG and spinel substrates.

The Dundurs' parameters for GaAs on YAG, spinel and sapphire substrates are -0.54, -0.49 and -0.66, respectively, indicating substrates are all much stiffer than the films, like for the CdTe/sapphire system. The estimated G/G_I by Suo and Hutchison, assuming $1/\lambda_0 \approx 0$, for systems with such elastic dissimilarity, are in the range -0.5 to -0.7, is 0.81 to 0.82.^[18] The investigated GaAs/oxide systems, and even the CdTe/sapphire system, share similar G/G_I ratios and substrate fracture toughness; thus, according to Equation 5 the primary influence for a system to prefer decohesion to spalling is its interfacial toughness, $G_{\text{interface}}$.

There is a lack of observed oxide substrate spalling in the GaAs/sapphire system, with only observation of controlled interface decohesion. Despite similar polymer carrier thickness and ranges of tensile strain applied during layer transfer process, these observations are consistent with weak enough adhesion between the GaAs/sapphire interface such that the system always favours interfacial decohesion. This behaviour is like the CdTe/sapphire interface, which was revealed to have weak vdW-like bonding at the interface. However, in the GaAs/sapphire system the mechanism of compliance is unknown.

4.4 Conclusions

A preliminary investigation of the growth and layer transfer of GaAs films from oxide substrates utilizing MELO methods similar to those developed in subsection 3.3.2 was conducted. The substrates Al_2O_3 (0001), MgAl_2O_4 (111) and YAG (111) were considered for their potential surface net match to GaAs, and from review of previous attempts in the literature to epitaxially growth GaAs on an oxide substrate. GaAs films deposited by MBE on all oxide substrates at the growth temperatures investigated were optically smooth and mirror like.

3DXRD analysis of GaAs films on YAG (111) revealed them to be polycrystalline, but not randomly oriented in- and out-of-plane relative to their substrate. While films deposited on YAG at a growth temperature of 350°C were in tension, at a growth temperature of 450°C they were measured to be strain relaxed, within the resolution of the XRD instrument, without an improvement of the texture. As such, it is likely that GaAs films on YAG relax strain by the introduction of crystalline defects.

GaAs films deposited on MgAl_2O_4 (111) at a substrate temperature of 350°C were polycrystalline with [111] texture normal to the substrate surface but random in-plane orientation and in residual compression. As the growth temperature was increased, films demonstrated a more epitaxial relationship with the spinel, developing texture with two preferred domains. At the maximum growth temperature, 525°C , GaAs films on

spinel have a dominate domain, with ~90.2% of the XRD spot intensity, aligned such that the GaAs $(11\bar{1})$, $(\bar{1}11)$ and $(1\bar{1}1)$ peaks align parallel to the MgAl_2O_4 $(11\bar{1})$, $(\bar{1}11)$ and $(1\bar{1}1)$ peaks. Despite this improvement, there was still some observed in-plane misalignment and second order twinning.

GaAs films grow with residual tension on Al_2O_3 (0001), demonstrating a $[111]$ texture normal to the substrate surface and strong in-plane orientation alignment for all grow temperatures. Crystallinity and residual strain improved with growth temperature and achieved one dominate domain, approximately 90.4% of the intensity, at a growth temperature of 525°C aligned in-plane such that the GaAs $(11\bar{1})$, $(\bar{1}11)$ and $(1\bar{1}1)$ peaks align parallel to the Al_2O_3 $(\bar{1}02)$, (012) , and $(1\bar{1}2)$ peaks respectively. Small second and third order twin volume fractions were also observed.

GaAs films grown on all substrates at all growth temperatures were able to be partially layer transferred to a PSU carrier by MELO. A spin coating of PSU/cyclohexanone solution was required, like with the CdTe/sapphire system, to achieve uniform contact between the film and polymer transfer layer. However, low adhesion strength of PSU sheets to GaAs films caused the partial transfer of films. This limitation was overcome with the thermal evaporation of an adherent metal contact on the GaAs films before transfer. A combined process was used to

demonstrate the large area transfer of optically smooth and uncracked GaAs films from sapphire substrates.

Despite similar G/G_I ratios and substrate fracture toughness, spontaneous substrate spalling during the layer transfer GaAs films from YAG and spinel was observed but not in the GaAs/sapphire system, where only controlled interfacial decohesion was observed. Since the primary influence for an otherwise comparable system to prefer decohesion to spalling is its interfacial toughness, these observations are consistent with weak adhesion between the GaAs/sapphire interface. The relatively relaxed and highly epitaxial growth of the GaAs/sapphire may also be due to a compliant interface and is worth further detailed STEM cross-sectional analysis.

5 Epitaxial Thin Film Transfer for Flexible Heterostructure Devices

5.1 Relevant Literature and Previous Work

MELO is an epitaxial thin film transfer method which takes advantage of weakly adhered but heteroepitaxially aligned semiconductor films on relaxed oxide surfaces without dangling bonds, such that a polymer tensile layer can be used to separate deposited films or structures at the film/substrate interface. As thin films have demonstrated a retention of their optical and structural properties following successful layer transfer in previous chapters, chapter 5 demonstrates the application of this technique by synthesizing simple crystalline heterostructure devices and transferring them to flexible substrates.

The primary concept applied in the development of these flexible two-side processed devices is the use of heterostructures. Due to the large surface to volume ratio, the electronic properties of thin film optoelectronic devices are often dominated by the electronic structure of their surfaces and at interfaces. Defect states at these positions act as non-radiative recombination sites for carriers, reducing the minority-carrier lifetime and reducing device efficiency (μ). As such, in addition to long bulk carrier lifetimes, reducing the interface recombination velocity for thin film devices is paramount to minimize threshold current in light emitting diodes

and laser diodes,^[136,137] or increasing the efficiency of photovoltaics and detectors.^[138,139]

A common technique employed to reduce the interfacial recombination velocity (IRV) of a thin film device is the use of a double heterostructure design. By sandwiching the active region, e.g. the absorber layer of a solar cell, between two wide-gap barriers, minority carriers can be effectively confined to the narrower-bandgap active region. Further, if the interface between the wide-gap and the active region material is pristine, such as for material systems which are chemically compatible and lattice matched, recombination defects at the absorber interface can be reduced.

One such wide-gap material suited for the double heterostructure passivation of a CdTe active region is $\text{Cd}_x\text{Mg}_{1-x}\text{Te}$. The ternary alloy of CdTe with magnesium is well lattice matched, $\epsilon_{\text{lattice}} \approx 0.7\%$, and a tunable bandgap from 1.5 eV to 2.5 eV for concentrations of Mg up to 68%.^[140] Bulk MgTe is hydroscopic and rapidly oxidizes in ambient air; however, chemically stable ternary alloy compositions have been demonstrated up to $\text{Cd}_{0.4}\text{Mg}_{0.6}\text{Te}$.^[141] $\text{Cd}_x\text{Mg}_{1-x}\text{Te}$ double heterostructure passivation on epitaxial CdTe thin films has demonstrated film carrier lifetimes up to 3.6 μs and interfacial recombination velocities as low as $\sim 1 \text{ cm/s}$,^[111] an IRV comparable to high quality $\text{In}_{0.5}\text{Ga}_{0.5}\text{P}$ and AlGaAs double heterostructure passivation of epitaxial GaAs films.^[137,142]

Two-side processing of thin CdTe double heterostructure devices offers additional advantages to overcome doping limitations and create stable low-resistance contacts.^[138] Heavy p-type doping of CdTe is difficult due to self compensation mechanisms.^[143] Combined with a large electron affinity of 4.28 eV, it is difficult to achieve stable low resistance p-type contacts. Doping limitations also reduce the obtainable quasi-Fermi level splitting in a CdTe absorber, reducing the useful extractable electrical potential.^[144]

However, due to confinement of minority carriers to and passivation of the absorber region by the double heterostructure, contact layers do not have to be high quality or latticed matched, and may even be amorphous, so long as they are strongly selective p-type or n-type contacts.^[138,145] Carrier selective contacts impede the transport of minority carriers while supporting the transport of majority carriers for extraction or injection out of or into the device, respectively. Such a contacting and device design strategy is also utilized by the passivation of bulk crystalline Si wafers with an amorphous silicon layer, to improve photovoltaic open circuit voltage, referred to as a heterostructure with intrinsic thin layer (HIT).

The exploratory tests in this chapter aim to demonstrate the ability for two-sided processing of thin films where it is advantageous to modify the previously inaccessible interfacial surface, independent of the growth substrate for device electrical or optical enhancement. Part of this work

was previously published in *Materials Research Express*,^[62] but also includes more advanced generations of CdTe heterostructure devices and GaAs heterostructures from work conducted.

5.2 Experimental Methods and Details

5.2.1 Current Density-Voltage Measurements

Current density-voltage (J-V) measurements were obtained at room temperature in darkness and under illumination, following the lift-off of the device structure onto a polysulfone carrier. Output J-V curves were acquired using a Keithley 2400 source-measure unit connected to a personal computer and collection software which swept through the voltage while simultaneously measuring the current. The current density was determined by dividing the measured current through the device by the device active area. Contact was made to an exposed section of the rear metalized surface plane and a point on the front surface, front contact pad or metalized front fingers of the device using micro-manipulated whisker type probes.

Samples illuminated with a Newport 96000 solar simulator with AM1.5G filter were calibrated to 1 sun irradiance and measured in a two-point probe configuration. However, J-V curves identified as being illuminated by a solar simulator calibrated to 0.605 sun with an AM1.5G filter, were measured in a four-point probe configuration.

Analysis of the dark and illuminated J-V characteristics was used to extract device properties such as diode characteristics and illumination response.

5.2.2 CdTe HIT Heterostructure Design and Growth

Three generations of CdTe heterostructure devices were fabricated to demonstrate the two-side processing of a flexible transferred structure. Each successive device iteration, as schematically illustrated in Figure 41, attempted to overcome a fabrication or design issue of the previous generation. The basic device structure of all three generations is a HIT photovoltaic cell. Section 5.3 includes a discussion of those issues with the illuminated and dark J-V characteristics measured for each generation of device. A discussion about the limitations of the PLD system, such as the lack of in-situ doping for the CdTe absorber layer, non-uniformities in thicknesses deposited and variation in thin film composition from target stoichiometry, which influenced the device design is also included.

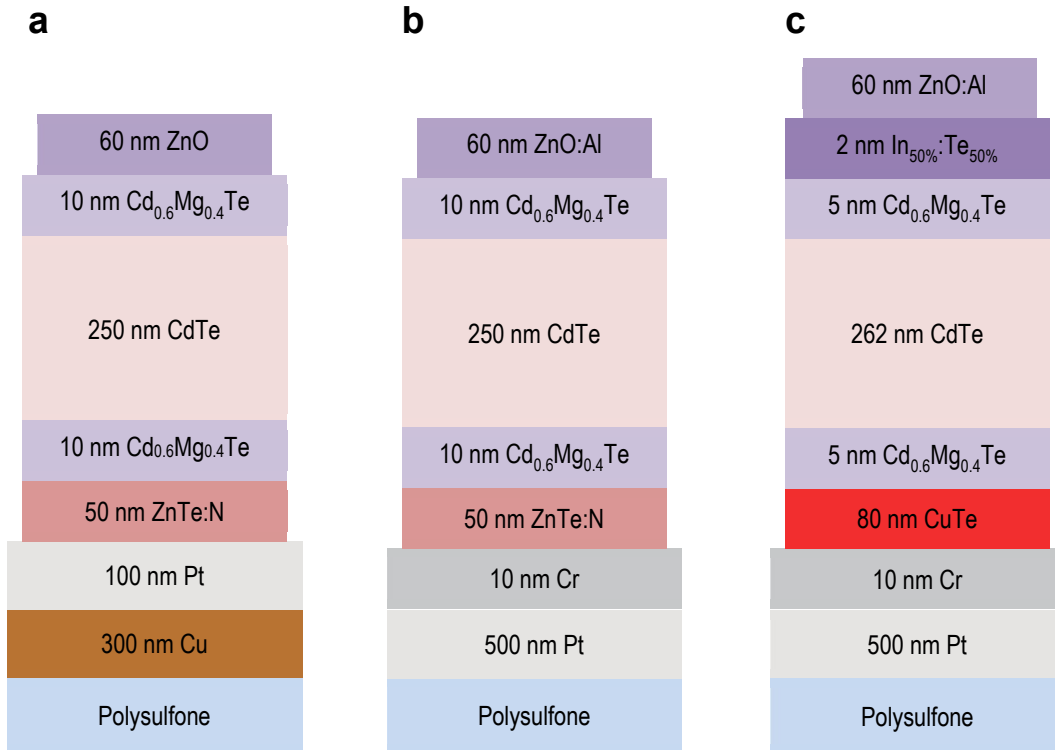


Figure 41: Schematic layer transferred CdTe heterostructures. (a) Illustration of 1st generation CdTe heterostructure layer transferred onto a polysulfone carrier. The presented illustration represents the intended structure, however, variation in thickness occurs due to both the uniformity of the plume and shadowing of the front optic during growth. (b) The 2nd generation layer transferred heterostructure included a more transparent and conductive front window layer, for the electron selective contacting layer, and a chromium adhesion layer for the platinum rear contact. (c) The 3rd generation of layer transferred devices replaced the hole selective contacting layer, ZnTe:N, with cupric telluride. CuTe is intrinsically heavily doped p-type, and the device could be grown entirely in high vacuum. The 3rd generation of devices also reduced the passivation CdMgTe barrier thickness and included a thin film of material ablated from a pressed powder puck of 50/50 blended indium and tellurium powder. These strategies aimed to improve carrier extraction from the intrinsic CdTe region.

All device generations consist of a CdTe absorber passivated in a double heterostructure configuration with an intrinsic wide-band gap but latticed matched Cd_{0.6}Mg_{0.4}Te barrier. Due to in-situ doping limitations of the PLD vacuum deposition system,^[112] the CdTe absorber deposited was also intrinsic. Rectification and separation of charge-carriers is

accomplished by the selectivity of the electron and hole layers on the front and rear side of the structure. Carrier selective contacts form a staggered gap heterostructure with the passivated CdTe absorber, having a difference in their work functions as seen in Figure 42.

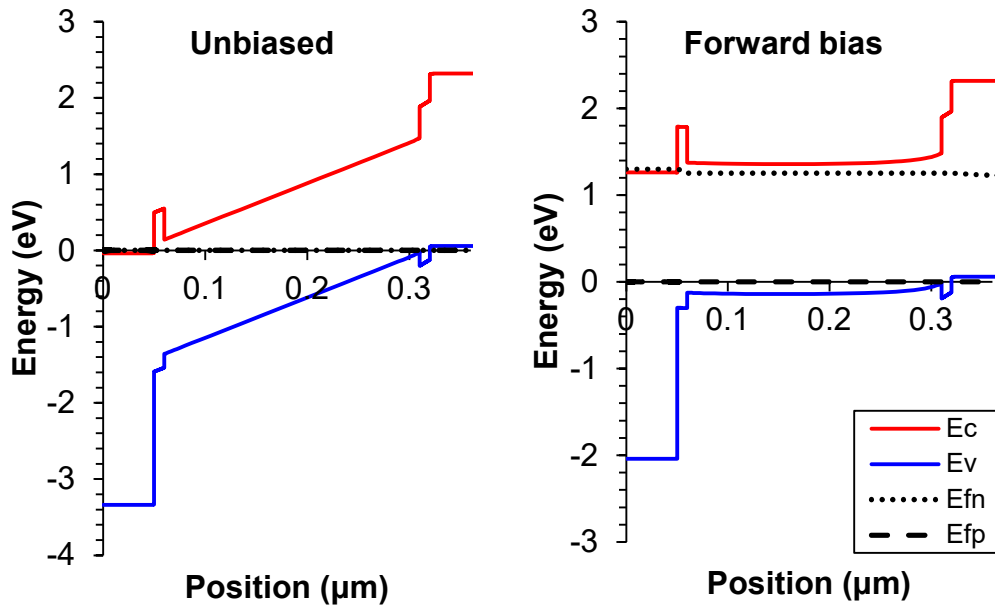


Figure 42: Proposed CdTe HIT heterostructure band diagram. (left) HIT heterostructure is unbiased. Electron and hole selective contacts provide rectification and carrier separation by their staggered gap alignment to CdTe. (right) Forward bias applied to heterostructure bring the CdTe region to an approximate flat band condition by the injection of majority carriers over and through the barriers via thermionic emission, thermionic field emission and field emission mechanisms.

These simulated band diagrams illustrate the conduction band edge, E_c , valance band edge, E_v , electron quasi-fermi level, E_{fn} , and hole quasi-fermi level, E_{fp} , for a generation one CdTe heterostructure predicted upon their fabrication process. Band diagrams and J-V characteristics for idealized heterostructures were simulated using a solar cell simulation software, wxAMPS,^[146] using material parameters from literature,^[138,143]

those included in software package and from measurements of samples grown in-house.^[112] However, these idealized models do not reflect the real band structures of the devices fabricated as illustrated by the non-idealized J-V characterized measures for the devices under test.

Numerical simulation and testing in literature suggest that a layer of highly doped p-type ZnTe and a high work function metal like platinum allow for a low resistance hole selective contact for a CdTe thin film device,^[147,148] with low specific resistivity comparable to acid etched and metalized contacts made to bulk CdTe substrates.^[149] Nitrogen p-type doping of ZnTe has been observed, without the use of a plasma source, by the reactive pulsed laser ablation of ZnTe targets with molecular nitrogen for hole concentrations $\sim 10^{17} \text{ cm}^{-3}$ to $\sim 10^{20} \text{ cm}^{-3}$ depending on the partial pressure of N_2 .^[150,151] This reactive PLD method was adapted in order to form hole selective contacts for generation one and two devices.

CdTe thin film heterostructures were grown by PLD on 12 mm by 12 mm squares diced from single crystal $\alpha\text{-Al}_2\text{O}_3$ (0001) $\pm 0.5^\circ$ obtained from the MTI Corporation. Sapphire substrates and deposition targets were prepared as described in subsection 3.2.2. The PLD spot size was 4.5 mm^2 with average energy density of 1.9 J/cm^2 and the beam was rastered along the target radius during growth to prevent trenching. Substrates were held at a nominal temperature of 310°C during growth.

At the base pressure of the vacuum system, heterostructure growth was initiated with a buffer layer of ZnTe, grown at 0.5 Hz for 75 seconds, to a minimum of 2 to 3 monolayers of complete substrate coverage. A ultrathin buffer layer of ZnTe on sapphire was previously shown to reduce twinning, improve crystallinity and decrease growth process variations for subsequent CdTe layers without impeding layer transfer.^[152] The first and second Cd_{0.6}Mg_{0.4}Te layers were deposited at 1 Hz for 8 minutes and 20 seconds, and the CdTe layer was deposited at 2 Hz for 83 minutes. The rear ZnTe:N hole selective contact was then deposited at a pulse rate of 4 Hz for 500 seconds in a 50 mTorr partial pressure of N₂ gas introduced and maintained by a Granville-Phillips 216 pressure flow/controller.

Following cooling and removal from the vacuum chamber, the rear side of the CdTe heterostructures were metalized by sputtering as detailed in subsection 3.2.2. The heterostructures were then layer transferred to a flexible PSU carrier by the methods described in subsection 3.3.2 and reloaded into the PLD vacuum chamber. Held at a temperature of 100°C, and using an Incoloy sheet mask to define front contact pads areas, ZnO or ZnO:Al transparent electron selective contacts were deposited by reactive PLD of a Zn or zinc alloy (0.9 %w/w aluminum) for 80 minutes in a 13 mTorr partial pressure of O₂. The average energy density of the beam was 2.34 J/cm², with a laser frequency of 8 Hz.

The generation 3 heterostructures used hole selective contacting layers ablated from cupric telluride targets in vacuum, with an average beam energy density of 1.96 J/cm^2 at a growth rate of $\sim 0.5 \text{ }\mu\text{m/hr}$. Cupric is semiconductor with intrinsic degenerate p-type doping.^[153,154]

5.2.3 Two Side Processed GaAs Device Design and Growth

Having also demonstrated the phenomena of epitaxial registry but apparent weak interface adhesion, GaAs layer transferred devices from c-plane $\alpha\text{-Al}_2\text{O}_3$ substrates were also fabricated and investigated. The original proposed device structure, see Figure 43a, was a GaAs pn junction with a rear InGaP heterostructure passivation of the p-type contact. This choice was made since the MBE has the capability of doping III-V semiconductor films in-situ. MBE and substrate preparation were performed as described in subsection 96. Deposition of the first two GaAs layers occurred at a nominal substrate temperature of 510°C a rate of $0.5 \text{ }\mu\text{m/hr}$ with p-type and n-type doping from a beryllium and silicon solid source, respectively. The temperature was lowered to 390°C for the InGaP and final GaAs layer and deposited a deposition rate of $1 \text{ }\mu\text{m/hr}$.

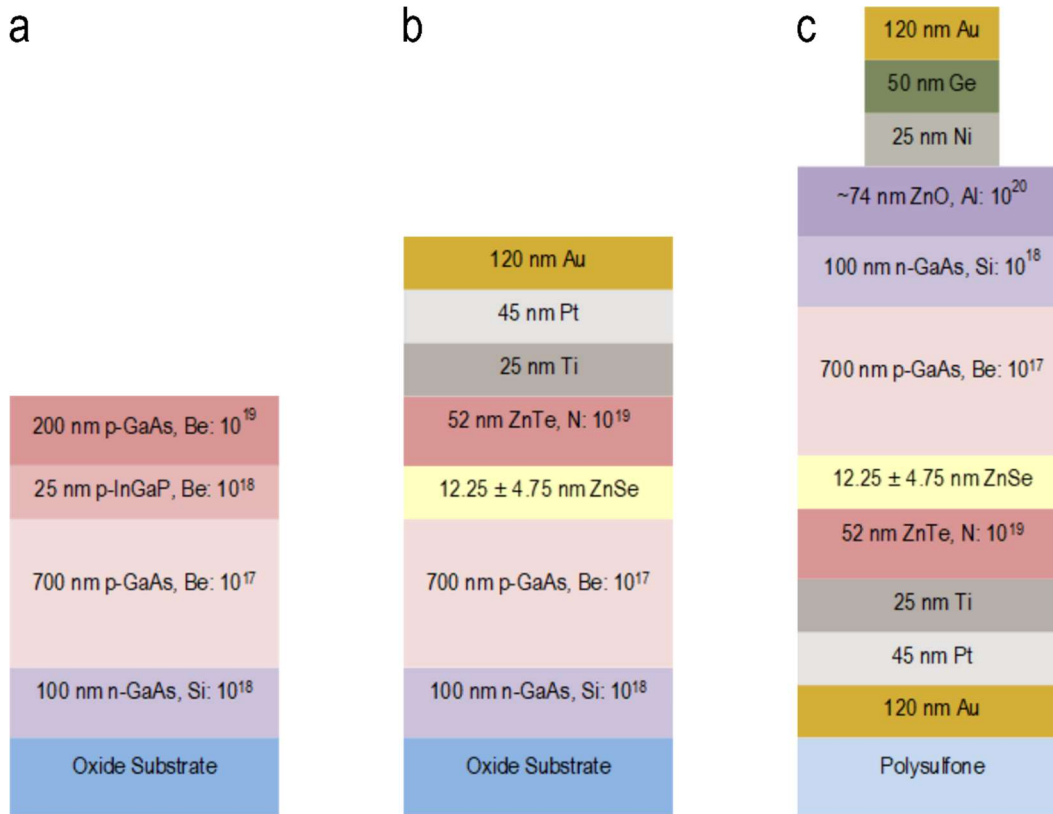


Figure 43: Schematic GaAs Diode on oxide substrate structure. (a) Illustration of proposed as MBE grown GaAs diode structure on sapphire and spinel substrates. (b) During deposition of 25 nm InGaP, low phosphorus content led to clouding and a rough surface in the passivation and GaAs contact layer. The contacting and passivation layer were removed using a selective chemical etch to reveal a mirror like GaAs pn structure. Following a chemical sulfur passivation, the devices were reloaded in the PLD system for a replacement ZnSe and ZnTe passivation and contacting layer. Devices were then transferred to an e-beam evaporator for rear side metallization. (c) After layer transfer to a polysulfone carrier, devices were inverted revealing the n-side of the device. The n-doped faces of the devices were then sulphur passivated and reloaded in the PLD system for a deposition of a ZnO front window layer. The window layer was then metalized by e-beam evaporation with a finger grid contact pattern.

However, during deposition of the 25 nm InGaP low phosphorus content, due to evaporation at temperature without a sufficient overpressure, led to clouding and a rough surface in the passivation and GaAs hole contacting layer. These two top layers were removed using a $\text{H}_2\text{SO}_4:\text{H}_2\text{O}_2:\text{H}_2\text{O}$ (1:8:100) selective GaAs wet etch, followed by a

H₂PO₄:HCl:H₂O (1:1:1) selective InGaP etch. The exposed p-type GaAs layer then had its native oxide removed and surface passivated with a two-hour dip into a solution of 25 mL (NH₄)₂S in H₂O 20% w/w, 4.0 mg of sulfur and 225 mL isopropanol.

These devices were then masked and loaded in the PLD deposition system to deposit a ZnSe heterostructure passivation layer and rear ZnTe:N constant at a nominal substrate temperature of 310°C. The ZnSe layer was deposited in vacuum with 514 laser pulses of average beam energy density of 1.96 J/cm² at a repetition rate of 1 Hz. The hole selective ZnTe:N layer was deposited with identical growth parameters to those for CdTe HIT heterostructures as described in subsection 5.2.2.

After cooling and unloading, the samples were then transferred and loaded into an e-beam evaporator to deposit a 25 nm of titanium, 45 nm of platinum, and 120 nm of gold rear side metallization for a standard p-type GaAs contact to achieve the structure seen in Figure 43b. After layer transfer to a polysulfone carrier by the method described in section 4.3, the inverted device revealing the n-type side was sulfur passivated with the same procedure as described above. A ZnO:Al window layer was then deposited on the passivated surface by reactive pulse laser ablation of a zinc aluminum alloy target in 13 mTorr of O₂.

The structure was then completed with the e-beam metallization of grid patterned front metal contact using a standard n-type contact recipe

for GaAs, 25 nm Ni/50 nm Ge/120 nm Au, to achieve the final device form seen in Figure 43c. While not the originally proposed structure for test, the GaAs structures that were salvaged and processed into devices had an observable photoresponse during illuminated J-V measurement. The predicted band diagram for these devices based upon their fabrication is shown below in Figure 44, but may not reflect the actual band structure of the devices under test.

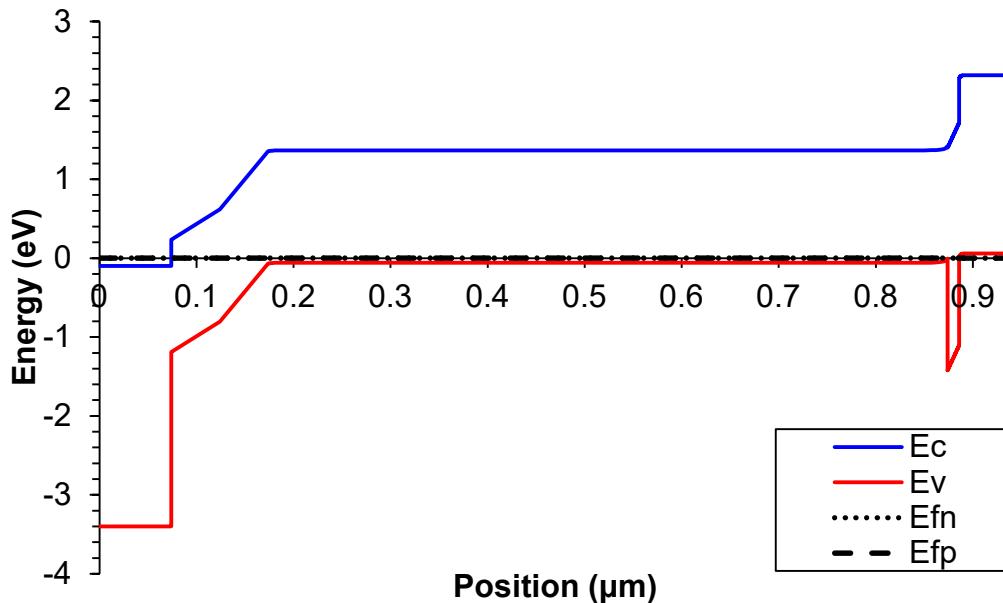


Figure 44: Predicted GaAs layer transfer device band diagram. Band diagram displays device under no bias.

5.3 Results and Discussion

5.3.1 CdTe Heterostructure J-V Characteristics

Initial attempts to create a layer transferred CdTe heterostructure, utilized the polymer tensile layer transfer technique, as described in

section 3.3.2. Generation one device heterostructures, as shown in Figure 41a for cross-sectional illustration, were deposited by PLD on the whole surface of the sapphire substrates as a large square and then metalized with a Pt and Cu back contact, without a metal adhesion layer. The original purpose of the platinum layer was to act as the high work function metal for p-type carrier selectivity and the thicker copper layer was to act as a high conductivity bus.

As seen in Figure 27, poor adhesion of the metal contact to the heterostructure lead to incomplete layer transfer with large and small visible holes in the transferred device on the PSU carrier. Front side transparent contact deposition of ZnO pads, using an Incoloy sheet mask, led to shorting and shunt pathways via the through-holes. The ZnO deposition recipe for the transparent pads was selected based upon UV-visible spectroscopic and electrical characterization of ZnO films on glass substrates, see Appendix 8.1, for the highest transparency and n-type carrier concentration grown by the reactive ablation of a zinc target in partial pressures of oxygen.

As seen in Figure 45, illuminated and dark J-V measurement of generation one heterostructures exhibited photo-resistive behaviour. The change in J-V curve slope for the device illuminated under 1 sun indicated a conductance 1.6 times that of the device in the dark. Weak photocurrent response was detected, leading to a small device open circuit voltage

(V_{oc}) 1.85 mV. Based upon the slope of the illuminated J-V curve at the intersection with the y- and x-axis, the specific series and shunt resistance, R_s and R_{sh} , respectively, were both found to be $\sim 17.4 \Omega \cdot \text{cm}^2$. By comparison, the series resistance of the device in the dark is $\sim 29.0 \Omega \cdot \text{cm}^2$. These similar specific low resistances for the illuminated and dark devices are indicative of device shunting through the visible film holes due to poor metal adhesion during layer transfer.

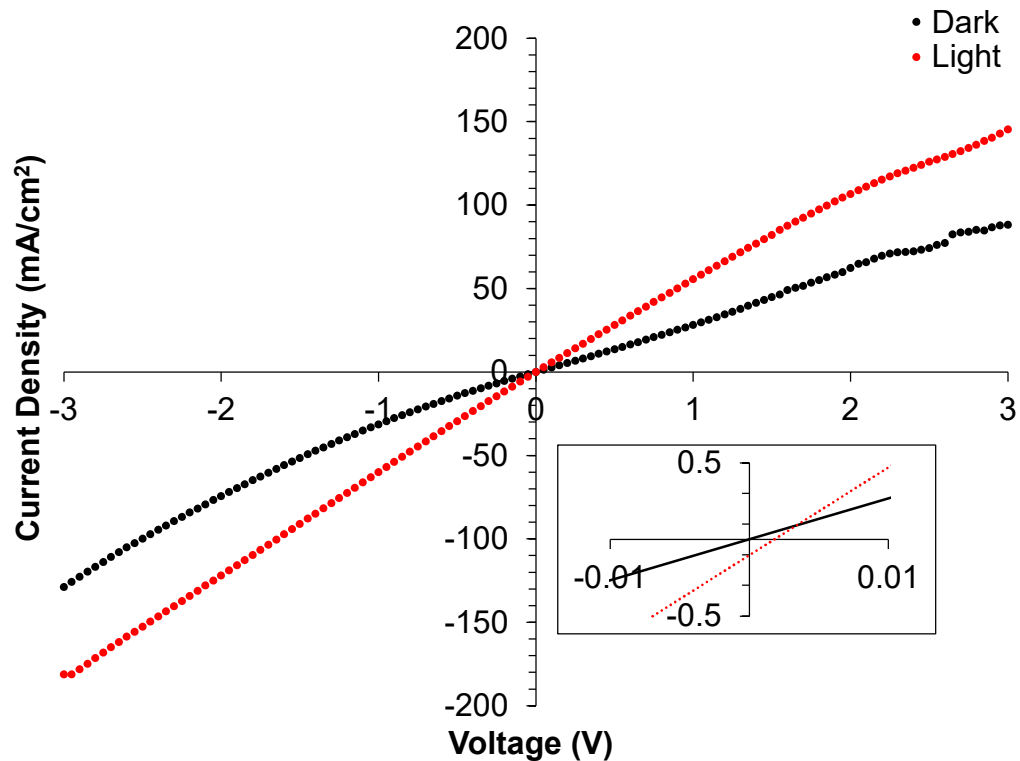


Figure 45: Generation one CdTe heterostructure device, photoresistor. J-V characteristics for generation one CdTe heterostructure contacted on the ZnO transparent front contact pad exhibiting photoresistor behavior activity. The conductance under one sun illumination, as seen by the slope of the curves, increases by 1.6 times in the light when compared to the dark, consistent with photocarrier generation. Inset graph shows a photocurrent shifts the light J-V curve into the fourth quadrant with respect to the dark curve, indicating a photocurrent when illuminated. Visible pin holes in transferred film under the ZnO pad, confirm the photoresistor behaviour is due to shorting between the front and rear contacts.

By instead whisker contacting the CdMgTe passivation layer directly, in a region without visible pinholes, the measured light and dark J-V response of the generation one heterostructure exhibited pronounced rectification, see Figure 46. The consequence of this type of contact is the restriction of the current through the device, due to the large series, resistance. The bypass of the electron selective contact layer to separate and collect photocurrent also eliminates any pronounced photoresponse, when comparing the illuminated and dark J-V curves. However, for a first attempt, the observed ~400 times forward versus reverse conductance and low dark current, with breakdown voltage of more than ~4 V for a device with total thickness of 320 nm, is encouraging that a refinement of the heterostructure two-sided processing and layer transfer may further improve the device characteristics.

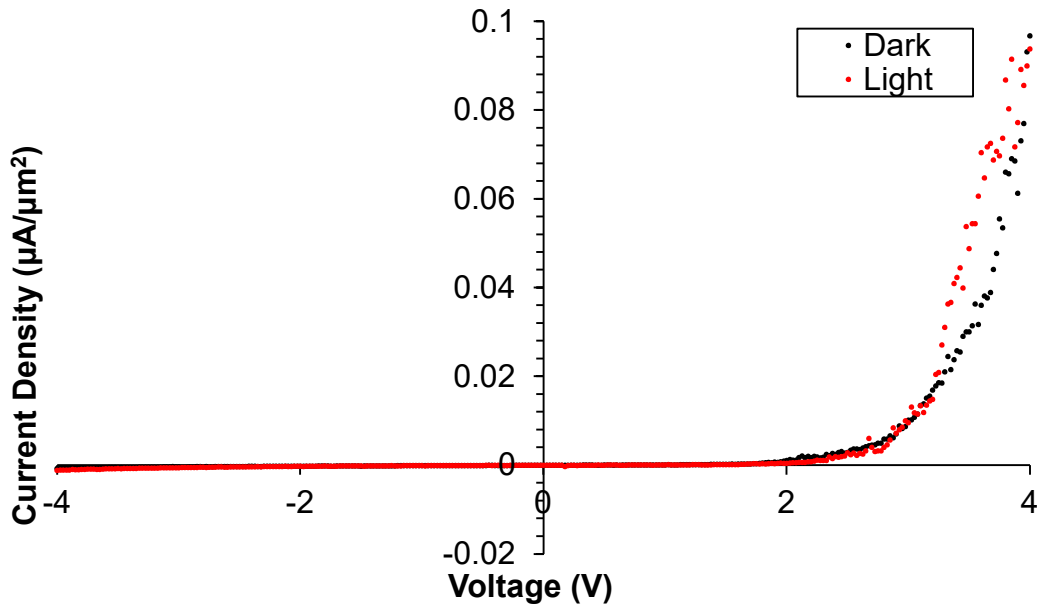


Figure 46: Generation one CdTe heterostructure device, whisker contacted. J-V characteristics for generation one CdTe heterostructure device, tungsten whisker contacted off the ZnO pad, which exhibits strong rectification across a thin film and low dark current, but no measurable photo-response at the origin. Some modification of the turn-on voltage is noticeable under one sun illumination.

The second generation of CdTe double heterostructures, see Figure 41b, were fabricated with a modified process in order to address the major issue of shunting between the front and rear device contacts through pinholes. First, instead of depositing one large square area on the sapphire substrate, an Incoloy mask was used to deposit four rectangular mesas of CdTe heterostructures. Using another Incoloy mask for the front transparent contact allowed for the deposition of multiple of ZnO pads per mesa to create a series of testable devices. Although the alignment tolerance of these shadow masks is poor, especially compared to photolithographic techniques, mesas and ZnO pad separation provided enough isolation to produce a few measurable functioning devices.

Secondly, the rear contact metallization process was modified to include a sputtered metal adhesion layer of 5 nm chromium and then 500 nm of platinum contact. Due to a restriction of only two sputter targets in the system, the copper resistive bus was replaced by a thicker Pt layer. Lastly, the front ZnO transparent contact recipe was replaced with a ZnO:Al recipe utilizing the reactive ablation of a zinc alloy target (0.9% w/w Al) in a partial pressure of O₂, since it demonstrated superior optical transparency, conductivity, carrier concentration and carrier mobility compared to pure ZnO transparent contacts (see Appendix 8.1). These combined fabrication modifications led to the successful layer transfer of generation 2 CdTe heterostructure devices, as seen Figure 28.

While some generation two device pads exhibited poor device characteristics, such as for those whose contact pads were misaligned and overhung on the edge of the mesa, there were a variety of contact pads which demonstrated promising J-V characteristics. A noticeable improvement for one such device under test, as shown in Figure 47, was the observed rectification in the dark between the front and rear contacts.

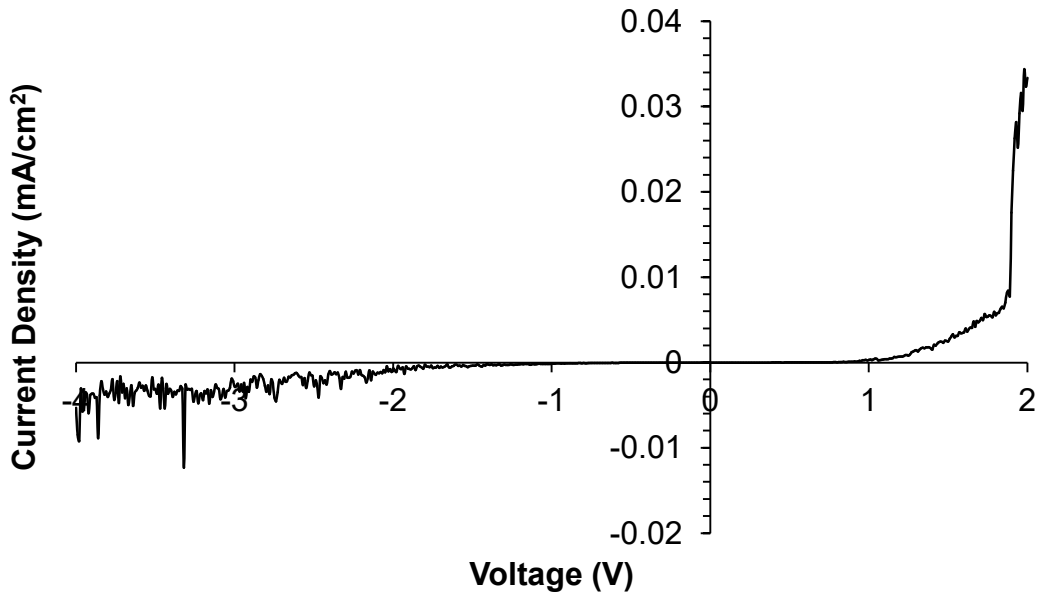


Figure 47: Generation two CdTe, heterostructure, dark rectification. Dark J-V characteristics for generation two CdTe heterostructure contacted on the ZnO transparent front contact pad exhibiting rectification. Device failed into a permanent open circuit under 1 sun illumination measurement. Device pad location row 1 column 2.

Under forward voltage, diode current is due to carrier recombination of the injected carriers from the n-type and p-type contact. The recombination of carriers in the forward voltage is complicated for these double heterostructure CdTe devices with electron and hole selective contacts, especially relative to a simple pn structure, since an applied electric field affects multiple band alignments in the structure by band bending. However, like a simple pn diode, at some forward threshold voltage, the applied potential modifies the band alignment such that the magnitude of recombining carriers becomes large enough to have a macroscopic impact on the measured conductivity, referred to as the diode 'turning on'.

The forward current density scale displayed for the generation one device is different than the scale displayed for the generation two device. While the total current measured is smaller in the whisker contacted device, the contact area ratio of the probe tip versus the deposited ZnO:Al pad is very small. The whisker contacted device, without a ZnO pad, 'turns-on' well before the device measured through a ZnO pad, illustrated below with a log plot dark current plot versus voltage in Figure 48. This is consistent with a device behaviour dominated by the contacting.

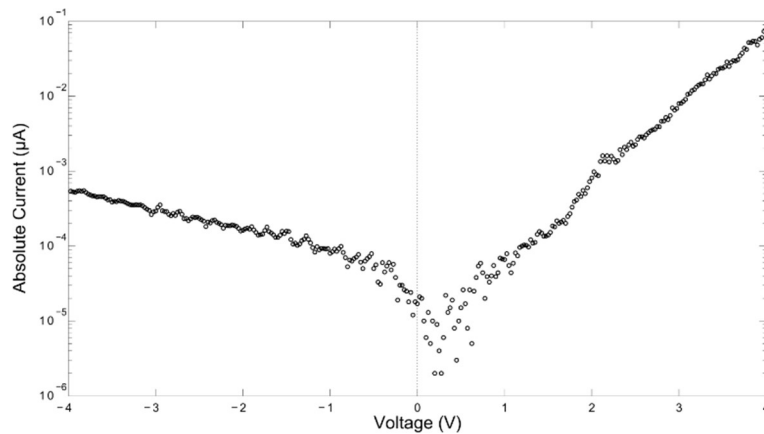


Figure 48: Log dark current-voltage plot for generation one device.

The dark J-V rectification behaviour observed for the generation two device under test, in Figure 47, for an applied forward electric field is primarily dominated by the change in band alignment in the heterostructure by band bending. Thus, it is more indicative of the rectifying behaviour for the intentionally fabricated heterostructure. Unfortunately, this same device under test, in Figure 47, was observed to

be an open circuit in illumination and then again when put into the dark, indicating device failure.

However, other ZnO:Al pads for the generation two device provided repeatable observations of photovoltaic activity in the J-V curves, such as those presented in Figure 49. Setting current and voltage limits on the source-measure unit to prevent device failure revealed a large V_{OC} of 291.1 mV but a small, short circuit current density (J_{SC}) of 0.00163 mA/cm². Another device under test had a higher V_{OC} of 397.9 mV, but a much smaller J_{SC} of 0.00009 mA/cm².

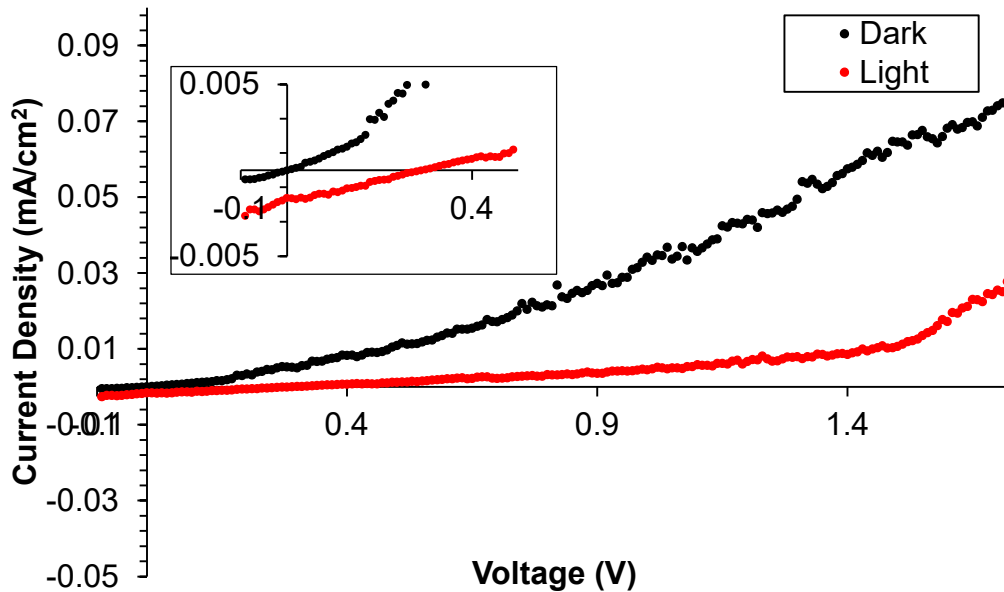


Figure 49: Generation two CdTe, heterostructure, photovoltaic activity. J-V characteristics for generation two CdTe heterostructure device exhibiting photovoltaic power output in the fourth quadrant. Current and voltage limits on the source-measurement unit were set to prevent device failure when illuminated. Inset image shows small J_{SC} and photocurrent, but relatively large V_{OC} . The heterostructure exhibits negative photoconductivity. Device pad location row 4 column 1.

The predominate electrical difference between the J-V curves for these two pads tested, was the device with the higher V_{oc} and smaller J_{sc} had a specific series resistance ~ 83 times and specific shunt resistance ~ 88 times larger than the other. The observation of a relatively large V_{oc} , but small J_{sc} is consistent with effective passivation of the CdTe absorber, but poor carrier extraction over and through the barriers by thermionic transmission and tunneling into the contacting layers. Large bulk carrier lifetime and low IRV lead to larger quasi-Fermi level splitting in an absorber, so that more of the chemical potential can be extracted as electrical potential.^[138] However, the CdMgTe passivation barrier thickness and height, as well as the contact layer doping, dominate the injection and collection of carriers at contacts.^[155]

Interestingly, the illuminated J-V characteristics of the device in Figure 49 also demonstrate negative photoconductivity. This behaviour is weakly observed for the whisker contacted generation one device in Figure 46. Negative photoconductivity has also been observed for modulation doped GaAs/AlGaAs and undoped InAs/AlGaSb double heterostructures.^[156,157] Another unexpected behaviour, as shown in Figure 50, is the apparent negative resistance of one of the generation two device pads. While the photovoltaic device demonstrates a V_{oc} of 551.7 mV and a J_{sc} of 0.173 mA/cm², the largest of both for the generation two devices, it also has a voltage dependant spike in conductivity for forward

bias. Increased conductivity at a specific range of applied forward voltage is speculated to be caused by increased tunneling across a barrier or staggered heterojunction due to favourable band alignment with the applied potential.

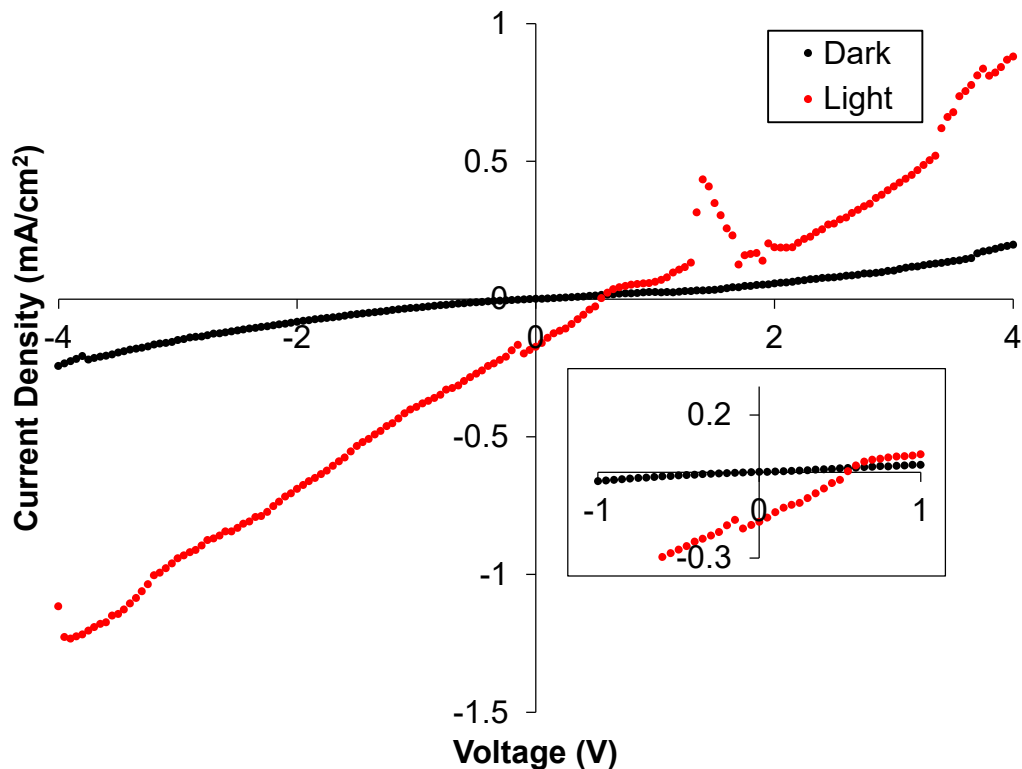


Figure 50: Generation two CdTe heterostructure, negative resistance. J-V characteristics for a generation two CdTe heterostructure exhibit photovoltaic activity in quadrant four and negative resistance in quadrant one under 0.605 sun illumination. Despite this behaviour in quadrant one, this device pad exhibits the higher V_{OC} and J_{SC} of all tested generation two CdTe heterostructures. Device pad location row 2 column 5.

There are a few general observations based on the variability in device performance with different pad locations across the different mesas and the deviation from the expected device performance from the predicted structure. First, the high forward scattering and non-symmetric

plume distribution from PLD has been demonstrated to cause non-uniformities in thickness and composition of thin films.^[158] Secondly, material vaporized which then deposits on optic entry window for the laser reduces the average beam energy density deposited on the target. This compounds to decrease the amount of material ablated per pulse for each subsequent pulse. The PLD system used in this study is better suited for the material research of small areas of thin films, rather than producing large area devices.

Lastly, the rear hole selective contact layer recipe for ZnTe:N, see Appendix 8.2, was developed by trial growths of ZnTe:N deposited by reactive PLD of ZnTe in a partial pressure of N₂ on glass substrates and from literature.^[150,151] Doping efficiency of the ZnTe, due to interaction with molecular nitrogen during PLD, is not considered when the plume energy is reduced as it is the last layer to be deposited. Further, the stoichiometry of the CdMgTe barriers are assumed to be equivalent to the target is stoichiometry, which was not verified in this study from the supplier. This also neglects thermodynamic and kinetic effects which may lead to a change in stoichiometry from the target during growth.

The simulated J-V curves for an idealized generation one CdTe heterostructure, see Figure 51, demonstrate the trend of changes to the barrier height, due to stoichiometry shift of Cd_xMg_{1-x}Te, from x=0.7 to x=0.5, dramatically impact charge carrier collection and the device R_s. A

similar result would be expected for increasing the barrier widths. Also observed in Figure 51 is that low doping efficiency selective contacting layer, ZnTe:N, from $p=1 \times 10^{19}$ to $p=1 \times 10^{13}$, impacts charge carrier collection efficiency and the extractable electrical potential from photogenerated carriers, V_{oc} .

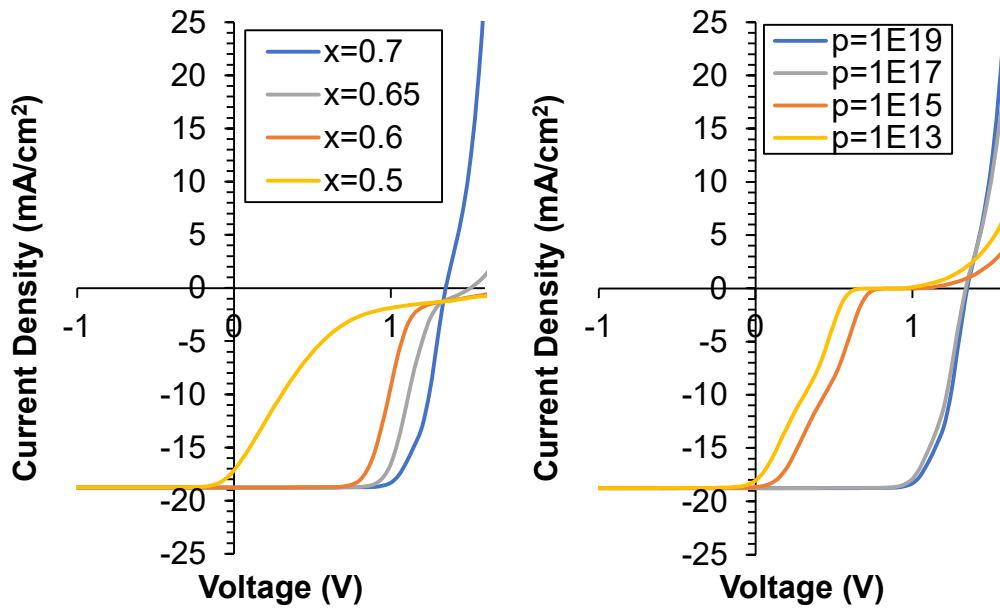


Figure 51: Simulated J-V characteristics of an ideal CdTe heterostructure. (left) The R_s of the photovoltaic heterostructure is increased when decreasing the fractional percentage of Cd in $Cd_xMg_{1-x}Te$ from 0.7 to 0.5. This indicates that deviations from the proposed stoichiometry of the CdMgTe passivation layers increase the barrier height and impede carrier collection efficiency from the CdTe absorber layer. Higher and thicker passivating barriers do reduce the IRV, however, so that the few carriers that are extracted are at a higher electric potential. (right) The effect of decreasing doping efficiency of the ZnTe:N hole contact layer is shown to increase the R_s and decrease the V_{oc} for the idealized device. This is due to the decrease in work function for the ZnTe:N layer, which is dependent on its Fermi level.

The third generation of CdTe devices, see Figure 41c, built on the strategies of the generation 2 devices, but attempted to reduce the double heterostructure barrier thickness, and improve hole contact carrier

selectivity with a intrinsically degenerate p-type layer of cupric telluride. A very thin intermediate indium telluride layer was also deposited between the ZnO:Al contacts and the CdMgTe barrier with the intension of improving electron selectivity at the front contact.

Together these strategies aimed to increase the carrier extraction efficiency to reduce the series resistance. They also attempted to remove the uncertainty surrounding the effectiveness of the ZnTe:N doping. Most of the generation three device pads tested were short circuited, and others failed becoming open circuits after J-V measurement under 0.605 sun illumination, despite attempts to set current limits on the source-measure unit. Of the devices that had observable J-V characteristics in the dark and under 0.605 sun illumination, see Figure 52, one device demonstrated a V_{oc} of 1186 mV, but low J_{sc} of 0.00336 mA/cm² due to a 245 times larger R_s than the best performing generation two device.

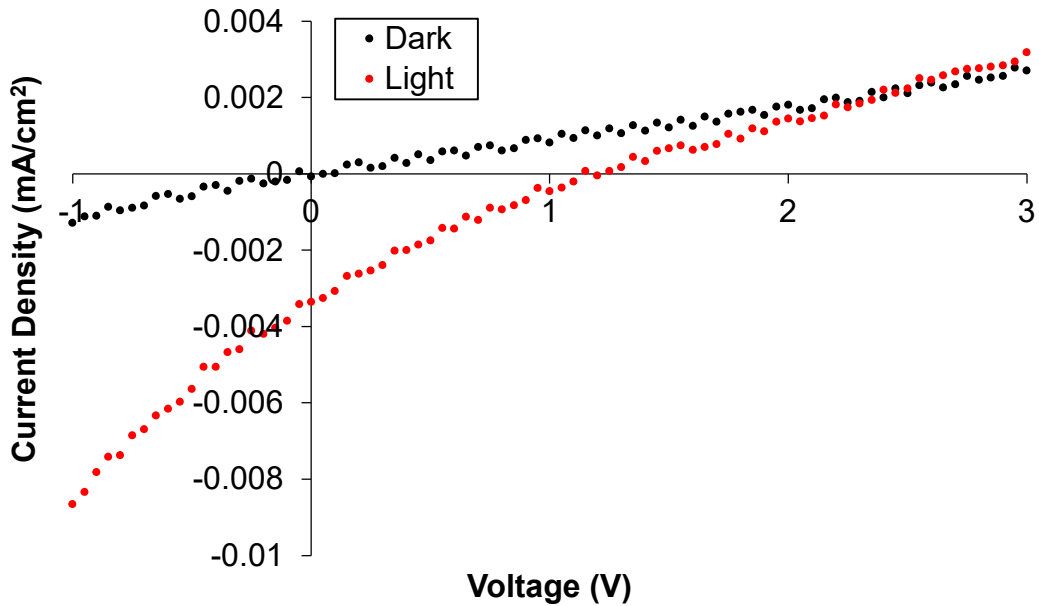


Figure 52: Generation three CdTe heterostructure. Most J-V characteristics for generation three devices measured short circuits and many other failed into an open circuit upon illuminated J-V measurement. However, despite a large R_s this generation three CdTe heterostructure exhibited a largest V_{OC} but a small J_{SC} under 0.605 sun illumination.

5.3.2 Layer transferred GaAs Device J-V Characteristics

The proposed structure for the demonstration of a layer transferred GaAs device, seen in Figure 43a, was originally deposited by MBE, as outlined in subsection 5.2.3, on both sapphire and spinel substrates. Roughening, and clouding of the InGaP and subsequent GaAs p-type contacting layer due to a loss of phosphorus during growth led to an attempt to salvage the devices first using a selective wet chemical etch. Unlike the GaAs/sapphire samples, which had exhibited a unique weak interfacial adhesion like the CdTe/sapphire system, the strain in GaAs/spinel system caused bowing and subsequent delamination during

wet chemical etching. This exposed and undercut the active GaAs device dissolving it entirely.

The remaining GaAs/sapphire samples were processed into salvaged devices as described in subsection 5.2.3. Like the CdTe heterostructures, the predicted chemical composition, doping and thickness of the secondary layers applied by PLD, may not reflect the actual device structure fabricated. Despite these challenges, the first attempt at layer transferred GaAs devices did all exhibit some photoactivity during illuminated J-V measurement.

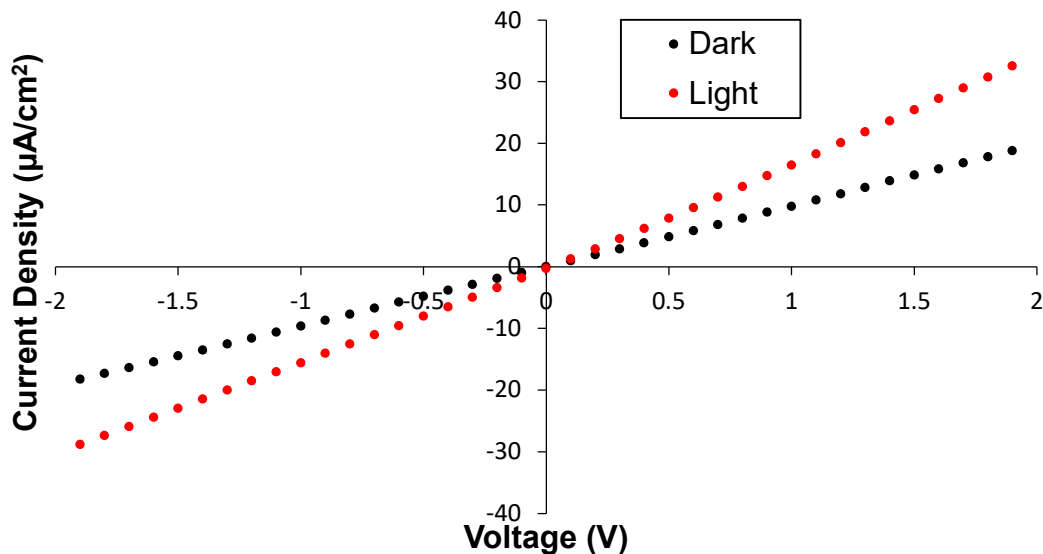


Figure 53: GaAs Device A, photoresistor. J-V characteristics for one of the three GaAs devices which exhibited no photocurrent shift into the fourth quadrant. Instead the device acts as a photoresistor, with device's photoconductivity increasing with increased irradiance from the dark measurement.

Some devices were observed to be photoresistors, see Figure 53, like the early generation one CdTe heterostructures. Unlike the CdTe

photoresistor devices, however, these GaAs photoresistors exhibited no measurable photocurrent. Other layer transferred GaAs devices demonstrated a weak photovoltaic response, see Figure 54, with a V_{OC} of 205 mV but low photocurrent, having a J_{SC} of $0.28 \mu\text{A}/\text{cm}^2$. While this device had a reasonable R_{sh} of $1038 \text{ k}\Omega\cdot\text{cm}^2$, it suffered from large R_s of $551.1 \text{ k}\Omega\cdot\text{cm}^2$.

The s-shape of the J-V curve is also indicative of a non-ohmic contact to the device, such as a Schottky contact.^[159] This is likely the result of not following a contact annealing procedure for the p- or n-type contacts,^[160] and should have been considered in the device fabrication process.

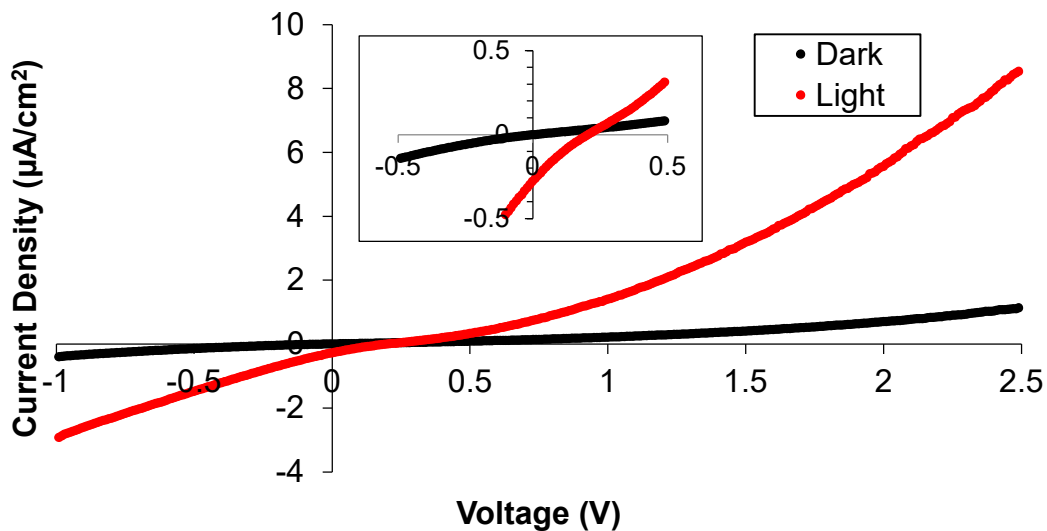


Figure 54: GaAs Device B, small photovoltaic response. J-V characteristics for one of the two GaAs devices exhibiting weak photovoltaic activity. Inset graph shows a photocurrent shifts the light J-V curve into the fourth quadrant with respect to the dark curve, indicating work output by the device when illuminated.

The layer transferred GaAs device with the highest photovoltaic performance had a V_{OC} of 240 mV and a J_{SC} of $0.72 \mu\text{A}/\text{cm}^2$. Although it too suffered from apparent non-ohmic contacts. Other factors which may have influenced the high R_s measured is the effective doping of the ZnTe:N hole contacting layer, as well as the barrier height and thickness of the ZnSe rear passivation. Although ZnSe layers and sulfur are effective surface passivation methods for GaAs,^[161] these samples represent the first attempt at deposition of a ZnSe layer by PLD. In hindsight, a ~ 10 nm ZnSe barrier width is expected to impede carrier collection efficiency given its wide bandgap of 2.70 eV.

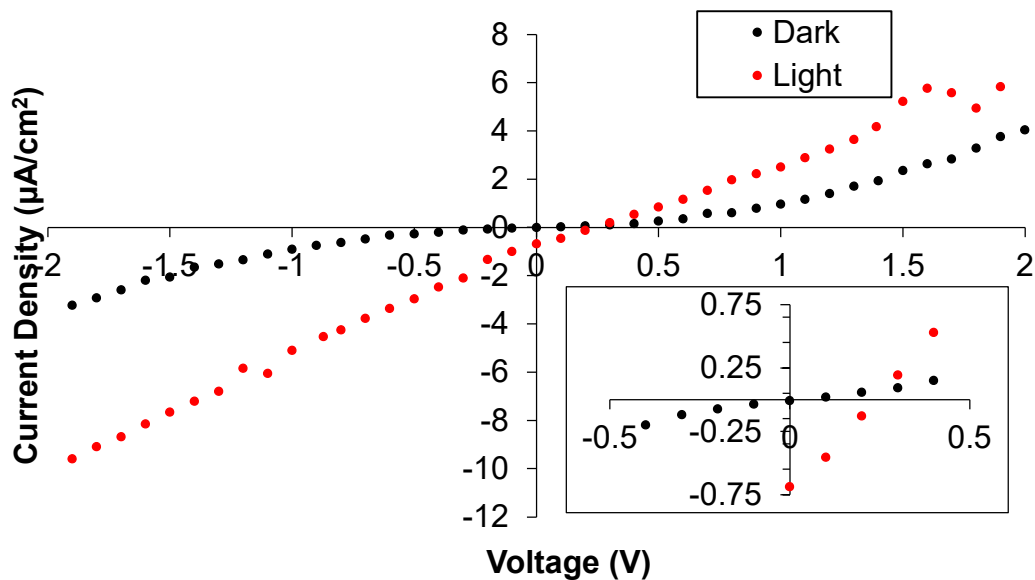


Figure 55: GaAs Device C, largest V_{OC} . J-V characteristics for the highest performing of the two GaAs devices exhibiting weak photovoltaic activity. Inset graph shows more than twice the photocurrent generated and larger open circuit voltage compared to the other GaAs device with PV behaviour. Both device behaviours appear dominated by a series resistance.

5.4 Conclusions

A summary of the three generations of device performances is given in Figure 56. Although, the highest performing device was only 0.0453%, the two-side processing of a flexible layer transferred CdTe double heterostructure was demonstrated. These experiments are a validation of MELO and its ability to offer a route to produce high quality flexible and large area devices for material systems not currently available by conventional processing techniques.

Further refinement and study of the fabrication process is required to decrease process variability between the predicted and deposited structures. Also, a cross-sectional analysis of the chemical composition of these structures may reveal the actual thicknesses, compositions, and the spatial sharpness of the heterointerfaces. While carrier extraction efficiency was low leading to large R_s and low J_{sc} it is encouraging for the preliminary study to measure consistently large V_{oc} indicating good absorber quality and surface passivation.

	V_{oc} (mV)	J_{sc} (mA/cm ²)	FF (%)	μ (%)	R_{sh} (k Ω ·cm ²)	R_s (k Ω ·cm ²)
Gen 1	1.85	0.106	25.1	0.000049	0.0174	0.0174
Gen 2_A	291.1	0.00163	32.0	0.000152	82.4	174.2
Gen 2_B	397.9	0.00009	26.5	0.00000949	7294	14501
Gen 2_C	551.7	0.173	28.7	0.0453	3.76	1.99
Gen 3	1186	0.00336	21.9	0.00145	292.9	488.2

Figure 56: Table summary of CdTe heterostructure PV characteristics. Subscripts _A, _B and _C denote the PV characteristics of three working pads on the generation 2 device with different behaviours.

A performance summary of the first attempt at layer transferred GaAs devices from sapphire is in Figure 57. Like their layer transferred CdTe heterostructure counterparts, they suffer from very high R_s , due to poor charge collection efficiency and apparent non-ohmic metal contacts. Despite the shortcomings and challenges of these preliminary devices, they do demonstrate the proof-of-concept of a GaAs layer transferred device from sapphire. The measured V_{oc} of 240 mV for a first attempt using salvaged thin films is also promising, that like the CdTe devices, further process and design refinements may yield dramatic improvements in the layer transferred device performance.

	V_{oc} (mV)	J_{sc} ($\mu A/cm^2$)	FF (%)	μ (%)	R_{sh} ($k\Omega \cdot cm^2$)	R_s ($k\Omega \cdot cm^2$)
Device A	--	--	--	--	--	102.6 _D
						62.1 _L
Device B	205	0.28	20.9	0.000012	1038	551.2
Device C	240	0.72	26.3	0.000045	307.4	338.4

Figure 57: Table summary of GaAs PV characteristics. Subscripts _D and _L are used to denote dark and illuminated photoresistance, respectively.

6 Conclusions and Future Work

6.1 Contribution Summary

The direct observation of a heteroepitaxial system, CdTe (111)/ α -Al₂O₃ (0001), which relaxes strain at the interface due to weak van der Waals-like bonding between the thin film and bulk substrate instead of via misfit dislocation despite a large lattice mismatch, is a major scientific discovery. As a result, this compliant interface produces a high quality CdTe film, comparable to or even exceeding its bulk crystal counterpart. It has been determined that weak bonding occurs spontaneously for the system during the growth process by the self-assembly of tellurium adatoms into a pseudomorphic monolayer on the surface of sapphire. The discovery of this type of interface, which spontaneously allows for a 3D/3D van der Waals heteroepitaxial system, supports the possibility that these interface types may exist in other heteroepitaxial systems on complex oxide and chalcogen terminated surfaces.

The transfer of 2D materials onto substrates has recently received tremendous attention as a mechanism to improve the quality of and allow for the integration of heteroepitaxial systems by overcoming the lattice matching requirement using a remote epitaxy mechanism. As a benefit, the resulting weak film/substrate adhesion, due to the van der Waals interactions with the 2D interlayer, allows for the transfer of films from their

growth substrate, by mechanical exfoliation with a tensile layer, to create a variety of novel heterostructures and even flexible devices not possible by conventional techniques. However, technological limitations to produce large area 2D pristine layers, have prevented the scaling of these techniques to wafer scale devices.

A direct heteroepitaxial growth pathway represents an alternative method to achieve a compliant heteroepitaxial interface, without the technological limitations of transferring 2D materials, since the weak bonding interface forms spontaneously in-situ during the deposition and heteroepitaxy is easily scalable to the wafer scale. Further, study of the mechanical epitaxial lift off and handling of these CdTe films and heterostructures layer transferred to a PSU carrier in this work demonstrate that the creation of such novel flexible devices is also possible by this technique. Successful large and patterned area polymer layer transfer, however, is shown to be strongly dependant on achieving uniform biaxial tension and strong polymer/metal adhesion to the semiconductor film. Such successfully transferred layers have also been demonstrated to retain their optical and structural quality leaving the original growth substrate for future reuse.

These MELO techniques were also used to demonstrate a successful proof of concept for a two-side processed layer transferred CdTe heterostructure photovoltaic device, validating its potential ability to

offer a route to produce high quality flexible and large area devices for material systems not currently available by conventional processing techniques. While overall efficiency of these devices was low due to high series impedance, likely caused by poor charge carrier collection efficiency, the measured high open circuit voltages illustrate the long bulk carrier lifetime and good surface passivation of the CdTe absorber layer. As such, future refinement of the fabrication process and heterostructure design is likely to yield improved device performance.

Following a growth study of GaAs on oxide substrates and the knowledge transfer of the MELO method to another material, the same phenomena of epitaxial registry but apparent weak interfacial adhesion was demonstrated for another system, GaAs (111)/ α -Al₂O₃ (0001). Despite low efficiency, like their CdTe heterostructure counterparts, preliminary development of layer transferred GaAs structures demonstrate a proof of concept for these types of devices, warranting future study to improve their quality.

Compliant interfaces with weak adhesion, identified in this work, represent a means to produce novel devices from materials not currently available in large areas due to a lack of bulk substrates. Further, interface layers generated by this technique may be used to create compliant substrates for additional heteroepitaxy. Utilizing layer transfer techniques in combination, they allow for the monolithic integration of unconventional

materials for advanced electronics and photonics, as well as the development of novel two-sided processed flexible thin film devices.

6.2 Future Work

6.2.1 Process Improvements for Layer Transferred Devices

The MELO process window with a tensile polymer transfer layer has demonstrated support of a wide range of structure thicknesses and tensile strains. Major improvements to this process could be made by scaling it up to films deposited on full sized wafers, using a deposition technique more suitable for the uniform deposition of large areas, as well as automating the lamination processing to support the handling of thinner thermoplastic transfer layers. Additionally, the study of new polymer and even metallic tensile transfer layers may provide additional opportunities to create free standing thin devices or monolithically integrate transferred thin films with traditional substrates, such as silicon.

Specifically, for the continued refinement of two-side processed CdTe films and heterostructures, improvements to the PLD deposition system available or transfer of the deposition process to a different growth technique is required to improve thickness and composition uniformity over large areas. Regardless of the growth process, in-situ characterization such as reflection high-energy diffraction or a calibrated crystal thickness monitor would provide additional real-time information

about the growth. Pairing such additional growth information with cross-sectional or depth profiling chemical composition analysis, time resolved photoluminescence and external quantum efficiency measurements will support improvements to the device performance characteristics, as well as the ability to develop more accurate modeling of the devices under test.

Further interfacial study could also be considered by plan view sample preparation for STEM and EELS study. Complimentary measurements may reveal more information about the nature of weak bonding at the interface such as the influence of topological variation on the surface of the substrate and the nature of in- and out-of-plane plasmon modes at the interface. Additionally, temperature dependant and time-resolved PL spectroscopy of transferred freestanding and on-sapphire CdTe films and structures may be considered to further investigate radiative and non-radiative transitions in the system, including the broadening mechanisms.

6.2.2 Refinement of GaAs (111)/ α -Al₂O₃ (0001) and Interfacial Study

The unique epitaxial registry with apparent weak interfacial adhesion demonstrated for GaAs (111)/ α -Al₂O₃ (0001) may be due to a type of compliant interface similar to that observed in the CdTe (111)/ α -Al₂O₃ (0001) system. A detailed STEM cross-sectional analysis would reveal the mechanism of compliance for the relatively relaxed, but highly epitaxial,

GaAs films provided the interface can be protected during lift-out. Given the reduction of twins and improved film quality of GaAs on sapphire in literature by various techniques, adapting such techniques may lead to the refinement of the thin film MBE deposition process for improved quality. Layer transferred GaAs films from α -Al₂O₃ substrates have a multitude of applications to explore, including the monolithic integration of GaAs devices on silicon platforms by layer transfer and bonding.

6.2.3 Compliant Chalcogen Interlayers for Other Material Systems

The demonstration of the direct 3D on 3D van der Waals heteroepitaxy by the in-situ formation of a chalcogen monolayer has direct application for the development of compliant substrates for additional heteroepitaxy for exotic materials, limited normally by the availability of lattice matched bulk wafer substrates. Since the CdTe depositions on sapphire can be patterned and formation of a vdW-like interface between the semiconductor and oxide is spontaneous, these interfaces may also direct application for forming non-perturbing vdW contacts for oxide electronics worth investigating. Another area of research for these types of interfaces is the intentional chalcogen passivation of a wafer surface followed by subsequent homo- or heteroepitaxial deposition. Chalcogen passivated 3D substrates have been demonstrated in literature to support the epitaxy of subsequent 2D layers. However, conditions may exist where

a passivated interface with a chalcogenide-chalcogenide vdW bond, such as GaAs-GaTe-GaTe-GaAs, may demonstrate epitaxial registry with weak adhesion. This was attempted previously at the MBE facilities at McMaster, but that system lacks a Te source with sufficient flux. The MOCVD system, however, may be more suited for this experimental study.

7 References

- [1] R. N. Thomas, H. M. Hobgood, P. S. Ravishankar, T. T. Braggins, *Journal of Crystal Growth* **1990**, *99*, 643.
- [2] M. D. Pavlyuk, I. A. Subbotin, V. M. Kanevsky, V. V. Artemov, *Journal of Crystal Growth* **2017**, *457*, 112.
- [3] S. Montanari, “III-V compound semiconductor material systems,” can be found under http://web.tiscali.it/decartes/phd_html/node4.html, **2005**.
- [4] K. J. Yu, Z. Yan, M. Han, J. A. Rogers, *npj Flexible Electronics* **2017**, *1*, 1.
- [5] A. Polman, H. A. Atwater, *Nature Materials* **2012**, *11*, 174.
- [6] H. Kum, D. Lee, W. Kong, H. Kim, Y. Park, Y. Kim, Y. Baek, S.-H. Bae, K. Lee, J. Kim, *Nature Electronics* **2019**, *2*, 439.
- [7] P. Rudolph, Ed. , *Handbook of Crystal Growth*, Elsevier, **2015**.
- [8] M. Dutta, M. A. Stroschio, *Advanced Semiconductor Heterostructures: Novel Devices, Potential Device Applications and Basic Properties*, WORLD SCIENTIFIC, **2003**.
- [9] J. Narayan, B. C. Larson, *Journal of Applied Physics* **2002**, *93*, 278.
- [10] J. C. Bean, T. T. Sheng, L. C. Feldman, A. T. Fiory, R. T. Lynch, *Appl. Phys. Lett.* **1984**, *44*, 102.
- [11] J. R. Arthur, *Surface Science* **2002**, *500*, 189.
- [12] J. W. Matthews, A. E. Blakeslee, *Journal of Crystal Growth* **1974**, *27*, 118.
- [13] J. Massies, N. Grandjean, *Phys. Rev. Lett.* **1993**, *71*, 1411.
- [14] R. Sharma, A. K. Rana, in *2015 IEEE 2nd International Conference on Recent Trends in Information Systems (ReTIS)*, **2015**, pp. 475–480.
- [15] A. Nainani, D. Kim, T. Krishnamohan, K. Saraswat, in *2009 International Conference on Simulation of Semiconductor Processes and Devices*, **2009**, pp. 1–4.
- [16] C. Kittel, *Introduction to Solid State Physics*, John Wiley & Sons, Inc., **2004**.
- [17] M. Reiche, M. Kittler, H. Uebensee, E. Pippel, A. Haehnel, S. Birner, *Appl. Phys. A* **2016**, *122*, 389.
- [18] Z. Suo, J. W. Hutchinson, *International Journal of Solids and Structures* **1989**, *25*, 1337.
- [19] M. D. Thouless, A. G. Evans, M. F. Ashby, J. W. Hutchinson, *Acta Metallurgica* **1987**, *35*, 1333.
- [20] M. Ohring, *Materials Science of Thin Films*, Elsevier, **2002**.
- [21] J. A. Venables, G. D. T. Spiller, in *Surface Mobilities on Solid Materials: Fundamental Concepts and Applications* (Ed.: V.T. Binh), Springer US, Boston, MA, **1983**, pp. 341–404.
- [22] K. Reichelt, *Vacuum* **1988**, *38*, 1083.
- [23] C. -h. Chiu, Z. Huang, C. T. Poh, *Phys. Rev. Lett.* **2004**, *93*, 136105.

- [24] R. People, J. C. Bean, *Appl. Phys. Lett.* **1985**, *47*, 322.
- [25] P. J. Orders, B. F. Usher, *Appl. Phys. Lett.* **1987**, *50*, 980.
- [26] J. Narayan, *Acta Materialia* **2013**, *61*, 2703.
- [27] D. E. Grider, S. E. Swirhun, D. H. Narum, A. I. Akinwande, T. E. Nohava, W. R. Stuart, P. Joslyn, K. C. Hsieh, *Journal of Vacuum Science & Technology B: Microelectronics Processing and Phenomena* **1990**, *8*, 301.
- [28] K. Eisenbeiser, R. Emrick, R. Droopad, Z. Yu, J. Finder, S. Rockwell, J. Holmes, C. Overgaard, W. Ooms, *IEEE Electron Device Letters* **2002**, *23*, 300.
- [29] P. O. Hansson, A. Gustafsson, M. Albrecht, R. Bergmann, H. P. Strunk, E. Bauser, *Journal of Crystal Growth* **1992**, *121*, 790.
- [30] A. Koma, K. Sunouchi, T. Miyajima, *Journal of Vacuum Science & Technology B: Microelectronics Processing and Phenomena* **1985**, *3*, 724.
- [31] A. K. Geim, I. V. Grigorieva, *Nature* **2013**, *499*, 419.
- [32] A. Koma, *Thin Solid Films* **1992**, *216*, 72.
- [33] J.-Y. Hwang, Y.-M. Kim, K. H. Lee, H. Ohta, S. W. Kim, *Nano Lett.* **2017**, *17*, 6140.
- [34] L. A. Walsh, C. L. Hinkle, *Applied Materials Today* **2017**, *9*, 504.
- [35] Y. Kim, S. S. Cruz, K. Lee, B. O. Alawode, C. Choi, Y. Song, J. M. Johnson, C. Heidelberger, W. Kong, S. Choi, K. Qiao, I. Almansouri, E. A. Fitzgerald, J. Kong, A. M. Kolpak, J. Hwang, J. Kim, *Nature* **2017**, *544*, 340.
- [36] W. Kong, H. Li, K. Qiao, Y. Kim, K. Lee, Y. Nie, D. Lee, T. Osadchy, R. J. Molnar, D. K. Gaskill, R. L. Myers-Ward, K. M. Daniels, Y. Zhang, S. Sundram, Y. Yu, S. Bae, S. Rajan, Y. Shao-Horn, K. Cho, A. Ougazzaden, J. C. Grossman, J. Kim, *Nature Mater* **2018**, *17*, 999.
- [37] J. Kang, D. Shin, S. Bae, B. H. Hong, *Nanoscale* **2012**, *4*, 5527.
- [38] K. S. Kim, Y. Zhao, H. Jang, S. Y. Lee, J. M. Kim, K. S. Kim, J.-H. Ahn, P. Kim, J.-Y. Choi, B. H. Hong, *Nature* **2009**, *457*, 706.
- [39] S. Pillet, M. Souhassou, C. Lecomte, K. Schwarz, P. Blaha, M. Rérat, A. Lichanot, P. Roversi, *Acta Crystallographica Section A* **2001**, *57*, 290.
- [40] R. A. Johnson, P. R. de la Houssaye, C. E. Chang, Pin-Fan Chen, M. E. Wood, G. A. Garcia, I. Lagnado, P. M. Asbeck, *IEEE Transactions on Electron Devices* **1998**, *45*, 1047.
- [41] M. E. Thomas, W. J. Tropf, S. L. Gilbert, *OE* **1993**, *32*, 1340.
- [42] D. S. Peng, Y. C. Feng, W. X. Wang, X. F. Liu, W. Shi, H. B. Niu, *J. Phys. D: Appl. Phys.* **2007**, *40*, 1108.
- [43] R. Müller, F. Huber, M. Töws, M. Mangold, M. Madel, J.-P. Scholz, A. Minkow, U. Herr, K. Thonke, *Crystal Growth & Design* **2020**, *20*, 3918.
- [44] S. Neretina, Q. Zhang, R. A. Hughes, J. F. Britten, N. V. Sochinskii, J. S. Preston, P. Mascher, *Journal of Elec Materi* **2006**, *35*, 1224.
- [45] G. Yu, G. Wang, H. Ishikawa, M. Umeno, T. Soga, T. Egawa, J. Watanabe, T. Jimbo, *Appl. Phys. Lett.* **1997**, *70*, 3209.

- [46] Ü. Özgür, V. Avrutin, H. Morkoç, in *Molecular Beam Epitaxy* (Ed.: M. Henini), Elsevier, **2018**, pp. 343–375.
- [47] F. A. Ponce, J. Aranovich, *Appl. Phys. Lett.* **1981**, *38*, 439.
- [48] Y. Chun, L. Yan-rong, L. Jin-shan, *Phys. Rev. B* **2004**, *70*, 045413.
- [49] N. Grandjean, J. Massies, Y. Martinez, P. Vennéguès, M. Leroux, M. Laügt, *Journal of Crystal Growth* **1997**, *178*, 220.
- [50] K. Dovidenko, S. Oktyabrsky, A. K. Sharma, J. Narayan, *MRS Online Proceedings Library Archive* **1998**, *526*, DOI 10.1557/PROC-526-311.
- [51] K. H. Johnson, S. V. Pepper, *Journal of Applied Physics* **1982**, *53*, 6634.
- [52] H. Li, W. Zhang, J. R. Smith, *physica status solidi (a)* **2011**, *208*, 1166.
- [53] K. Meinander, J. S. Preston, *Surface Science* **2015**, *632*, 93.
- [54] C. B. Duke, *Chem. Rev.* **1996**, *96*, 1237.
- [55] J. Dąbrowski, H.-J. Müssig, *Silicon Surfaces and Formation of Interfaces: Basic Science in the Industrial World*, World Scientific, **2000**.
- [56] M. D. Pashley, K. W. Haberern, in *Semiconductor Interfaces at the Sub-Nanometer Scale* (Eds.: H.W.M. Salemink, M.D. Pashley), Springer Netherlands, Dordrecht, **1993**, pp. 63–73.
- [57] C. C. Chang, *Journal of Applied Physics* **1968**, *39*, 5570.
- [58] T. J. Godin, J. P. LaFemina, *Phys. Rev. B* **1994**, *49*, 7691.
- [59] M. Yoshimoto, T. Maeda, T. Ohnishi, H. Koinuma, O. Ishiyama, M. Shinohara, M. Kubo, R. Miura, A. Miyamoto, *Appl. Phys. Lett.* **1995**, *67*, 2615.
- [60] H. Kroemer, *Journal of Crystal Growth* **1987**, *81*, 193.
- [61] S. M. Jovanovic, H. M. El-Sherif, N. D. Bassim, J. S. Preston, *Small* **n.d.**, *16*, 2004437.
- [62] S. M. Jovanovic, G. A. Devenyi, P. Kuyanov, J. L. Carvalho, K. Meinander, R. R. LaPierre, J. S. Preston, *Mater. Res. Express* **2018**, *6*, 025913.
- [63] J. E. Ayers, *Journal of Elec Materi* **2008**, *37*, 1511.
- [64] Z. Y. Al Balushi, T. Miyagi, Y.-C. Lin, K. Wang, L. Calderin, G. Bhimanapati, J. M. Redwing, J. A. Robinson, *Surface Science* **2015**, *634*, 81.
- [65] S. Z. Butler, S. M. Hollen, L. Cao, Y. Cui, J. A. Gupta, H. R. Gutiérrez, T. F. Heinz, S. S. Hong, J. Huang, A. F. Ismach, E. Johnston-Halperin, M. Kuno, V. V. Plashnitsa, R. D. Robinson, R. S. Ruoff, S. Salahuddin, J. Shan, L. Shi, M. G. Spencer, M. Terrones, W. Windl, J. E. Goldberger, *ACS Nano* **2013**, *7*, 2898.
- [66] C.-J. Shih, M. S. Strano, D. Blankschtein, *Nature Materials* **2013**, *12*, 866.
- [67] S.-H. Bae, K. Lu, Y. Han, S. Kim, K. Qiao, C. Choi, Y. Nie, H. Kim, H. S. Kum, P. Chen, W. Kong, B.-S. Kang, C. Kim, J. Lee, Y. Baek, J. Shim, J. Park, M. Joo, D. A. Muller, K. Lee, J. Kim, *Nat. Nanotechnol.* **2020**, *1*.
- [68] D. B. Chrisey, G. K. Hübner, *Pulsed Laser Deposition of Thin Films*, Wiley, **1994**.
- [69] R. Reichelt, in *Science of Microscopy* (Eds.: P.W. Hawkes, J.C.H. Spence), Springer, New York, NY, **2007**, pp. 133–272.

- [70] G. Zhu, High-Resolution Characterization of Low-Dimensional Defects in SrTiO₃, thesis, **2012**.
- [71] B. B. He, *Two-Dimensional X-Ray Diffraction*, John Wiley & Sons, Incorporated, Hoboken, UNITED STATES, **2009**.
- [72] S. T. Edwards, A. F. Schreiner, T. M. Myers, J. F. Schetzina, *Journal of Applied Physics* **1983**, *54*, 6785.
- [73] S. M. Jovanovic, G. A. Devenyi, V. M. Jarvis, K. Meinander, C. M. Haapamaki, P. Kuyanov, M. Gerber, R. R. LaPierre, J. S. Preston, *Thin Solid Films* **2014**, *570*, 155.
- [74] M. Kh. Rabadanov, I. A. Verin, Yu. M. Ivanov, V. I. Simonov, *Crystallogr. Rep.* **2001**, *46*, 636.
- [75] I. Dima, D. Borşan, *physica status solidi (b)* **1967**, *23*, K113.
- [76] S.-H. Wei, S. B. Zhang, *Phys. Rev. B* **2000**, *62*, 6944.
- [77] B. Hinnemann, E. A. Carter, *J. Phys. Chem. C* **2007**, *111*, 7105.
- [78] L. S. Brooks, *J. Am. Chem. Soc.* **1952**, *74*, 227.
- [79] A. C. Egerton, F. V. Raleigh, *J. Chem. Soc., Trans.* **1923**, *123*, 3024.
- [80] R. Cavallotti, J. Goniakowski, R. Lazzari, J. Jupille, A. Koltsov, D. Loison, *J. Phys. Chem. C* **2014**, *118*, 13578.
- [81] D. Mohanty, W. Xie, Y. Wang, Z. Lu, J. Shi, S. Zhang, G.-C. Wang, T.-M. Lu, I. B. Bhat, *Appl. Phys. Lett.* **2016**, *109*, 143109.
- [82] D. Mohanty, Z. Lu, X. Sun, Y. Xiang, Y. Wang, D. Ghoshal, J. Shi, L. Gao, S. Shi, M. Washington, G.-C. Wang, T.-M. Lu, I. Bhat, *Phys. Rev. Materials* **2018**, *2*, 113402.
- [83] Y. Du, G. Qiu, Y. Wang, M. Si, X. Xu, W. Wu, P. D. Ye, *Nano Lett.* **2017**, *17*, 3965.
- [84] G. J. Shu, S. C. Liou, S. K. Karna, R. Sankar, M. Hayashi, F. C. Chou, *Phys. Rev. Materials* **2018**, *2*, 044201.
- [85] Y. H. Ichikawa, *Phys. Rev.* **1958**, *109*, 653.
- [86] G. Kästner, U. Gösele, *Journal of Applied Physics* **2000**, *88*, 4048.
- [87] Y. Alaskar, S. Arafin, D. Wickramaratne, M. A. Zurbuchen, L. He, J. McKay, Q. Lin, M. S. Goorsky, R. K. Lake, K. L. Wang, *Advanced Functional Materials* **2014**, *24*, 6629.
- [88] G. Dhanaraj, K. Byrappa, V. (Vish) Prasad, M. Dudley, in *Springer Handbook of Crystal Growth* (Eds.: G. Dhanaraj, K. Byrappa, V. Prasad, M. Dudley), Springer Berlin Heidelberg, Berlin, Heidelberg, **2010**, pp. 3–16.
- [89] H.-S. Lee, J. Suk, H. Kim, J. Kim, J. Song, D. S. Jeong, J.-K. Park, W. M. Kim, D.-K. Lee, K. J. Choi, B.-K. Ju, T. S. Lee, I. Kim, *Scientific Reports* **2018**, *8*, 3504.
- [90] G. P. Willeke, *Solar Energy Materials and Solar Cells* **2002**, *72*, 191.
- [91] E. Yablonovitch, T. Gmitter, J. P. Harbison, R. Bhat, *Applied Physics Letters* **1987**, *51*, 2222.

- [92] C.-W. Cheng, K.-T. Shiu, N. Li, S.-J. Han, L. Shi, D. K. Sadana, *Nature Communications* **2013**, *4*, 1577.
- [93] D.-M. Geum, M.-S. Park, J. Y. Lim, H.-D. Yang, J. D. Song, C. Z. Kim, E. Yoon, S. Kim, W. J. Choi, *Scientific Reports* **2016**, *6*, 20610.
- [94] C.-H. Cheng, A.-J. Tzou, J.-H. Chang, Y.-C. Chi, Y.-H. Lin, M.-H. Shih, C.-K. Lee, C.-I. Wu, H.-C. Kuo, C.-Y. Chang, G.-R. Lin, *Scientific Reports* **2016**, *6*, 19757.
- [95] S. W. Bedell, K. Fogel, P. Lauro, D. Shahrjerdi, J. A. Ott, D. Sadana, *J. Phys. D: Appl. Phys.* **2013**, *46*, 152002.
- [96] M. Bruel, *Nuclear Instruments and Methods in Physics Research Section B: Beam Interactions with Materials and Atoms* **1996**, *108*, 313.
- [97] M. Bruel, B. Aspar, A.-J. Auberton-Hervé, *Jpn. J. Appl. Phys.* **1997**, *36*, 1636.
- [98] J. Kim, C. Bayram, H. Park, C.-W. Cheng, C. Dimitrakopoulos, J. A. Ott, K. B. Reuter, S. W. Bedell, D. K. Sadana, *Nature Communications* **2014**, *5*, 4836.
- [99] M. A. Islam, J. H. Kim, A. Schropp, H. Kalita, N. Choudhary, D. Weitzman, S. I. Khondaker, K. H. Oh, T. Roy, H.-S. Chung, Y. Jung, *Nano Lett.* **2017**, *17*, 6157.
- [100] M. Stadermann, S. H. Baxamusa, C. Aracne-Ruddle, M. Chea, S. Li, K. Youngblood, T. Suratwala, *J Vis Exp* **2015**, DOI 10.3791/52832.
- [101] S. H. Baxamusa, M. Stadermann, C. Aracne-Ruddle, A. J. Nelson, M. Chea, S. Li, K. Youngblood, T. I. Suratwala, *Langmuir* **2014**, *30*, 5126.
- [102] J. W. Hutchinson, Z. Suo, in *Advances in Applied Mechanics* (Eds.: J.W. Hutchinson, T.Y. Wu), Elsevier, **1991**, pp. 63–191.
- [103] A. G. Evans, J. W. Hutchinson, *International Journal of Solids and Structures* **1984**, *20*, 455.
- [104] M. F. Gruninger, B. R. Lawn, E. N. Farabaugh, J. B. Wachtman, *Journal of the American Ceramic Society* **1987**, *70*, 344.
- [105] B. Lawn, *Fracture of Brittle Solids*, Cambridge University Press, Cambridge, **1993**.
- [106] A. M. Kelley, A. M. Kelley, *Condensed-Phase Molecular Spectroscopy and Photophysics*, John Wiley & Sons, Incorporated, Somerset, UNITED STATES, **2012**.
- [107] G. Brammertz, Y. Mols, S. Degroote, V. Motsnyi, M. Leys, G. Borghs, M. Caymax, *Journal of Applied Physics* **2006**, *99*, 093514.
- [108] B. Sarıkavak, M. K. Öztürk, T. S. Mammadov, S. Özçelik, *Crystal Research and Technology* **2010**, *45*, 517.
- [109] X. Zhu, N. R. Monahan, Z. Gong, H. Zhu, K. W. Williams, C. A. Nelson, *J. Am. Chem. Soc.* **2015**, *137*, 8313.
- [110] T. G. Mack, L. Jethi, P. Kambhampati, *J. Phys. Chem. C* **2017**, *121*, 28537.

- [111] X. Zhao, S. Liu, C. M. Campbell, Y. Zhao, M. B. Lassise, Y. Zhang, in *2016 IEEE 43rd Photovoltaic Specialists Conference (PVSC)*, **2016**, pp. 2302–2305.
- [112] S. M. Jovanovic, Pulsed Laser Heteroepitaxy of High Quality CdTe Thin Films on Sapphire Substrates, thesis, **2013**.
- [113] R. Balasubramanian, W. R. Wilcox, *Materials Science and Engineering: B* **1993**, *16*, 1.
- [114] J. Brandrup, E. H. Immergut, E. A. Grulke, A. Abe, D. R. Bloch, *Polymer Handbook*, John Wiley & Sons, **1999**.
- [115] N. Li, S. Bedell, H. Hu, S.-J. Han, X. H. Liu, K. Saenger, D. Sadana, *Adv. Mater.* **2017**, *29*, DOI 10.1002/adma.201606638.
- [116] S. W. Bedell, P. Lauro, J. A. Ott, K. Fogel, D. K. Sadana, *Journal of Applied Physics* **2017**, *122*, 025103.
- [117] R. Martini, M. Gonzalez, F. Dross, A. Masolin, J. Vaes, D. Frederickx, J. Poortmans, *Energy Procedia* **2012**, *27*, 567.
- [118] W. S. Leong, H. Wang, J. Yeo, F. J. Martin-Martinez, A. Zubair, P.-C. Shen, Y. Mao, T. Palacios, M. J. Buehler, J.-Y. Hong, J. Kong, *Nat Commun* **2019**, *10*, DOI 10.1038/s41467-019-08813-x.
- [119] J. A. Thornton, D. W. Hoffman, *Journal of Vacuum Science and Technology* **1977**, *14*, 164.
- [120] I. Rose, C. Whittington, *Nickel Plating Handbook*, Nickel Institute, Russel, Belgium, **2014**.
- [121] M. Iwasa, T. Ueno, R. C. Bradt, *Journal of the Society of Materials Science, Japan* **1981**, *30*, 1001.
- [122] H. S. Cole, H. H. Woodbury, J. F. Schetzina, *Journal of Applied Physics* **1984**, *55*, 3166.
- [123] R. N. Bicknell, T. H. Myers, J. F. Schetzina, *Journal of Vacuum Science & Technology A* **1984**, *2*, 423.
- [124] T. H. Myers, Y. Lo, R. N. Bicknell, J. F. Schetzina, *Appl. Phys. Lett.* **1983**, *42*, 247.
- [125] N. C. Giles-Taylor, R. N. Bicknell, D. K. Blanks, T. H. Myers, J. F. Schetzina, *Journal of Vacuum Science & Technology A* **1985**, *3*, 76.
- [126] K. Kasai, K. Nakai, M. Ozeki, *Journal of Applied Physics* **1986**, *60*, 1.
- [127] A. Sugimura, T. Hosoi, K. Ishibitsu, T. Kawamura, *Journal of Crystal Growth* **1986**, *77*, 524.
- [128] A. C. Diebold, S. W. Steinhauser, R. P. Mariella, J. Marti, F. Reidinger, R. F. Antrim, *Surface and Interface Analysis* **1990**, *15*, 150.
- [129] I. Ladany, C. C. Wang, *Journal of Applied Physics* **1972**, *43*, 236.
- [130] C.-C. Wang, F. C. Dougherty, M. T. Duffy, I. Ladany, S. H. McFarlane, *Epitaxial Growth and Characterization of GaAs on Spinel.*, RCA LABS PRINCETON NJ, **1972**.

- [131] J. R. Arthur, J. J. LePore, *Journal of Vacuum Science and Technology* **1969**, *6*, 545.
- [132] A. Y. Cho, J. R. Arthur, *Progress in Solid State Chemistry* **1975**, *10*, 157.
- [133] S. Neretina, The Deposition of Cadmium Telluride Using Exotic Growth Pathways, McMaster University, **2007**.
- [134] S. K. Saha, R. Kumar, A. Kuchuk, M. Z. Alavijeh, Y. Maidaniuk, Y. I. Mazur, S.-Q. Yu, G. J. Salamo, *Crystal Growth & Design* **2019**, *19*, 5088.
- [135] D. R. Crouse, Controlled Spalling in (100)-Oriented Germanium by Electroplating, Text, Colorado School of Mines, **2016**.
- [136] T. Sadi, I. Radevici, P. Kivisaari, A. Casado, J. Oksanen, *Opt Quant Electron* **2019**, *51*, 207.
- [137] L. W. Molenkamp, H. F. J. van't Blik, *Journal of Applied Physics* **1988**, *64*, 4253.
- [138] Y. Zhao, M. Boccard, S. Liu, J. Becker, X.-H. Zhao, C. M. Campbell, E. Suarez, M. B. Lassise, Z. Holman, Y.-H. Zhang, *Nature Energy* **2016**, *1*, 16067.
- [139] R. E. Longshore, in *Handbook of Infra-Red Detection Technologies* (Eds.: M. Henini, M. Razeghi), Elsevier Science, Amsterdam, **2002**, pp. 233–267.
- [140] A. Waag, H. Heinke, S. Scholl, C. R. Becker, G. Landwehr, *Journal of Crystal Growth* **1993**, *131*, 607.
- [141] S. Nakashima, T. Fukumoto, A. Mitsuishi, K. Itoh, *J. Phys. Soc. Jpn.* **1973**, *35*, 1437.
- [142] J. M. Olson, R. K. Ahrenkiel, D. J. Dunlavy, B. Keyes, A. E. Kibbler, *Appl. Phys. Lett.* **1989**, *55*, 1208.
- [143] *CdTe and Related Compounds; Physics, Defects, Hetero- and Nano-Structures, Crystal Growth, Surfaces and Applications*, Elsevier, **2010**.
- [144] T. A. Gessert, S.-H. Wei, J. Ma, D. S. Albin, R. G. Dhere, J. N. Duenow, D. Kuciauskas, A. Kanevce, T. M. Barnes, J. M. Burst, W. L. Rance, M. O. Reese, H. R. Moutinho, *Solar Energy Materials and Solar Cells* **2013**, *119*, 149.
- [145] E. Yablonovitch, T. Gmitter, R. M. Swanson, Y. H. Kwark, *Appl. Phys. Lett.* **1985**, *47*, 1211.
- [146] Y. Liu, Y. Sun, A. Rockett, *Solar Energy Materials and Solar Cells* **2012**, *98*, 124.
- [147] S. Uličná, P. J. M. Isherwood, P. M. Kaminski, J. M. Walls, J. Li, C. A. Wolden, *Vacuum* **2017**, *139*, 159.
- [148] T. A. Gessert, P. Sheldon, X. Li, D. Dunlavy, D. Nilas, R. Sasala, S. Albright, B. Zadler, in *Conference Record of the Twenty Sixth IEEE Photovoltaic Specialists Conference - 1997*, IEEE, Anaheim, CA, USA, **1997**, pp. 419–422.
- [149] T. C. Anthony, A. L. Fahrenbruch, R. H. Bube, *JEM* **1982**, *11*, 89.
- [150] C. M. Rouleau, D. H. Lowndes, J. W. McCamy, J. D. Budai, D. B. Poker, D. B. Geohegan, A. A. Puretzky, S. Zhu, *Appl. Phys. Lett.* **1995**, *67*, 2545.

- [151] K. S. Lee, G. Oh, E. K. Kim, *Journal of the Korean Physical Society* **2015**, *67*, 672.
- [152] C. Miki, Growth and Characterization of CdTe/ZnTe Thin Films and Heterostructures, Thesis, **2014**.
- [153] K. Neyvasagam, N. Soundararajan, Ajaysoni, G. S. Okram, V. Ganesan, *physica status solidi (b)* **2008**, *245*, 77.
- [154] Y. He, T. Zhang, X. Shi, S.-H. Wei, L. Chen, *NPG Asia Materials* **2015**, *7*, e210.
- [155] Y. Zhao, X. Zhao, Y. Zhang, *IEEE Journal of Photovoltaics* **2017**, *7*, 690.
- [156] A. S. Chaves, H. Chacham, *Appl. Phys. Lett.* **1995**, *66*, 727.
- [157] A. S. Chaves, A. F. S. Penna, J. M. Worlock, G. Weimann, W. Schlapp, *Surface Science* **1986**, *170*, 618.
- [158] J. A. Greer, M. D. Tabat, *Journal of Vacuum Science & Technology A* **1995**, *13*, 1175.
- [159] J. Nelson, *The Physics of Solar Cells*, Imperial College Press, **2003**.
- [160] A. Nussbaum, in *Semiconductors and Semimetals* (Eds.: R.K. Willardson, A.C. Beer), Elsevier, **1981**, pp. 39–194.
- [161] P. A. Murawala, O. Tsuji, S. Fujita, S. Fujita, *Jpn. J. Appl. Phys.* **1991**, *30*, 3777.

8 Appendix

8.1 Optical and Electrical Characterisation of ZnO Films

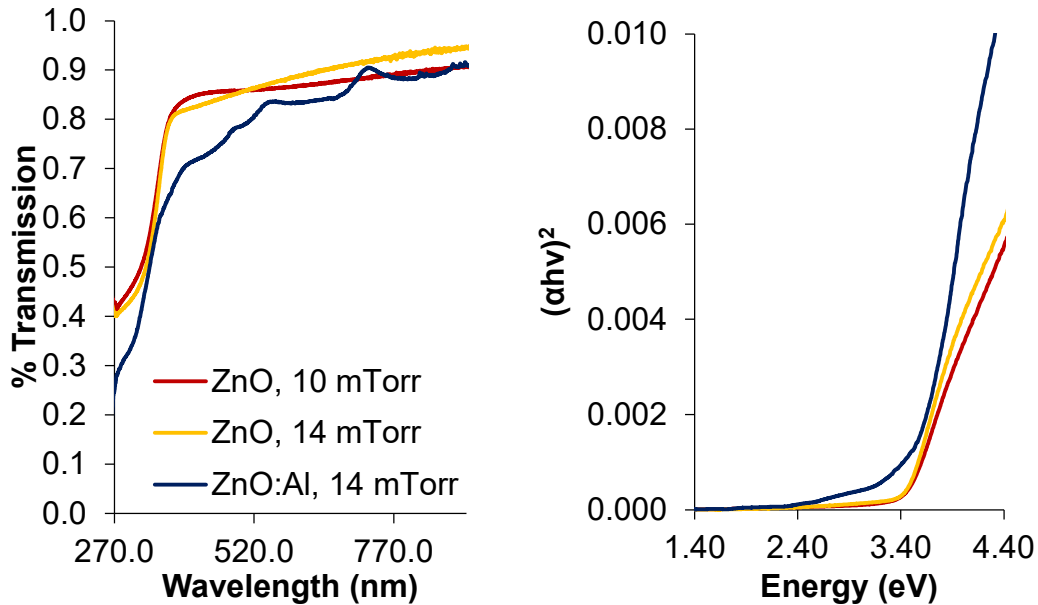


Figure 58: Optical characterization of ZnO and ZnO:Al films. Samples were deposited on glass substrates at room temperature in a partial pressure of O_2 by reactive PLD. (left) UV-visible spectroscopy spectra for transmission through transparent conductive oxide film on glass, with background glass absorption substrate. (right) Tauc plot used to determine the optical bandgap for direct transition in films.

O_2 Partial Pressure (mTorr)	Thickness (nm)	Resistivity ($m\Omega \cdot cm$)	Carrier Concentration (cm^{-3})	Mobility ($cm^2/V \cdot s$)
ZnO				
10	105	86.3	3.07×10^{19}	2.37
14	60	60.7	2.99×10^{19}	1.98
ZnO:Al				
14	45	5.18	2.60×10^{20}	4.63

Figure 59: Summary table of ZnO and ZnO:Al electrical characterization.

8.2 Optical and Electrical Characterisation of ZnTe:N Films

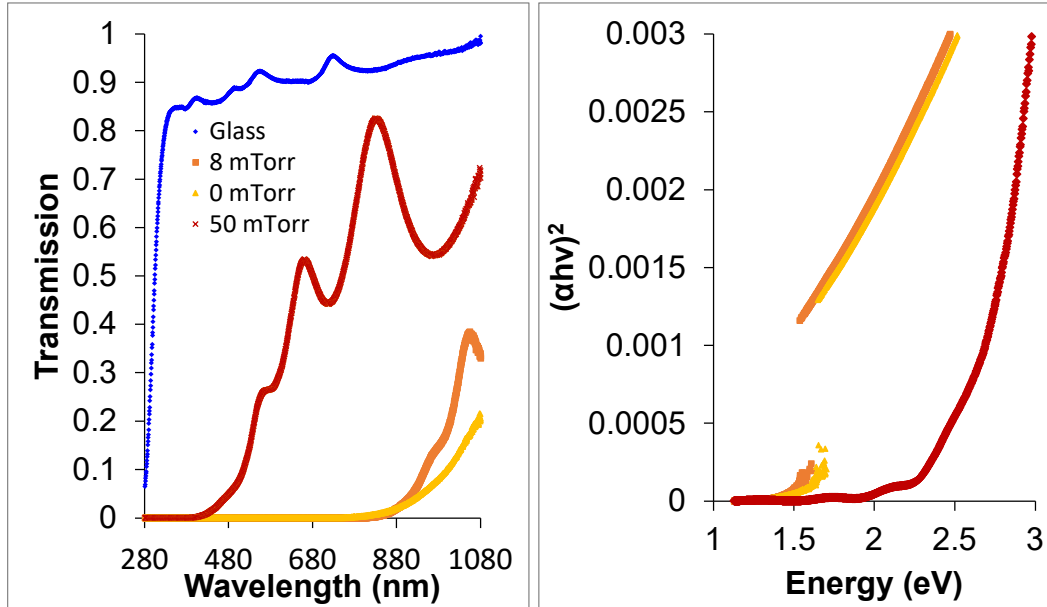


Figure 60: Optical characterization of ZnTe films. Samples were deposited on glass substrates at 100°C in a partial pressure of N₂ by reactive PLD. (left) UV-visible spectroscopy spectra for transmission through ZnTe films deposited on glass at different partial background pressures of N₂. Background transmission spectrum for glass substrate shown, was subtracted from the deposited samples to achieve the film spectra. (right) Tauc plot used to determine the optical bandgap for direct transition in films.

N ₂ Partial Pressure (mTorr)	Thickness (nm)	Resistivity (mΩ·cm)	Carrier Concentration (cm ⁻³)	Mobility (cm ² /V·s)
ZnTe:N				
0	1055	-	-	-
8	1033	-	-	-
50	290	4.93	2.22x10 ¹⁹	0.134

Figure 61: Summary table of ZnTe:N electrical characterization. Null values indicate value was unmeasurable in the van der Pauw hall effect/resistivity measurement apparatus. Measure of conductivity and carrier concentration in ZnTe:N films was much more unstable and variable comparable to the consistent values measured for ZnO and ZnO:Al films.